
Initial Data for Neutron Star Binaries with Arbitrary Eccentricity

Dissertation

zur Erlangung des akademischen Grades
doctor rerum naturalium (Dr. rer. nat.)

vorgelegt dem Rat der physikalisch-astronomischen Fakultät der
FRIEDRICH-SCHILLER-UNIVERSITÄT JENA

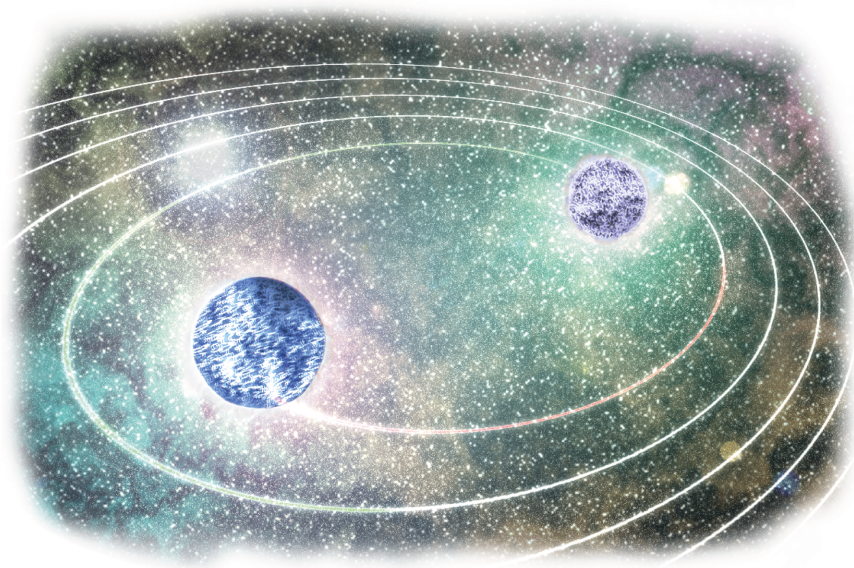
von

Niclas Moldenhauer

geboren am 04.05.1988 in Braunschweig



seit 1558



An artistic impression of two neutron stars orbiting each other

Gutachter:

1. Prof. Dr. Bernd Brügmann
Friedrich-Schiller-Universität Jena
2. PD Dr. Ewald Müller
MPI für Astrophysik Garching
3. Prof. Dr. Nikolaos Stergioulas
Aristotle University of Thessaloniki

Tag der Disputation: 19.04.2016

Contents

1	Introduction	3
2	Theoretical background in numerical relativity	9
2.1	3+1 decomposition	9
2.2	Initial data construction.....	16
2.2.1	Conformal transformation.....	16
2.2.2	Conformal thin-sandwich decomposition	18
2.3	Perfect fluid model	20
2.3.1	Thermodynamic quantities	21
2.3.2	Equations of state.....	22
2.4	Relativistic hydrodynamics.....	24
2.4.1	Matter evolution.....	24
2.4.2	Euler equation.....	27
3	Model and assumptions	29
3.1	Gravitational field equations.....	29
3.2	Stationary fluid approximation	31
3.2.1	Helical symmetry.....	31
3.2.2	Constant three-velocity approximation.....	33
3.2.3	Full velocity potential and spin	36
3.2.4	Eccentric orbits	38
3.2.5	Generalized orbits with radial velocity	45
4	Numerical method	47
4.1	Iteration recipe.....	47
4.2	Elliptic solver	49
4.2.1	Multigrid methods	50
4.3	BAM implementation	52

4.4	SGRID implementation	54
4.4.1	Grid configuration	55
4.4.2	Iteration	58
5	Neutron star initial data	61
5.1	Quasicircular orbits	61
5.2	Eccentric orbits	66
5.2.1	Convergence	68
5.2.2	Eccentric sequences and post-Newtonian comparisons	71
5.2.3	Trajectories and waveforms.....	75
5.3	Eccentricity reduced orbits	82
5.3.1	Eccentricity reduction scheme.....	83
5.3.2	Trajectories and waveforms.....	87
6	Irrotational binary inspiral	93
6.1	Irrotational Hamilton-Jacobi hydrodynamics.....	93
6.2	Preliminary numerical results	95
7	Conclusion.....	97
7.1	Summary.....	97
7.2	Future prospects.....	99
	Appendix	101
A	Stationarity in a linearly comoving frame.....	101
B	Nonrelativistic incompressible binaries.....	102
C	Publications.....	106
D	List of presentations	107
	Bibliography	117
	Abbreviations.....	119
	Acknowledgement.....	121
	Zusammenfassung	125

CHAPTER 1

Introduction

Exactly one hundred years ago Albert Einstein presented his theory of general relativity. Since then a lot of progress has been made and the theory has been confirmed several times, but its foundations have not changed. His famous equations connect the distribution of energy and matter with the curvature of spacetime

$$G_{ab} = R_{ab} - \frac{1}{2}g_{ab}R = \kappa T_{ab}. \quad (1.1)$$

Here, the energy and matter distribution is described via the stress energy tensor T_{ab} , while the curvature is given in terms of the Ricci tensor R_{ab} and scalar R , which in turn can be expressed in terms of the spacetime metric g_{ab} and its derivatives.

One of the predictions of general relativity which remains to be directly proved is the existence of gravitational waves. Today we know that the coalescences of compact binary objects, such as neutrons stars or black holes, are prominent sources for ground based gravitational wave (GW) detectors.

With the rise of computer technology came the desire and the possibility to run general relativistic simulations. In the early phase of numerical relativity, many groups focused on binary black hole systems, but especially within the last years, binary neutron star systems have got a lot of attention as well. In contrast to black hole binaries, binary neutron stars (BNS) have been observed via electromagnetic observations of binary pulsars and within this work, we will focus on such systems. The astronomy and relativity community are confidently looking forward to see the first detections of gravitational waves from neutron star or mixed black hole neutron star binaries within the next few years. Faber and Rasio [2012] (in particular Table 1 within their work) and more recently Dominik et al. [2015], give a review of estimated merger rates from population synthesis calculations. Besides the context of gravitational wave astronomy, neutron star binaries are also interesting from another points of view. For example, as suggested by Eichler et al. [1989], short gamma ray bursts could likely originate from neutron star coalescences. They could also play

an important role in the r -process, where heavy elements are produced which can be found in the interstellar medium.

Based on the observed BNS systems where at least one star is seen as a radio pulsar, one obtains some expectations on the stellar properties that have to be fulfilled in most cases (see the work of Lattimer [2012] and the corresponding link in the bibliography). Additionally, we can narrow down our range of expectations by looking at studies from Peters [1964] or Kowalska et al. [2011], where it is explained that the GW emission during long inspirals efficiently reduces the eccentricities of compact binaries. Summarizing these results, we would expect to observe coalescing binary neutron stars with low spins, negligible eccentricity and almost equal masses around $1.35M_{\odot}$. On the other hand, from a statistical point of view, the ~ 12 systems which have been observed so far and serve as a basis of the above considerations, are not sufficient to give definite results. It is thus possible that current observations are influenced by random selection effects. In fact, recent population synthesis models by Dominik et al. [2012] predict that the range of mass ratios and masses is wider than what has been found so far. Furthermore, the observable neutron star spins at merger could be larger than the current observations suggest. We pick up those discussions and astrophysical predictions in the appendix of [Mol3].

These points already show that it might not be sufficient to focus on neutron star simulations with restrictive choices of spins and mass ratios (most common choices are irrotational equal mass stars), but they also show that the negligible eccentricity is no safe assumption. In fact, all known BNS systems are eccentric to a certain degree. Postnov and Yungelson [2014] show in tables 2 and 3 of their work that those systems have eccentricities between $e = 0.085$ and $e = 0.681$ (we will define eccentricities e and various measurements later in this thesis). However, these mergers will occur within the next few hundred million years, and, due to GW radiation, the eccentricities before merger will admittedly be negligible. Nevertheless, there are other mechanisms which could produce highly eccentric binaries close to merger. As described in Lee et al. [2010], one of those scenarios are dynamical captures, i.e. the binary is formed in a dense stellar region such as globular clusters [Lee et al., 2010; O’Leary et al., 2009; Samsing et al., 2014; Tsang, 2013], where stars can be captured at small periapsis distance with high eccentricities. Alternatively, the Kozai mechanism in a hierarchical triple (see Antognini et al. [2014]; Antonini and Perets [2012]; Naoz et al. [2013]; Seto [2013]) can excite eccentricities in neutron star systems. According to Verbunt and Freire [2014], the production of eccentric systems in globular clusters is possible. But in general, compared to circular binaries, the eccentric counterparts are probably quite rare events.

On the other hand, the underlying physics allows interesting observations from those systems. Highly eccentric systems produce gravitational wave signals with repeated bursts. Although these signals are challenging for gravitational wave astronomy, they provide rewarding insights as it has been investigated by several other groups. Kyutoku and Seto [2014] find improvements in the accuracy of premerger sky localization and timing in comparison to the quasicircular case. In Loutrel et al. [2014], burst signals from highly eccentric binaries are considered as test regimes for general relativity, while East et al. [2013] and Tai et al. [2014] discuss strategies for detection of such systems. Furthermore, physical phenomena like electromagnetic flares from crust cracking during close encounters of eccentric binaries have been considered by Tsang [2013]. In summary, neutron star binaries cover a large parameter space of which several parts provide interesting physics, although these interesting parts might not be the first to be detected. In order to successfully detect gravitational waves, the models have to be carefully tuned.

This thesis puts its focus on binaries with arbitrary eccentricities. The only way to make accurate theoretical predictions of the properties of binary neutron star systems are full general relativistic hydrodynamical simulations. The neutron star binary parameter space has been explored in the context of varying eccentricities by other authors before. The first full numerical relativistic evolutions of neutron stars with large eccentricities have been performed by Gold et al. [2012], with some further investigations by East and Pretorius [2012]. Additionally, Lee et al. [2010] and Rosswog et al. [2013] have carried out simulations with Newtonian methods. The very similar topic of highly eccentric black hole-neutron star binaries has also been considered in papers by Stephens et al. [2011] and East et al. [2012a] (furthermore, it has to be mentioned that eccentric black hole binaries have been investigated for instance by Gold and Brügmann [2010, 2013], but due to the absence of matter, the treatment is different here). In general, all simulations need accurate initial data that fulfill Einstein's equations along with the Euler equation on a certain hypersurface. These data have to describe a system with the desired physical properties, and ideally should not be too far in time from merger, avoiding computationally expensive evolutions. Unfortunately, the works cited above, dealing with eccentric neutron stars, were lacking adequate initial data. Instead, they used inconsistent initial data, since it is not possible to apply the standard techniques of initial data construction, which have been used before. These techniques employ the binary's approximate helical Killing vector to solve the Euler equations via a first integral, but for eccentric binaries this vector is not valid. The workarounds used by the other

groups are fairly straightforward: Gold et al. [2012] boosted two superimposed spherical stars, which resulted in large violations of the Einstein constraint equations and additionally yielded unphysical matter configurations. The Princeton group [East and Pretorius, 2012; East et al., 2012a; Stephens et al., 2011] do solve the constraint equations, but their solutions did not satisfy Euler’s equation. Thus, it is not clear how accurate the simulations are and to what extent the tidally induced oscillations of the neutron stars found in these simulations are affected by the initial spurious oscillations of the stars due to polluted initial data.

There is a clear need of consistent initial data for these eccentric scenarios. Moreover, on the opposite end of the parameter space, i.e. for circular orbits, one encounters some problems as well. Numerous well-developed, sophisticated codes are in existence, which are capable of computing binary neutron star initial data. One of the most well known examples is the LORENE code from the Meudon group [Gourgoulhon et al.]. Other important codes are the Princeton solver East et al. [2012b] mentioned before, or COCAL as described in Tsokaros et al. [2015]. Recently, Tichy [2009a, 2011, 2012] made significant progress on the topic of spinning neutron star binary initial data. His code SGRID plays a major role in the advancement of these investigations (see e.g. Bernuzzi et al. [2014]). The problem at the lower end of the eccentricity range is that these codes produce data which result in evolutions with eccentricities $e \sim 10^{-2}$. Contrary to the expected, almost vanishing values of e in long lasting inspirals, these values are orders of magnitude too large. In case of binary black holes, there are techniques to reduce the residual eccentricities via iteration (see [Buonanno et al., 2011; Pürrer et al., 2012; Tichy and Marronetti, 2011]). But again, these methods are not applicable for standard binary neutron initial data construction schemes and need a generalization of the helical Killing vector. Note that during the development of this thesis Kyutoku et al. [2014] presented a method similar to the one we employ and that is used by the black hole community, but we come to this later in more detail.

In this thesis, we present a method which we published in [Mol1] and which allows to construct initial data with arbitrary eccentricity by generalizing the helical Killing vector to a pair of inscribed helical symmetry vectors. This takes into account a more general situation of an eccentric orbit at apoapsis. Also, we further extend the obtained symmetry vector by adding radial components, which are appropriate for gravitational wave radiation, and thus provide the opportunity to construct low-eccentric initial data. Our method yields constraint solved initial data under the assumption of conformal flatness (also known as Isenberg-Wilson-Mathews approxi-

mation [Isenberg, 2008; Wilson and Mathews, 1989]) with a self-consistent iteration scheme, keeping the geometry and matter in a momentarily stationary frame. Since we perform all evolutions with the fully general relativistic BAM code of the Jena group, we used the same code for a first proof-of-principle implementation of our scheme. These tests have been presented in [Mol1] and were restricted to equal-mass binaries with an irrotational flow. This flow was approximated by a homogeneous velocity field in order to make a simple implementation in Cartesian coordinates possible avoiding surface-fitted coordinates. The assumption of irrotational flow is standard and not too restrictive, since the known spins in binaries are at most 44 Hz for the more massive star in the double pulsar (see Table 2 of Postnov and Yungelson [2014]) and these spins will further decrease until merger. A couple of dozen orbits before merger, the system's orbital frequency is expected to be $\gtrsim 100$ Hz for quasicircular binaries, hence the assumption is justified.

After successfully computing the first eccentric orbits, we tried to obtain more accuracy and implemented the method in Tichy's pseudo-spectral SGRID code in order to achieve higher accuracy. This also allows the computation of low-eccentricity initial data and yields the opportunity to compute eccentric binaries with spin. Such binaries are interesting, since Bernuzzi et al. [2014] have found that spins of realistic magnitude can have a sizable effect on the system's dynamics. Especially in the eccentric scenarios originating from dynamic captures in globular clusters, larger spins of the individual stars are expected. The results of our SGRID implementation are published in [Mol3] and include a wide range of parameters. The generalized symmetry vector in addition to the existing, and recently implemented, features of SGRID allows us to compute more realistic equations of state (EoS), add individual spins to each star, vary the eccentricity of the orbits and consider larger mass ratios up to $q \sim 2$. Here, we focus on different eccentricities, while we make use of piecewise polytropic EoS and, furthermore, we provide some first experiments with eccentric spinning stars. We provide the framework to compute consistent initial data for neutron stars exploring regions of the parameter space not reached before. Though we provide several simulations to test our scheme, we do not concentrate on evolutions. Due to the vast number of combinations in parameter space, there are several interesting configurations that cannot be covered in this thesis. Current investigations about highly eccentric evolutions are to be published in [Mol4], but are only partially included here.

The structure of this thesis is as follows: After this initial introduction, we cover the fundamental work done on initial data. The standard approach to construct ini-

tial data in general relativity starts with the discussion of the 3+1 decomposition of spacetime. That chapter also provides the choice of our fluid model and a brief summary of relativistic hydrodynamics as needed for simulations including matter. Afterwards, in the third chapter we introduce our fluid model along with the assumptions we made and we discuss how this setup influences the equations from the first chapter. The fourth chapter gives details about the numerical methods. Here we show the recipe of our initial data construction scheme and the way we implemented it first in BAM and then in SGRID. Since large parts of the implementation rely on an elliptic multigrid solver, we briefly explain that concept as well. We finally show the results of our computations in chapter 5. These are divided into three subcategories: (i) The implementation has to be verified against existing codes, which has to be done in the limit of quasi circular data. (ii) The code can be tested for arbitrary, but large eccentricities, since these are fundamentally different from (iii) eccentricity reduced orbits. In part (i), we use data constructed with BAM and SGRID results as a reference. In (ii) we use both codes interchangeably, while the last part is studied with SGRID data.

The penultimate chapter is a short digression to an evolution scheme, particularly useful for irrotational binaries in our approximation made within BAM. We want to advertise the potential use of such a scheme that does not need an artificial atmosphere. We include this part due to the effort that has been invested, but wish to state upfront that this is work in progress and the results are promising, but preliminary. Finally, chapter 7 concludes this thesis and give some further prospects.

Throughout this work, we use the following notation adapted from Baumgarte and Shapiro [2010]: Latin letters from the beginning and the end of the alphabet a, b, \dots, h resp. o, p, \dots, z denote spacetime indices running from 0 to 3, while i, j, \dots, n denote spatial indices running from 1 to 3. We raise and lower all indices with the physical metric, i.e. the 3-metric for spatial indices and the 4-metric for spacetime indices. The summation convention is always employed and we shall also use index-free notation when convenient, denoting vectors using overset harpoons. We use geometric units with $G = c = M_{\odot} = 1$ almost exclusively, apart from the cases where we show the appearances of G explicitly for clarity when making some Newtonian calculations.

Theoretical background in numerical relativity

2.1 3+1 decomposition

To achieve our main goal, i.e. the construction of initial data, we have to specify the meaning of initial data in general relativity. Therefore it is inevitable to have a closer look at the numerical treatment of Einstein's equations. The struggle arises from the fact that Einstein's equations are written in an entirely covariant way, where time and space are treated equally. To recast this as an initial value problem, a split of time and spatial components is required. Although most of the approaches to these fundamental derivations are similar, they differ in details and styles. Many authors have covered this topic (e.g. [Alcubierre, 2008; Baumgarte and Shapiro, 2010; Gourgoulhon, 2006; Rezzolla and Zanotti, 2013]), and here we follow the route of Baumgarte and Shapiro [2010].

Projection operators and extrinsic curvature

We assume that the spacetime (\mathcal{M}, g_{ab}) can be foliated into spacelike hypersurfaces Σ , which do not intersect each other. These surfaces should be (at least locally) the level surfaces of a scalar function t . The idea is to decompose an arbitrary vector v^a (and of course in a similar way also arbitrary tensors) into its spatial part $\perp^a_b v^b$ and its timelike part $N^a v^b$. Therefore, we start with constructing the unit normal vector to the hypersurfaces Σ_t and thus consider the 1-form $\Omega_a = \nabla_a t$, respectively its normalized counterpart $\omega_a = \alpha \Omega_a$, with a normalization function α — also called *lapse*. The unit normal vector is now given by

$$n^\alpha = -g^{ab} \omega_b. \quad (2.1)$$

This now allows us to compute the induced spatial metric $\gamma_{ab} = g_{ab} + n_a n_b$, which serves as a projection operator if we raise one index

$$\perp^a{}_b = \gamma^a{}_b = g^a{}_b + n^a n_b. \quad (2.2)$$

While this operator projects 4-dimensional tensors into the spatial hypersurface, we need to define another projection operator $N^a{}_b$, which does an analogous projection into the normal direction,

$$N^a{}_b = -n^a n_b = \delta^a{}_b - \gamma^a{}_b. \quad (2.3)$$

Equipped with these tools, we are now able to project tensors into the spatial hypersurface or along the normal direction and we can also decompose tensors into their spatial and timelike parts. We first use the spatial projection operator to construct the *extrinsic curvature* K_{ab} .

The geometry of any spatial hypersurface Σ can be described by the intrinsic curvature, given by the three-dimensional Riemann tensor, i.e. the Riemann tensor constructed with the 3-metric γ_{ij} . To describe the embedding of the hypersurfaces into the four-dimensional manifold, we use the extrinsic curvature, which measures the change of a normal vector when it is parallel transported from one point to another one. As already indicated, we apply the projection tensor to construct K_{ab} , which makes the result purely spatial and symmetric and yields

$$K_{ab} = -\gamma_a{}^c \gamma_b{}^d \nabla_c n_d. \quad (2.4)$$

Note that it is equivalently possible to define the extrinsic curvature via the Lie derivative

$$K_{ab} = -\frac{1}{2} \mathcal{L}_n \gamma_{ab}, \quad (2.5)$$

if one expands (2.4) by inserting the definition of the projection operator (2.2) and introduces the acceleration of the unit normal vector $a_a \equiv n^b \nabla_b n_a$. Both versions will be used interchangeably, depending on the situation. Additionally, we introduce the trace of the curvature

$$K = g^{ab} K_{ab}, \quad (2.6)$$

which is also called the *mean curvature* (and could be written with the induced metric as well, due to the purely spatial nature of K_{ab}).

Projections of the Riemann tensor

In order to split Einstein's equations into spatial and timelike parts, we have to find a relation of the three-dimensional Riemann tensor $R^a{}_{bcd}$ of the hypersurfaces Σ and the four-dimensional counterpart ${}^{(4)}R^a{}_{bcd}$ of the manifold \mathcal{M} . Therefore, we want to look at different projections of the 4D Riemann tensor and due to the symmetries one can find that only three different non-vanishing projections exist. However, before we can relate these quantities, we have to express the covariant derivative ∇ in terms of covariant spatial derivatives, denoted by D .

For a spatial vector V^b , we want to look at the spatial gradient and we use the fact that $n_q \nabla_p V^q = -V^q \nabla_p n_q$, which follows directly from the spatial nature of V^q and the product rule. Now, we can follow

$$\begin{aligned} D_a V^b &= \gamma_a{}^p \gamma_q{}^b \nabla_p V^q \\ &= \gamma_a{}^p (g_q{}^b + n_q n^b) \nabla_p V^q \\ &= \gamma_a{}^p \nabla_p V^b - \gamma_a{}^p n^b V^q \nabla_p n_q \\ &= \gamma_a{}^p \nabla_p V^b - n^b V^e \gamma_a{}^p \gamma_e{}^q \nabla_p n_q \\ &= \gamma_a{}^p \nabla_p V^b + n^b V^e K_{ae} \quad . \end{aligned}$$

Analogously, one can write second derivative terms as

$$D_a D_b V^c = \gamma_a{}^p \gamma_b{}^q \gamma_r{}^c \nabla_p \nabla_q V^r - K_{ab} \gamma_r{}^c n^p \nabla_p V^r - K_a{}^c K_{bp} V^p. \quad (2.7)$$

We define the three dimensional Riemann tensor according to its higher dimensional counterpart

$$R^d{}_{ba} V_d = 2D_{[a} D_{b]} V^c. \quad (2.8)$$

Together with equation (2.7), this yields

$$R_{dcba} V^d = \gamma^p{}_a \gamma^q{}_b \gamma^r{}_c {}^{(4)}R_{drqs} V^d - 2K_{c[a} K_{b]d} V^d,$$

and with a re-summation allows us to write

$$R_{abcd} + K_{ac} K_{bd} - K_{ad} K_{cb} = \gamma^p{}_a \gamma^q{}_b \gamma^r{}_c \gamma^s{}_d {}^{(4)}R_{pqrs}, \quad (2.9)$$

which is known as *Gauss' equation*. In the subsequent calculations, we will make use of a slightly modified version of this equation, namely the *contracted Gauss equation*,

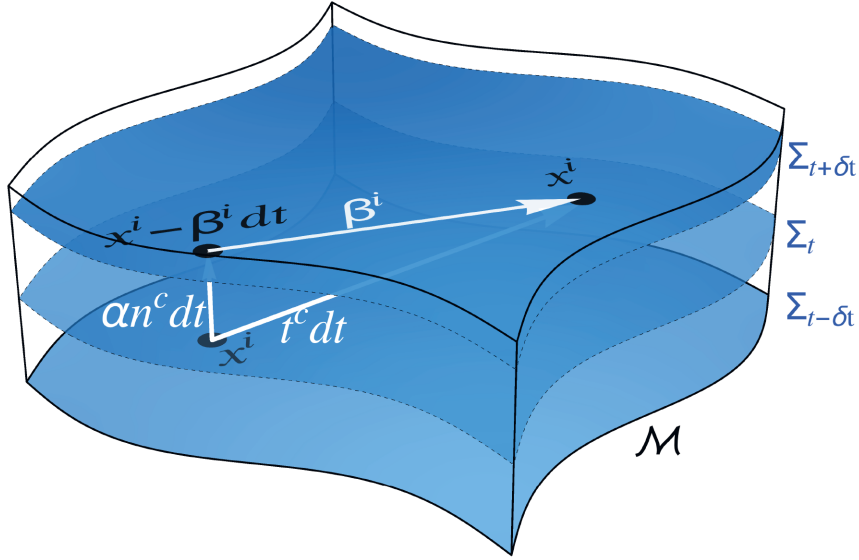


Figure 2.1: Depicted is the 3+1 Decomposition of the spacetime. A 4D Manifold \mathcal{M} is sliced into three-dimensional non-intersecting hypersurfaces Σ_t , where each of them is parametrized by a constant coordinate value t . Two neighboring slices are connected via the normal vector scaled with the lapse αn^c . The shift β^i lies inside a slice and measures the difference between this vector and the time vector t^c , which connects the points $x_i(t)$ and $x_i(t + \delta t)$ at two different times.

which can be written as

$$R_{bd} + K K_{bd} - K^c{}_d K_{cb} = \gamma^{pr} \gamma^q{}_b \gamma^s{}_d {}^{(4)}R_{pqrs}. \quad (2.10)$$

The second projection of the Riemann tensor that is needed, can be obtained by looking at

$$\begin{aligned} D_a K_{bc} &= \gamma^p{}_a \gamma^q{}_b \gamma^r{}_c \nabla_p K_{qr} \\ &= -\gamma^p{}_a \gamma^q{}_b \gamma^r{}_c (\nabla_p \nabla_q n_r + \nabla_p (n_q a_r)) \\ &= -\gamma^p{}_a \gamma^q{}_b \gamma^r{}_c \nabla_p \nabla_q n_r + a_c K_{ab}, \end{aligned}$$

where we inserted the definition of the extrinsic curvature (2.4) in the last equality. The last summand on the right-hand side can be dropped by anti-symmetrizing and we can plug in the definition of the four dimensional Riemann again:

$$D_b K_{ac} - D_a K_{bc} = \gamma^p{}_a \gamma^q{}_b \gamma^r{}_c n^s {}^{(4)}R_{pqrs}. \quad (2.11)$$

Equation (2.11) is known as *Codazzi equation* and once again, we use its contracted

counterpart

$$D_b K_a^b - D_a K = \gamma^p{}_a \gamma^{qr} n^s {}^{(4)}R_{pqrs}. \quad (2.12)$$

Finally, we look at the last non-trivial projection of the Riemann tensor, i.e. projected twice against the timelike direction. In particular we take the definition of the Lie derivative $\mathcal{L}_n K_{ab} = n^c \nabla_c K_{ab} + 2K_{c(a} \nabla_{b)} n^c$ and insert (2.4), which yields:

$$\mathcal{L}_n K_{ab} = -n^c \nabla_c \nabla_a n_b - n^c \nabla_c (n_a a_b) - 2K_{c(a} K_b)^c - 2K_{c(a} n_b) a^c. \quad (2.13)$$

Once again, we can employ the definition of the Riemann tensor and insert $\nabla_c \nabla_a n_b = {}^{(4)}R_{dbac} n^d + \nabla_a \nabla_c n_b$ and we get

$$\mathcal{L}_n K_{ab} = -n^c n^d {}^{(4)}R_{dbac} - n^c \nabla_a \nabla_c n_b - n^c \nabla_c (n_a a_b) - 2K_{c(a} K_b)^c - 2K_{c(a} n_b) a^c. \quad (2.14)$$

Another substitution can be made by using $n^c \nabla_a \nabla_c n_b = \nabla_a a_b - (\nabla_a n^c)(\nabla_c n_b) = \nabla_a a_b - K_a^c K_{cb} - n_a a^c K_{cb}$, where the product rule and the definition of the extrinsic curvature are employed, and in (2.14) several terms are canceled out:

$$\mathcal{L}_n K_{ab} = -n^c n^d {}^{(4)}R_{dbac} - \nabla_a a_b - n^c n_a \nabla_c a_b - a_c a_b - K_b^c K_{ac} - K_{ca} n_b a^c. \quad (2.15)$$

Finally, by rewriting the spatial derivative of the acceleration as $D_a a_b = -a_a a_b + 1/\alpha D_a D_b \alpha$ and by exploiting the spatial nature of $\mathcal{L}_n K_{ab}$, i.e. spatial projections do not effect it, we obtain *Ricci's equation*

$$\mathcal{L}_n K_{ab} = n^d n^c \gamma^q{}_a \gamma^r{}_b {}^{(4)}R_{drcq} - \frac{1}{\alpha} D_a D_b \alpha - K_b^c K_{ac}. \quad (2.16)$$

Constraint and evolution equations

Using the equations derived in the previous subsection, it is straightforward to derive the 3+1 decomposed Einstein equations. First, the contracted Gauss equation (2.10) is further contracted by multiplying it with γ^{bd} , which yields

$$\gamma^{pr} \gamma^{qs} {}^{(4)}R_{pqrs} = R + K^2 - K_{ab} K^{ab}. \quad (2.17)$$

Expanding the three dimensional metric by virtue of (2.2) and using the identity $-n^r n_r = n^p n^r (\gamma_{pr} - n_p n_r) = 1$, we can finally write (2.17) as

$$\begin{aligned} 2n^p n^r {}^{(4)}R_{pr} - n^p n^r g_{pr} {}^{(4)}R &= R + K^2 - K_{ab}K^{ab} \\ 2n^p n^r G_{pr} &= R + K^2 - K_{ab}K^{ab} = 16\pi\rho_H, \end{aligned} \quad (2.18)$$

where we used $\rho_H = n_a n_b T^{ab}$ to define the total energy density as measured by a normal observer n^a and Eq. (2.18) is known as *Hamiltonian constraint*. In a similar manner, we can derive another constraint equation by looking at the contracted Codazzi equation (2.12). Its right-hand side can be written as

$$\begin{aligned} -\gamma^p{}_a (g^{qr} + n^q n^r) n^s {}^{(4)}R_{qprs} &= -\gamma^p{}_a n^s {}^{(4)}R_{ps} \\ &= -\gamma^p{}_a n^s {}^{(4)}R_{ps} - \frac{1}{2} \gamma_{as} n^s {}^{(4)}R \\ &= -\gamma^p{}_a n^s {}^{(4)}R_{ps} - \frac{1}{2} \gamma^p{}_a n^s g_{ps} {}^{(4)}R = -\gamma^p{}_a n^s G_{ps} \quad , \end{aligned}$$

where we just added a zero in the second step. This enables us now to write the mixed projection of Einstein's equations as

$$D_b K_a{}^b - D_a K = 8\pi S_a \quad , \quad (2.19)$$

with the momentum density $S_a = -\gamma^b{}_a n^c T_{bc}$. This equation is known as the *momentum constraint*. The constraints (2.18) and (2.19) correspond to four equations that contain no time derivatives and have to be fulfilled at all times.

On the other hand, we want to derive the evolution equations from the remaining, fully spatial projection of Einstein's field equations. Inserting the contracted Gauss equation (2.10) into Ricci's equation (2.16), while expanding γ^{ab} according to its definition, leads to

$$\gamma^q{}_a \gamma^s{}_b {}^{(4)}R_{qs} = -\mathcal{L}_n K_{ab} - \frac{1}{\alpha} D_a D_b \alpha - 2K^c{}_b K_{ac} + R_{ab} + K K_{ab}. \quad (2.20)$$

Looking at the full spatial projection of Einstein's equations yields

$$\begin{aligned} \gamma^q{}_b \gamma^s{}_d {}^{(4)}R_{qs} &= 8\pi \left(\gamma^q{}_b \gamma^s{}_d T_{qs} - \frac{1}{2} \gamma^q{}_b \gamma^s{}_d T g_{qs} \right) \\ &= 8\pi \left(S_{bd} - \frac{1}{2} \gamma_{bd} (S - \rho) \right), \end{aligned} \quad (2.21)$$

where we recognize ρ_H and introduced the momentum current $S_{bd} = \gamma^q{}_b \gamma^s{}_d T_{qs}$ along

with its trace $S = S^a_a$. Combining (2.20) and (2.21) gives us an evolution equation for the extrinsic curvature, which is the last equation we were looking for

$$\mathcal{L}_t K_{ab} = -D_a D_b \alpha + \mathcal{L}_\beta K_{ab} + \alpha \left(-2K^c_b K_{ac} + R_{ab} + K K_{ab} - 8\pi \left(S_{bd} - \frac{1}{2} \gamma_{bd} (S - \rho) \right) \right). \quad (2.22)$$

To obtain this result, it is necessary to decompose $t^a = \alpha n^a + \beta^a$ with the lapse α and the spatial shift β^a , since n^a is not dual to the surface 1-form Ω_a and therefore, \mathcal{L}_n is no natural time derivative with respect to t . Together with the coordinate choice we will make, the Lie derivative then reduces to a partial derivative.

ADM equations

To obtain numerically useful equations, we still have to specify basis vectors. Arnowitt et al. [1962] suggested to chose spatial basis vectors $e^a_{(i)}$, which lie completely in the hypersurface and a time basis vector t^a , which has to fulfill $t^a = (1, 0, 0, 0)$. Making these choices has consequences for the derived 3+1 decomposed equations. From the spatial nature of the basis vectors, $0 = \Omega_a e^a_{(i)} = -1/\alpha n_a e^a_{(i)}$, it follows $n_i = 0$. Using this together with the decomposition of t^a into lapse and shift, we can write $n^a = 1/\alpha(1, \beta^i)$ and from $n^a n_a = -1$, it is obvious that $n_a = (-\alpha, 0, 0, 0)$. Altogether, this yields

$$g^{ab} = \gamma^{ab} - n^a n^b = \begin{pmatrix} -\alpha^{-2} & \alpha^{-2} \beta^i \\ \alpha^{-2} \beta^j & \gamma_{ij} - \alpha^{-2} \beta^i \beta^j \end{pmatrix}, \quad (2.23)$$

which can be written as a 3+1 line element

$$ds^2 = -\alpha^2 dt^2 + \gamma_{ij} (dx^i + \beta^i dt)(dx^j + \beta^j dt). \quad (2.24)$$

Due to the simplicity of the time vector, the Lie derivative simplifies to partial derivatives and the 3+1 equations can be written as

$$R + K^2 - K_{ij} K^{ij} = 16\pi \rho_H, \quad (2.25)$$

$$D_j K_i^b - D_i K = 8\pi S_i \quad (2.26)$$

$$\begin{aligned} \partial_t K_{ab} = & \alpha \left(-2K^k_i K_{jk} + R_{ij} + K K_{ij} - 8\pi \left(S_{ij} - \frac{1}{2} \gamma_{ij} (S - \rho_H) \right) \right) \\ & - D_i D_j \alpha + \beta^k D_k K_{ij} + K_{ik} D_j \beta^k + K_{kj} D_i \beta^k, \end{aligned} \quad (2.27)$$

$$\partial_t \gamma_{ij} = -2\alpha K_{ij} + D_i \beta_j + D_j \beta_i \quad (2.28)$$

where the evolution equation for the metric is directly coming from the definition of the curvature. We want to note that this is not the final form of the evolution equations for numerical purposes. Due to the limited extent of this thesis, we cannot go into details about other formulations, but we use the BSSN and Z4c reformulation within the thesis, since they are better suited for numerical approximation.

2.2 Initial data construction

In section 2.1, we saw that Einstein's equations can be decomposed into evolution equations (2.22) and constraint equations (2.18) and (2.19), when we want to bring them into a suitable form for numerical treatment. This also means that it is not trivial to start an evolution on an arbitrary slice by freely specifying (γ_{ij}, K_{ij}) . We have to keep in mind that every choice we make has to fulfill the constraint equations, while fitting the desired physical situation. Similar properties are well known from other topics in physics, like electrodynamics, where we also find a set of coupled differential equations. In analogy to the 3+1 equations, two of Maxwell's equations contain time derivatives and are used to determine the evolution of a system, while on the other hand two equations constrain the solution, including the initial slice. For instance, if the divergence of the magnetic field $\nabla \cdot \vec{B}$ does not vanish, we are not solving Maxwell's equations.

The idea behind initial data construction is to simplify the problem by decomposing the constraints. An example from the simpler electromagnetic equations would be a scaling of the electric field $E^i = \psi^4 \bar{E}^i$. Instead of choosing values for two components of E and then solving the constraint $D_i E^i = 4\pi\rho$ for the third, the scaling enables us to arbitrarily choose a background field \bar{E} and then solve the constraint for the scaling factor.

2.2.1 Conformal transformation

Similarly, we can make a conformal transformation of the metric and introduce a conformally related background metric

$$\gamma^{ij} = \psi^4 \bar{\gamma}^{ij}, \quad (2.29)$$

as it was done by Lichnerowicz [1944] and York [1971]. With $\det(\gamma_{ij}) := \gamma = \psi^{12}$, we can write the inverse relation as

$$\bar{\gamma}_{ij} = \gamma^{-1/3} \gamma_{ij} \quad (2.30)$$

with the benefit that the determinant of the conformal metric $\bar{\gamma}$ equals one. Further note that all quantities associated with the conformal metric are denoted with a bar. The following procedure is straightforward and consists of using (2.29) with the definition of the Christoffel symbols to compute their transformed counterparts and use these to calculate the modified Ricci scalar. Doing this yields

$$R = \psi^{-4} \bar{R} - 8\psi^{-5} \bar{D}^2 \psi, \quad (2.31)$$

which can directly be plugged into the Hamiltonian constraint (2.18) to obtain

$$8\bar{D}^2 \psi - \psi \bar{R} + \psi^5 K_{ij} K^{ij} = -16\pi \psi^5 \rho_H \quad . \quad (2.32)$$

In the same manner, we can modify the momentum constraint equations. Additionally to the conformal transformation, we insert another transformation, which is a decomposition of the extrinsic curvature K_{ij} into its traceless part A_{ij} and its trace K

$$K_{ij} = A_{ij} + \frac{1}{3} \gamma_{ij} K \quad . \quad (2.33)$$

Finally, we define conformally related quantities by multiplying with powers of the conformal factor, where the exponents are chosen such that a convenient form will be obtained later (again, for further details we refer to a full discussion as in Baumgarte and Shapiro [2010]).

$$A^{ij} = \psi^{-10} \bar{A}^{ij} \quad , \quad A_{ij} = \psi^{-2} \bar{A}_{ij} \quad , \quad K = \bar{K}. \quad (2.34)$$

Inserting (2.33) and (2.34) into the constraints results in the following set of equations

$$\text{Hamiltonian constraint: } 8\bar{D}^2 \psi - \psi \bar{R} + \psi^{-7} A_{ij} A^{ij} - \frac{2}{3} \psi^5 K^2 = -16\pi \psi^5 \rho_H \quad (2.35)$$

$$\text{Momentum constraint: } \bar{D}_j \bar{A}^{ij} - \frac{2}{3} \psi^6 \bar{\gamma}^{ij} \bar{D}_j K = 8\pi \psi^{10} S^i. \quad (2.36)$$

A closer look at the operators of (2.35) shows that we have a Laplacian on the left-hand side and we will further modify the momentum constraint (2.36) as well, in order to obtain elliptic equations that we have to solve.

2.2.2 Conformal thin-sandwich decomposition

Until now we were able to recast the problem of initial data construction and introduced a Laplace operator. However, the constraint equations are only specified on a single hypersurface. As a natural consequence of this, nothing can be said about the gauge quantities α and β^i . The problem that often arises in this case is the difficulty in choosing the freely specifiable data and the corresponding influence on the resulting physical solutions. An idea to circumvent this problem was proposed by York [1999] with the so-called *conformal-thin sandwich decomposition* or for short CTS. Instead of choosing the conformal metric $\bar{\gamma}_{ij}$ and e.g. the transverse traceless part of the extrinsic curvature \bar{A}_{TT}^{ij} (as it is done in the conformal transverse traceless [CTT] decomposition) on a single hypersurface, we want to specify the three-metric on two neighboring slices Σ_t and $\Sigma_{t+\delta t}$, which corresponds to the specification of a time derivative of the metric if we take the limit $dt \rightarrow 0$. In this spirit, we define

$$\bar{u}_{ij} := \partial_t \bar{\gamma}_{ij} \quad (2.37)$$

in addition to the definitions from Sec. 2.2.1 to denote the time derivative of the three-metric. We do not want the conformal volume element to vary in time, i.e.

$$\bar{\gamma}^{ij} \bar{u}_{ij} = 0 \quad . \quad (2.38)$$

In the next step, the trace-free part of \bar{u}_{ij} is defined as

$$u_{ij} := \partial_t \gamma_{ij} - \frac{1}{3} \gamma_{ij} (\gamma^{kl} \partial_t \gamma_{kl}) \quad (2.39)$$

We can make use of the evolution equation (2.28) and insert it into (2.39), which yields

$$u^{ij} = -2\alpha A^{ij} + (L\beta)^{ij}, \quad (2.40)$$

where we used the vector gradient L with $(L\beta)^{ij} = D^i \beta^j + \nabla^j \beta^i - \frac{2}{3} \gamma^{ij} \nabla_k \beta^k$. Equation (2.38) lets us derive $12\partial_t \psi = \partial_t \ln(\gamma)$, which in turn can be combined with (2.40) to rewrite the time derivative of the conformal three-metric as

$$\bar{u}_{ij} = \partial_t (\psi^{-4} \gamma_{ij}) = \psi^{-4} \left(\partial_t \gamma_{ij} - \frac{1}{3} \gamma_{ij} \partial_t \ln(\gamma) \right) = \psi^{-4} u_{ij}. \quad (2.41)$$

Plugging equation (2.41) in a rearranged version of (2.40), we finally find

$$\bar{A}^{ij} = -\frac{\psi^6}{2\alpha} (\bar{u}^{ij} - (\bar{L}\beta)^{ij}). \quad (2.42)$$

Equation (2.42) relates the conformal traceless part of the extrinsic curvature \bar{A}^{ij} to the shift β^i and we can make use of this relation by modifying the momentum constraint (2.36)

$$(\bar{\Delta}_L \beta)^i - (\bar{L}\beta)^{ij} \bar{D}_j \ln(\bar{\alpha}) = \bar{\alpha} \bar{D}_j (\bar{\alpha}^{-1} \bar{u}^{ij}) + \frac{4}{3} \bar{\alpha} \psi^6 \bar{D}^i K + 16\pi \bar{\alpha} \psi^{10} S^i \quad , \quad (2.43)$$

where we introduced the *densitized* lapse $\bar{\alpha} = \psi^{-6} \alpha$ to get a convenient form.

At this point all necessary material has been gathered to construct a solution of the initial value problem for given background data.

CTS and XCTS equations

Similar to other approaches, like the CTT decomposition mentioned before, the CTS decomposition allows us to freely specify the background metric $\bar{\gamma}_{ij}$, which fixes five degrees of freedom. Another five degrees can be fixed by choosing its time derivate \bar{u}^{ij} , which is a particular feature of the CTS approach. Furthermore, we have to take into account the free choice of the trace of the extrinsic curvature K and the rescaled lapse $\bar{\alpha}$, which each fix one additional degree of freedom. This makes 12 variables from a total of 16 independent variables that are provided by the CTS decomposition. The derived Hamiltonian constraint, see Eq. (2.35)

$$\bar{D}^2 \psi - \frac{1}{8} \psi \bar{R} + \frac{1}{8} \psi^{-7} A_{ij} A^{ij} - \frac{1}{12} \psi^5 K^2 = -2\pi \psi^5 \rho_H \quad (2.44)$$

and momentum constraint (2.43) can then be used to compute the remaining four variables ψ and β^i .

The full recipe to obtain initial data is to start with the momentum constraint (2.43) and solve it for the shift β^i , which enables us to compute

$$\bar{A}^{ij} = \frac{1}{2\bar{\alpha}} ((\bar{L}\beta)^{ij} - \bar{u}^{ij}) . \quad (2.45)$$

Having A^{ij} at hand, we can proceed by solving the Hamiltonian constraint (2.44) for ψ . After gathering the information about the variables in the CTS equations, we can construct the physical solution similar to the example of Maxwell's equations in the

beginning of this section. The quantities we are looking for are obtained through

$$\gamma_{ij} = \psi^4 \bar{\gamma}_{ij}, \quad (2.46)$$

$$K_{ij} = \psi^{-2} \bar{A}_{ij} + \frac{1}{3} \gamma_{ij} K, \quad (2.47)$$

$$\alpha = \psi^6 \bar{\alpha}. \quad (2.48)$$

This is one way to construct the constraint-solved physical data γ_{ij} and K_{ij} by solving an elliptical problem with four coupled equations. However, there exists a slight alteration to this decomposition, which was also described by York [1999], i.e. the *extended* conformal thin-sandwich formalism. Instead of freely specifying the densitized lapse $\bar{\alpha}$ we want the freedom to choose the time derivative of the trace of the extrinsic curvature $\partial_t K$. The result of this formalism is the free choice of the metric $\bar{\gamma}_{ij}$ and the mean curvature K as well as their time derivatives.

Therefore, the evolution equation of the extrinsic curvature (2.27) has to be contracted once and combined with the Hamiltonian constraint (2.35), which yields

$$\bar{D}^2(\alpha\psi) = \alpha\psi \left(\frac{7}{8} \psi^{-8} \bar{A}_{ij} \bar{A}^{ij} + \frac{5}{12} \psi^4 K^2 + \frac{1}{8} \bar{R} + 2\pi\psi^4 (\rho_H + 2S) \right) - \psi^5 \partial_t K + \psi^5 \beta^i \bar{D}_i K. \quad (2.49)$$

We refer to equation (2.49) as the *lapse equation*, since it is another elliptic equation we have to solve in order to obtain the lapse. We now ended up with a set of five coupled nonlinear elliptic equations. In fact, the extended conformal thin-sandwich formalism is the one we choose throughout this work as a foundation of our method. As we will see later, we choose this decomposition over the others since it allows us to easily specify the given data.

2.3 Perfect fluid model

When dealing with neutron star simulations, i.e. considering evolutions as well as initial data, we have to handle matter in order to describe the stars properly. Typically, this means that we have to choose a model which describes the matter and we have to fulfill the equations governing the matter and energy behavior. We start by choosing a fluid model and we briefly explain the consequences.

2.3.1 Thermodynamic quantities

Throughout all parts of this thesis we assume that the matter of the neutron star can be modeled as a perfect fluid, which neglects phenomena such as heat conduction or shear stresses. A good overview about different models and their justifications was given by Andersson and Comer [2007]. The mathematic description of such a fluid is given by an energy-momentum tensor

$$T_{ab} = \rho h u_a u_b + p g_{ab}, \quad (2.50)$$

where ρ is the rest mass density, h the specific enthalpy, p the fluid pressure and u_a is the four-velocity. As in the previous sections g_{ab} is the Lorentzian metric used to describe a spacetime (\mathcal{M}, g_{ab}) together with a four dimensional manifold \mathcal{M} . the specific enthalpy h can be expressed in terms of the pressure p , the rest-mass density ρ and the proper energy density ϵ , i.e.

$$h := \frac{\epsilon + p}{\rho}. \quad (2.51)$$

We further restrict our fluid to be *simple*, which means that the equation of state of the fluid can be described by some function

$$\epsilon = \epsilon(\sigma, n), \quad (2.52)$$

where σ is the entropy density and n the baryon number density. In other words this means that all thermodynamic quantities that describe the fluid can be seen as only depending on σ and n . From thermodynamics we know how to define the temperature T and the baryon chemical potential μ in terms of the quantities we introduced so far

$$T := \frac{\partial \epsilon}{\partial \sigma} \quad \text{and} \quad \mu := \frac{\partial \epsilon}{\partial n}. \quad (2.53)$$

Another very elemental feature that arises from thermodynamics is the conservation of energy, also known as the first law of thermodynamics. In our case it can be expressed as

$$d\epsilon = \mu dn + T d\sigma. \quad (2.54)$$

We can now make use of the fundamental thermodynamic relation, which expresses the internal energy U as

$$dU = T dS - p dV, \quad (2.55)$$

where S is the entropy, and exploit the assumption that ϵ depends only on σ and n (2.52) to express the pressure as

$$p = -\epsilon + T\sigma + \mu n. \quad (2.56)$$

Taking into account the definitions of the rest-mass density from the atomic mass unit $m_b = 1.66 \times 10^{-27} \text{kg}$

$$\rho := m_b n \quad (2.57)$$

and of the specific entropy

$$s := \sigma / \rho, \quad (2.58)$$

we can rewrite the specific enthalpy (2.51) as

$$h = \frac{\mu}{m_b} + Ts. \quad (2.59)$$

Finally, we can use Eqs. (2.54)–(2.59), to derive the thermodynamic relations as in Gourgoulhon [2006]

$$d\epsilon = h d\rho + \rho T ds, \quad dp = \rho (dh - T ds). \quad (2.60)$$

2.3.2 Equations of state

In order to close the system of equations, we have to specify an equation of state, which describes the matter inside the neutron star. The correct description of neutron star matter is unknown. However, a one parameter EoS for cold matter above nuclear density can be used to model the matter rather accurately, due to the low temperature of the star compared to its particle's Fermi energy. Moreover, it is fairly easy to implement a more realistic model as it was done by Read et al. [2009b], who used a piecewise polytropic approach to approximate the EoSs.

Polytropic EoS

In most parts of this work we only consider simple polytropic equations of state, since these are perfectly fine for a large series of tests as they have been showed in [Mol1]. These EoS assume a relation of the pressure p and the rest-mass density ρ

$$p = \kappa \rho^{1+1/n}, \quad (2.61)$$

where κ is the polytropic constant, $n = \frac{1}{\Gamma-1}$ is the polytropic index and Γ is known as the adiabatic index. We restrict our parameter space for simple polytropes to $\Gamma = 2$, which corresponds to $n = 1$. This is a common choice, since it is sufficient for testing and it is close to the effective polytropic index of realistic nuclear physics equations of state as shown in Lattimer and Prakash [2001]. The basic quantity in our code is the specific enthalpy h , so we want to express ρ , p , and ϵ in terms of h

$$\rho = \left[\frac{h-1}{\kappa(1+n)} \right]^n, \quad (2.62a)$$

$$p = \kappa \left[\frac{h-1}{\kappa(1+n)} \right]^{1+n}, \quad (2.62b)$$

$$\epsilon = \left[1 + \frac{n(h-1)}{1+n} \right] \left[\frac{h-1}{\kappa(1+n)} \right]^n. \quad (2.62c)$$

The advantage of taking h as a basic variable will become clear in the next section. In this approach, the matter variables inside the star are C^∞ except for the star's surface, which needs to be handled carefully. However, as a next step the above approach can be generalized by stitching several polytropes together in order to compute a more realistic model. In that case, h is more accurate and for a single TOV star it is differentiable inside the star, which makes it more suitable than ρ (or more precisely p/ρ , as it is chosen in many codes) for taking derivatives.

Piecewise polytropic EoS

Piecewise polytropes consist of different density intervals and thus provide more parameters to tweak the EoS. Read et al. [2009a,b] show that these more realistic descriptions of the neutron star's matter can potentially be used in gravitational wave astronomy to constrain free parameters and get more insight into the underlying physics. On the technical side, the drawback of the piecewise polytropic approach is given by the fact that the matter variables are losing their nice properties and are only C^0 continuous inside the star instead of arbitrarily differentiable. In [Mol3] we constructed piecewise polytropes by taking the possible range of densities and divided it into intervals $[0, \rho_0], [\rho_0, \rho_1], [\rho_1, \rho_2], \dots$, where the intervals are labeled by $i = 0, 1, 2, \dots$. The EoS in each interval is given by a polytropic relation of the same

kind as (2.62), but with varying parameters n and κ , so that we obtain

$$p = \kappa_i \rho^{1+1/n_i}, \quad (2.63a)$$

$$h = (n_i + 1) \kappa_i \rho^{1/n_i} + K_i, \quad (2.63b)$$

$$\epsilon = (n_i \kappa_i \rho^{1/n_i} + K_i) \rho. \quad (2.63c)$$

When we compare (2.62) and (2.63) we see immediately that K_0 must be one, since the enthalpy has to be unity at the outer region. While $\kappa_{i \neq 0}$ and $K_{i \neq 0}$ are determined by demanding continuity, the other parameters n_i and κ_0 can be chosen freely so that a desired EoS is modeled. The relations arising from continuity are given by

$$\kappa_i = \kappa_{i-1} \rho_i^{1/n_{i-1} - 1/n_i}, \quad (2.64a)$$

$$K_0 = 1, \quad (2.64b)$$

$$K_i = K_{i-1} + n_{i-1} \kappa_{i-1} \rho_i^{1/n_{i-1}} - n_i \kappa_i \rho_i^{1/n_i}. \quad (2.64c)$$

Throughout this work we use values for the parameters as given by Read et al. [2009b] and we study some exemplary models such as H4, MS1b and SLy. All of these setups result in reasonable maximal masses of a neutron star with $M_{\max} \geq 1.99M_{\odot}$ and adiabatic sound speeds less than the speed of light.

2.4 Relativistic hydrodynamics

After presenting the fluid model to handle the matter model in our simulations, the next step is to discuss the treatment of matter in a physically reasonable way. We start with a short summary of the equations governing the matter evolutions. This is useful, since we perform several evolutions throughout the work using the below introduced concepts. Moreover, in chapter 6 we present the concept of a new matter evolution scheme. However, the focus of this thesis is the construction of initial data. Thus we keep that investigation brief and discuss the crucially needed Euler equation in the subsequent section in more detail.

2.4.1 Matter evolution

In order to provide the concepts and information needed within this thesis, we follow the route of Rezzolla and Zanotti [2013], to which we also refer for a complete, more detailed description.

The starting point for this discussion are the *general relativistic hydrodynamic equa-*

tions

$$\nabla_a J^a = 0, \quad (2.65)$$

$$\nabla_b T^{ab} = 0, \quad (2.66)$$

where J^a is the rest-mass density current, while T^{ab} is again the energy-momentum tensor, introduced in (1.1). Eq. (2.65) represents the conservation of the rest mass, while (2.66) represents conservation of energy and momentum. First, we have to make the derivation less general by choosing a certain fluid model, which in our case is the *perfect fluid model*, as it was explained in Section 2.3.1. Inserting the stress-energy tensor (2.50) into (2.66) yields

$$\nabla_a J^a = \nabla_a(\rho u^a) = u^a \nabla_a \rho + \rho \nabla_a u^a = 0, \quad (2.67)$$

$$\nabla_b T^{ab} = \nabla_b ((e + p)u^a u^b + pg^{ab}) = 0. \quad (2.68)$$

Martí et al. [1991] introduced a formulation of the relativistic hydrodynamic equations in conservative form, which is particularly useful for numerical purposes. Due to the strong geographical concentration of its creators, this formulation is also known as the “*Valencia*” *formulation*. The basic idea is to rewrite (2.65) and (2.66) in conservative form by introducing a new set of conservative variables.

We can easily transform the equation of rest-mass conservation by using the identity $\nabla_a X^a = \frac{1}{\sqrt{-g}} \partial_a (\sqrt{-g} X^a)$ and afterwards define the conserved variable

$$D := \rho \alpha u^t, \quad (2.69)$$

so that we can write (2.65) as

$$\partial_t(\sqrt{\gamma}D) + \partial_i(\sqrt{\gamma}D(\alpha v^i - \beta^i)) = 0, \quad (2.70)$$

which provides a conservative form. In order to bring the energy-momentum conservation equations to a conservative form, we use the definitions of the different projections of the energy-momentum tensor T from section 2.1 to rewrite it as

$$T^{ab} = (e + p)u^a u^b + pg^{ab} = \rho_H n^a n^b + S^a n^b + S^b n^a + S^{ab}. \quad (2.71)$$

On the other hand, inserting a decomposition of the fluid four-velocity as $u^a =$

$W(n^a + v^a)$ yields

$$T^{ab} = \rho h W^2 (n^a + v^a)(n^b + v^b) + p(\gamma^{ab} - n^a n^b). \quad (2.72)$$

A term by term comparison of (2.71) and (2.72) gives us the expressions

$$\rho_H = \rho h W^2 - p, \quad (2.73)$$

$$S^a = \rho h W^2 v^a, \quad (2.74)$$

$$S^{ab} = \rho h W^2 v^a v^b + p \gamma^{ab}. \quad (2.75)$$

We can express the conservative form of the momentum conservation equations with the same methods as above. We use an identity to rewrite the four-divergence of a symmetric rank-2 tensor as

$$\frac{1}{\sqrt{-g}} \partial_a (\sqrt{-g} T^a_b) = \frac{1}{2} T^{ac} \partial_b g_{ac}. \quad (2.76)$$

Substituting (2.71) into (2.76) while only considering spatial indices, yields the conservative form of the momentum equation

$$\partial_t (\sqrt{\gamma} S_j) + \partial_i (\sqrt{\gamma} (\alpha S^i_j - \beta^i S_j)) = \frac{1}{2} \sqrt{-g} T^{ab} \partial_j g_{ab}. \quad (2.77)$$

The last step is to bring the energy equation into its conservative form. Therefore, one has to contract (2.66) with n_a and substitute the energy momentum tensor as we did it before

$$\partial_t (\sqrt{\gamma} \rho_H) + \partial_i (\sqrt{\gamma} (\alpha S^i - \beta^i \rho_H)) = -\sqrt{-g} T^{ab} \nabla_a n_b. \quad (2.78)$$

It is possible to describe the conservative equations in a more convenient form

$$\partial_t (\sqrt{\gamma} \vec{U}) + \partial_i (\sqrt{\gamma} \vec{F}^i) = \vec{S}, \quad (2.79)$$

where we used the conserved variables \vec{U} and a flux vector \vec{F}^i in direction i , i.e.

$$\vec{U} = \begin{pmatrix} D \\ S_j \\ \rho_H \end{pmatrix}, \quad \vec{F}^i = \begin{pmatrix} \alpha v^i D - \beta^i D \\ \alpha S^i_j - \beta^i S_j \\ \alpha S^i - \beta^i E \end{pmatrix} \quad (2.80)$$

and a source vector given by

$$\vec{S} = \begin{pmatrix} 0 \\ \frac{1}{2}\alpha S^{ik}\partial_j\gamma_{ik} + S_i\partial_j\beta^i - \rho_H\partial_j\alpha \\ \alpha S^{ij}K_{ij} - S^j\partial_j\alpha \end{pmatrix}. \quad (2.81)$$

The problem with this formulation that is addressed later in chapter 6 is the fact that the primitive variables ρ , v^i and ϵ cannot be expressed trivially in terms of the conservative variables, but rather have to be reconstructed using a root finder. During this step an artificial atmosphere is often employed in the exterior of the stars to prevent the code from having zero densities in the denominator.

2.4.2 Euler equation

In the previous section we discussed the treatment of matter with the focus on evolutions. However, when we want to construct initial data, the emphasis is placed on Euler's equation, which will turn out to be very useful. Taking this into account, we want to give an overview of that equation, starting with the conservation of energy and momentum (2.66), which can easily be written as

$$\nabla_a T^a_b = 0, \quad (2.82)$$

due to the compatibility of the covariant derivative with the metric. We define the canonical momentum 1-form of a fluid element to be

$$\pi_a = hu_a \quad (2.83)$$

and its derivative $(d\pi)_{ab} = \nabla_a\pi_b - \nabla_b\pi_a$ is known as canonical vorticity 2-form. These definitions can be used together with (2.54)–(2.60) to decompose the divergence of the energy momentum tensor (2.50) as

$$\nabla_a T^a_b = \rho(u^a(d\pi)_{ab} - T\nabla_b s) + \pi_b\nabla_a(\rho u^a). \quad (2.84)$$

Equation 2.84 has to vanish due to (2.82) and we can further exploit conservation of rest-mass density (2.65) to obtain the Carter-Lichnerowicz form (Carter [1979]; Lichnerowicz [1941] or more recently summarized by Gourgoulhon [2006]) of Euler's equation

$$u^a(d\pi)_{ab} = T\nabla_b s. \quad (2.85)$$

We focus on barotropic fluids, which means that we assume the matter quantities are only depending on the rest-mass density ρ , which is equivalent to the proper baryon number density n and thus in accordance with our definition of a perfect fluid (2.52). Again, this can be justified with the absence of shock heating and a fluid temperature, which is far below the Fermi temperature for neutron star binaries, as discussed in Friedman and Stergioulas [2013]. Invoking this assumption to simplify equation (2.85) yields a simplified version of the Euler equation

$$u^a(d\pi)_{ab} = 0 \quad (2.86)$$

It is possible to use equation (2.86) to construct a first integral if we take into account the normalization condition $u^a u_a = -1$ and one obtains

$$u^a \nabla_a \mathcal{E} = -\frac{1}{2h} u^a u^b \mathcal{L}_k (h^2 g_{ab}) = 0. \quad (2.87)$$

Here $\mathcal{E} = -k^\alpha \pi_\alpha$ is a constant of the integration. As we discussed in [Mol1], this can be interpreted as streamlines for barotropic flows. These can be seen as geodesics of a Riemannian manifold with a metric $h^2 g_{ab}$ as described in Lichnerowicz [1967]. An alternative derivation of the Euler equation (2.86) can be obtained by minimizing the fluid element action

$$S = \int_{\tau_1}^{\tau_2} L(x, u) d\tau = - \int_{\tau_1}^{\tau_2} h(x) \sqrt{-g_{ab}(x) u^a u^b} d\tau, \quad (2.88)$$

with canonical velocity given by $u^a = dx^a/d\tau$ and canonical momentum given by $\pi_a = \partial L/\partial u^a = hu_a$. Finally, we can invoke Noether's theorem, which states that the quantity

$$\mathcal{E} = -k^\alpha \pi_\alpha \quad (2.89)$$

is conserved along streamlines, if the ε -family of infinitesimal coordinate transformations $x^\alpha \rightarrow x^\alpha + \varepsilon k^\alpha$ is a continuous symmetry of the fluid element action (2.88). This agrees with what we found in equation (2.87) and can be explained geometrically with the conformal metric $h^2 g_{ab}$, which vanishes if it is Lie-derived by k^a , i.e. k^a is a Killing vector.

Model and assumptions

After gathering the general information about initial data in numerical relativity and the treatment of neutron stars in the last sections, we now want to give a more detailed description of the particular scheme we use to construct initial data, especially for neutron stars on orbits with arbitrary eccentricity.

3.1 Gravitational field equations

An overview about the conformal thin-sandwich equations has been given in section 2.2 and we also gave the equations of the extended decomposition, which we use in this work. We have five equations (2.44), (2.49) and (2.43), which we wish to solve for the five metric coefficients ψ , α and β^i on some initial slice Σ_0 . We now assume maximal slicing

$$K = 0 \tag{3.1}$$

$$\partial_t K = 0 \tag{3.2}$$

and spatial conformal flatness, which is also known as Isenberg-Wilson-Mathews [IWM] approximation [Isenberg, 2008; Wilson and Mathews, 1989], with the flat metric f_{ab}

$$\bar{\gamma}_{ab} = f_{ab} \tag{3.3}$$

$$\partial_t \bar{\gamma}_{ab} = 0, \tag{3.4}$$

as well as the preservation of these conditions for a short time. These assumptions allow us to rewrite the extended conformal thin-sandwich equations in a much simpler

form

$$\partial^i \partial_i \psi = -\frac{1}{8} \psi^5 (A_{ij} A^{ij} + 16\pi \rho_H), \quad (3.5a)$$

$$\partial^j \partial_j \beta^i + \frac{1}{3} \partial^i \partial_j \beta^j = 2\psi^{10} A^{ij} \partial_j (\alpha \psi^{-6}) + 16\pi \alpha \psi^4 S^i, \quad (3.5b)$$

$$\partial^i \partial_i (\alpha \psi) = \alpha \psi^5 \left[\frac{7}{8} A_{ij} A^{ij} + 2\pi (\rho_H + 2S) \right]. \quad (3.5c)$$

Here we used Cartesian coordinates, which further simplify $f_{ij} = \delta_{ij}$. The matter terms are given by straightforwardly computing the projections of the stress energy tensor, which was introduced in section 2.1 and from equations (2.73) – (2.75) we obtain

$$\rho_H = \rho h (\alpha u^t - 1)^2 + \epsilon, \quad (3.6a)$$

$$S^i = \rho h \alpha (u^t)^2 \psi^4 (\beta^i + u^i / u^t), \quad (3.6b)$$

$$S = \rho h [(\alpha u^t)^2 - 1] + 3p. \quad (3.6c)$$

Note that the spatial indices are raised and lowered with the flat conformal metric.

At this point we stress the difference of our approach to many other works in the literature, e.g. as reviewed in Baumgarte and Shapiro [2010] or Rezzolla and Zanotti [2013]. It is common to assume maximal slicing (3.1) and spatial conformal flatness (3.3) later on and for now use a time-like Killing symmetry or quasi-equilibrium in order to obtain our imposed condition of preservation for an infinitesimal small time interval (3.2) and (3.4). This means, since we assume maximal slicing (3.1) and spatial conformal flatness (3.3) anyway, we can simply swap the order of assumptions and assume it right now. The advantage is that we can naturally assume that these conditions are preserved in time and we do not have to employ quasi-equilibrium or Killing-symmetry. If we invoke spatial conformal flatness, we do not need a notion of stationarity for the gravitational part of our system. Nevertheless, we discuss the stationarity of the fluid part in section 3.2.

Unfortunately, these assumptions do not come for free. Although the IWM approximation is very helpful in order to simplify the equations and to make the computation of initial data easier, it is known that the metric of a non-spinning binary system is only fulfilling spatial conformal flatness to first post-Newtonian order. Thus the errors introduced might be quite large. In the case of quasi-circular binaries this has been discussed by Johnson-McDaniel et al. [2009] or Rieth and Schäfer [1996], who also include eccentricity in their studies. Hence, it is not possible to obtain a setup

with purely outgoing gravitational radiation and this results in some artificial initial oscillations that can be observed at the beginning of all simulations. A possible method to solve this issue would be the *waveless* approach as suggested by Uryū et al. [2006, 2009], which represents a way to compute constraint solved initial data for binary neutron stars without assuming the IWM approximation. On the other hand, this method has not been studied very well and most groups resort to using the IWM approximation, since studies with black hole binaries have shown that the overall physics is not significantly affected [Garcia et al., 2012].

3.2 Stationary fluid approximation

Until now we have discussed the gravitational part and also the equations that govern the fluid part of our system. However, if we want to construct initial data by solving all equations, we still do not have enough equations to consistently give a solution. We have to invoke another symmetry in order to be able to describe the desired equilibrium character of our system.

3.2.1 Helical symmetry

Before we go into any detail about the more general symmetries that can be employed to construct stars with arbitrary eccentricities, it is necessary to summarize the methods that already have been used. In most cases, people construct initial data for irrotational binaries on circular orbits. The most common choice to describe these circular binaries is to assume that the stars are stationary in a frame that is corotating with the stars. The symmetry vector k_{qc}^a , which describes such stationarity is called *helical Killing vector*

$$k_{\text{qc}}^a = t^a + \Omega_{\text{qc}} \varphi^a = t^a + \Omega_{\text{qc}} (x y^a - y x^a), \quad (3.7)$$

where the vectors $\vec{t} = \vec{\partial}_t$, $\vec{x} = \vec{\partial}_x$, and $\vec{y} = \vec{\partial}_y$ generate translations in the t , x , and y directions, respectively, while $\vec{\varphi} = \vec{\partial}_\varphi$ generates rotations about the z -axis. The subscript qc denotes the quasicircular character of the vector. The idea behind Equation 3.7 is that in strict equilibrium, we should be able to exploit the rotational symmetry of our spacetime to construct two Killing vectors, ∂_t and ∂_φ . Although in case of our quasi-equilibrium binaries we do not have these two Killing vectors, we can construct an approximate Killing vector as a linear combination of those, where Ω_{qc} denotes the orbital angular velocity. This means that the movement along an

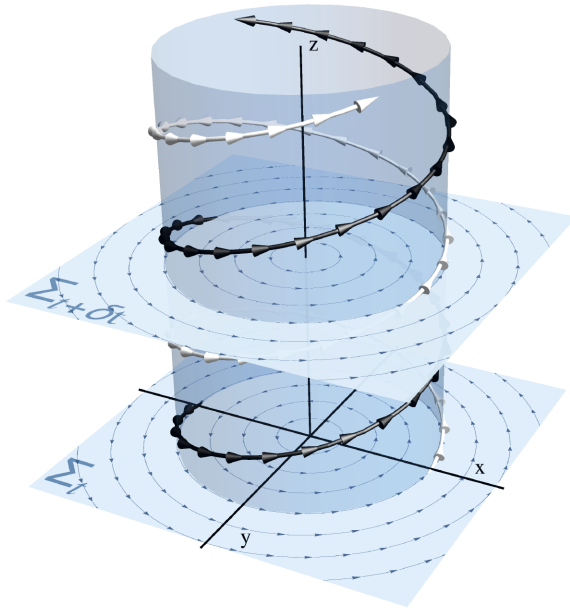


Figure 3.1: Illustrating a helical Killing vector. The black and the white line denote the field vectors at the stars center. Two time slices are shown, where the x and y components of the vector field are inscribed.

angle $d\phi = \Omega_{\text{qc}} dt$ within a time dt would leave the spacetime invariant, or expressed mathematically $\mathcal{L}_{k_{\text{qc}}} g_{ab} = 0$.

In order to construct initial data for neutron stars, we have to find a matter distribution that is in equilibrium with the gravitational field. Therefore, a rotation of our system at time t_1 along the helical Killing vector k_{qc} has to be able to generate the configuration of the binaries at an arbitrary time t_2 . As discussed in Baumgarte and Shapiro [2010], for the fluid quantities ρ and u^a this can be expressed by Lie dragging them along k_{qc} , i.e.

$$\mathcal{L}_{k_{\text{qc}}} \rho = 0 \quad \text{and} \quad \mathcal{L}_{k_{\text{qc}}} u^a = 0. \quad (3.8)$$

In order to make this more explicit, we exploit stationarity of the system in a rotating frame, which lets us utilize Noether's theorem (2.89) and (2.87) to obtain the energy in a rotating frame

$$\mathcal{E} = -k^a \pi_a, \quad (3.9)$$

which is conserved along streamlines. In analogy to the Jacobi constant of motion of test particles on Newtonian orbits [Carter, 1979], this quantity is also often called *injection energy*, as in Friedman and Stergioulas [2013].

Many other groups have set up self-consistent field methods to construct initial data,

where they use the fact that the injection energy is constant throughout the star for irrotational or corotating binaries [Bonazzola et al., 1999; Foucart et al., 2008; Gourgoulhon, 1998; Price et al., 2009; Shibata, 1998; Teukolsky, 1998].

In [Mol1], we showed that this conservation law can be derived from Cartan's identity [Carter, 1979; Gourgoulhon, 2006] and that it can be interpreted as a relativistic generalization of the strong Bernoulli principle. The Cartan identity relates the Lie derivative operator \mathcal{L} to the exterior derivative operator d . In case of a vector \vec{u} and a differential form ω , it states

$$\mathcal{L}_u \omega = \vec{u} d\omega + d(\vec{u}\omega). \quad (3.10)$$

Particularly, we obtain

$$\mathcal{L}_k \pi_a = k^b (d\pi)_{ba} + \nabla_a (k^b \pi_b) = 0, \quad (3.11)$$

and given a flow u^a parallel to k_{qc} as it is true for rigid rotation or rigid translation, the first term of (3.11) vanishes by considering Euler's equation (2.86).

For irrotational flows, the situation is slightly more complicated, but the above term vanishes as well, since the canonical vorticity is vanishing for some potential Ψ

$$\pi_a = \nabla_a \Psi \Leftrightarrow (d\pi)_{ab} = \nabla_a \pi_b - \nabla_b \pi_a = 0. \quad (3.12)$$

So we can see that for both types of flows the first term in (3.11) is vanishing, which implies that the injection energy (3.9) is constant throughout the star:

$$\nabla_a \mathcal{E} = 0. \quad (3.13)$$

The approximation of irrotational stars is rather common and is a natural choice since the spin frequencies of the stars are known to be much smaller than the orbital frequency for the last orbits before merger. However, we use a more generalized ansatz with arbitrary spins later on.

3.2.2 Constant three-velocity approximation

From this point on, the basic idea to proceed is the following: we would like to take the integrated Euler equation to derive an expression for the time component of the four velocity u^t and together with the normalization condition $u^a u_a = -1$ this can be further used to find an algebraic expression for the enthalpy h . Thus we would

be able to compute the enthalpy profile (and with a given EoS we could obtain the other fluid quantities) as a function of the gravitational quantities α , β^i , ψ .

However, depending on the flow we want to construct, this task can be complicated. While corotating binaries yield a simple algebraic expression in the way we outlined, irrotational flows are more troublesome. In the latter case, the obtained algebraic equation additionally depends on the velocity potential Ψ , which can be computed with the help of another elliptic equation. A common way to do this is to insert the canonical vorticity (3.12) in the continuity equation (2.67), which yields

$$\nabla_a \left(\frac{\rho}{h} \nabla^a \Psi \right) = 0. \quad (3.14)$$

In order to solve this elliptic equation, one has to impose boundary conditions at the star's surface, which is technically complicated and typically requires special coordinates. Since we want to give the possibility to compute initial data with simpler existing codes, we have to find an appropriate way to solve (3.14) without surface-fitting coordinates or an approximation that circumvents these problems. In particular the multigrid solver we use for testing our new method, works with Cartesian coordinates and cannot be straightforwardly generalized. Hence, we take advantage of Kelvin's circulation theorem [Friedman and Stergioulas, 2013], which states that in an ideal barotropic fluid, an initially irrotational flow will remain irrotational at later times. We assume a homogeneous fluid three-velocity, which means the velocity measured by coordinate observers is approximated as constant throughout the fluid. Since we are free to specify the initial position of the stars, we assume that the binary start at maximal distance of its elliptic orbit, i.e. at apoapsis. The coordinate system is chosen such that the x -axis goes through the stellar centers, which means that each of the stars is initially moving rigidly in y -direction with an instantaneous four-velocity

$$u^a = u^t (t^a + v^y y^a), \quad (3.15)$$

where we introduced the instantaneous three-velocity of a fluid element measured by a coordinate observer $v^y := u^y/u^t = dy/dt$. The Lorentz factor u^t can be obtained through the normalization condition $u^a u_a = -1$, which yields

$$u^t = [-g_{tt} - 2g_{ty}v^y - g_{yy}(v^y)^2]^{-1/2}. \quad (3.16)$$

The parameter v^y is approximated to be constant throughout the fluid, but with different sign for each star and also with different magnitudes if one wants to construct

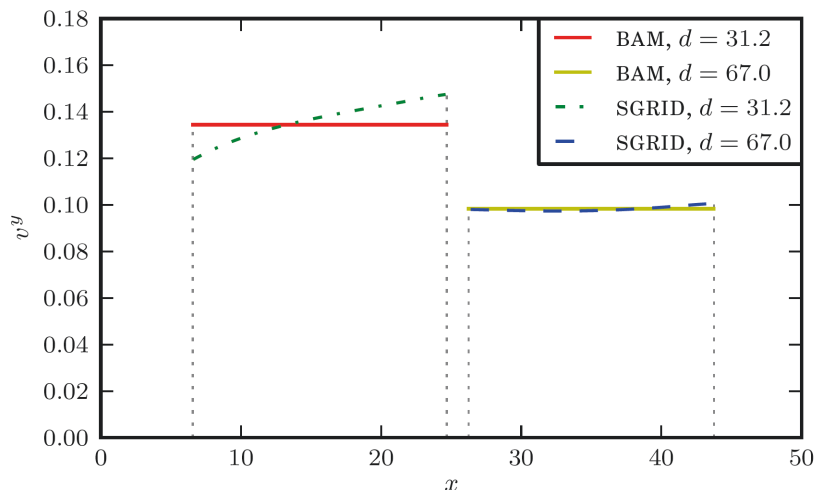


Figure 3.2: Shown are two different implementations (in BAM, respectively in SGRID) of the initial data scheme, where the first is using the constant three-velocity approximation (solid lines) and the latter performs a full solve for the velocity potential (dashed lines). We vary the coordinate distance d of the stars’ centers from $67 \simeq 100\text{km}$ to $31.2 \simeq 47\text{km}$ (note that $M_{\odot} = 1$) and compare the y -component of the fluid velocity along the x -axis. The thin dotted vertical lines denote the star’s surfaces, where the data is cut, because the velocity is not well-defined in the outer region. Plot adopted from [Mol1].

the most generic setup.

In the general relativistic case for irrotational, compressible fluids, this assumption is an approximation that becomes better if we increase the distances or decrease the velocities, i.e. if we consider less relativistic setups. However in the limit of incompressible Newtonian flows, the constant three-velocity assumption is exact as we show in a small calculation in appendix B.

After implementing the initial data scheme using the constant three-velocity assumption and also a “full” scheme, where we solve for the velocity potential using surface fitting coordinates, we were able to compare both versions. The results are shown in Figure 3.2, where we see the parameter v^y for different distances, given in terms of the separation of both star’s coordinate centers. At a distance of 47km, the deviation of the fully-solved fluid three-velocity from a constant is clearly visible and is roughly $\sim 10\%$. However, if we increase the distance to 100km and calculate v^y from solving the velocity potential, the deviation from the approximated constant velocity reduces to $\sim 1\%$. As we will see later, we do not restrict ourselves to the constant three-velocity assumption (3.15), but we use it as a method to easily implement our method on Cartesian grids. We drop the assumption in more complicated codes,

which provide surface fitting coordinates and the way of solving the elliptic equation for the velocity potential is outlined in the following section.

3.2.3 Full velocity potential and spin

In section 3.2.1, we assumed to have a symmetry vector and constructed a first integral of the Euler equation using Cartan's identity. We solved that equation and had to know the fluid velocity, which we approximated in Sec. 3.2.2 instead of computing $u_a = h^{-1}\nabla_a\Psi$, because Ψ would be determined with an elliptic equation (3.14). At this point, we do want to solve this elliptic equation and we could do this by eliminating the time derivatives $\partial_t\Psi$ in (3.14) by using (2.89) (see [Friedman and Stergioulas, 2013] or briefly sketched in [Mol1]). However, we now also want to describe the way Tichy added arbitrary spins to neutron stars in his code SGRID, thus we adopt his notion of constructing the first integral of the Euler equation for spinning stars and the velocity potential¹. The original derivation is given in [Tichy, 2011] for circular binaries (see also [Tichy, 2012] for more details), but can be adopted without changes (apart from the symmetry vector) for eccentric stars. The necessary assumptions are briefly described below, cf. [Mol3].

The starting point is given by Shibata [1998] who decomposes the four velocity u^a into a piece along the symmetry vector and a piece orthogonal to it

$$u^a = u^t(k^a + V^a), \quad (3.17)$$

with $u^t = -u^a n_a / \alpha$. The assumption (3.11) we used in the irrotational case in Section 3.2.1 is not valid for general spins, as shown in Appendix A of Tichy [2011]. Instead, we split the canonical 3-momentum 1-form of a fluid element $\pi_i = \gamma_i^a \pi_a$ into an irrotational part which can be written as the gradient of a potential, $D_i\phi$, and a rotational part w_i :

$$\pi_i = D_i\phi + w_i. \quad (3.18)$$

Furthermore, three reasonable assumptions are made

$$\mathcal{L}_k(\rho u^t) = 0, \quad (3.19a)$$

$$\gamma_i^a \mathcal{L}_k(\nabla_a\phi) = 0, \quad (3.19b)$$

$$\gamma_i^a \mathcal{L}_{\bar{k}} w_a = 0, \quad (3.19c)$$

¹Note that we give a derivation of the first integral for spinning stars in the appendix of [Mol3], which uses Cartan's identity and is shorter than the original derivation. Since it has slightly stronger assumptions we stick with the original one here.

where the vector

$$\bar{k}^a := \frac{\nabla^a \phi}{hu^0} =: k^a - \Delta k^a, \quad (3.20)$$

is parallel to the worldline of the star's center and is used to denote the stationarity of the rotational piece. With some effort, one can now derive the relations

$$\begin{aligned} \gamma_i^b \mathcal{L}_k p_b &\stackrel{(3.19b)}{=} \gamma_i^b \mathcal{L}_k w_b = \gamma_i^b \mathcal{L}_{\bar{k}+\Delta k} w_b \\ &\stackrel{(3.19c)}{=} \gamma_i^b \mathcal{L}_{\Delta k} w_b = {}^{(3)}\mathcal{L}_{\Delta \bar{k}} w_b, \end{aligned} \quad (3.21a)$$

$$V^i + \Delta \tilde{k}^i \stackrel{(3.17)}{=} \frac{u^i}{u^t} - k^i + \Delta k^i = \frac{u^i}{u^t} - \bar{k}^i \stackrel{(3.18)}{=} \frac{w^i}{hu^t} \quad (3.21b)$$

$${}^{(3)}\mathcal{L}_{V+\Delta \tilde{k}} w_i = \frac{w_i}{hu^0} {}^{(3)}\mathcal{L}_{\frac{w}{hu^0}} hu^0 + w^j {}^{(3)}\mathcal{L}_{\frac{w}{hu^0}} \gamma_{ij} \approx 0. \quad (3.21c)$$

where Δk^a is given by $(0, \Delta \tilde{k}^i)$ and (3.21c) used the fact that hu^t and γ_{ij} are approximately constant along $\frac{w^i}{hu^t}$. The continuity equation (2.67) can be written in terms of k^a and V^a and can be formulated as

$$D_i(\rho \alpha u^t V^i) + \alpha[\mathcal{L}_k(\rho u^t) + \rho u^t g^{ab} \mathcal{L}_k g_{ab}]. \quad (3.22)$$

Further following Tichy, this can be simplified through assuming

$$\rho_0 g^{ab} \mathcal{L}_k g_{ab} = \rho_0(12\mathcal{L}_k \ln \psi + 2\mathcal{L}_k \ln \alpha) \approx 0, \quad (3.23)$$

which follows from our metric assumptions (also compare the discussion about the minimal assumption necessary in appendix of [Mol3]). Plugging (3.17) into the continuity equation (2.67) and using (3.23) and (3.19a) we obtain

$$D_i(\rho_0 \alpha u^0 V^i) = 0. \quad (3.24)$$

Next, the Euler equation (2.86) can be reformulated with the help of (3.21a), (3.21b), and (3.21c) and integrated

$$\frac{h}{u^t} + V^j D_j \phi = -\mathcal{E} = \text{const.} \quad (3.25)$$

As we describe in section 4, we choose \mathcal{E} such that the baryonic mass is kept constant. The generic expression of the velocity is given by

$$V^i = \frac{D^i \phi + w^i}{hu^t} - (\beta^i + k^i), \quad (3.26)$$

thus the continuity equation can finally be written as

$$D_i \left[\frac{\rho\alpha}{h} (D^i\phi + w^i) - \rho\alpha u^t (\beta^i + k^i) \right] = 0. \quad (3.27)$$

Equation (3.27) represents the nonlinear elliptic equation in ϕ which was mentioned earlier, where we have to know the boundary conditions at the stars' surfaces. SGRID uses surface-fitted coordinates to handle this issue, which are described in Sec. 4.4. The normalization condition $u^a u_a = -1$ can be used to compute h as a function of the elliptic quantities, analogues as we did in the previous section.

$$h = \sqrt{L^2 - (D_i\phi + w_i)(D^i\phi + w^i)}, \quad (3.28)$$

with

$$L^2 = \frac{b + \sqrt{b^2 - 4\alpha^4 [(D_i\phi + w_i)w^i]^2}}{2\alpha^2}, \quad (3.29a)$$

$$b = [(k^i + \beta^i)D_i\phi - C]^2 + 2\alpha^2(D_i\phi + w_i)w^i. \quad (3.29b)$$

3.2.4 Eccentric orbits

In section 3.2.1 we described how helical symmetry is often used to construct stars on circular orbits. In this section we describe how we extended this scheme in order to be able to generate non-circular orbits. It is not possible to describe eccentric binaries using the notion of helical symmetry, since eccentric binaries are not stationary in a rotating frame². However, a simple way to construct initial data for binaries on arbitrary orbits has been used by e.g. Gold et al. [2012] or Stephens et al. [2011]. Their solution is to boost two superimposed, spherical stars in arbitrary (most often opposite) directions. Later implementations like East et al. [2012b] additionally solve for the Einstein constraints, but not for the Euler equation. Other groups [Alic et al., 2013] suggested to use inconsistent initial data along with constraint damping evolution schemes, such as Z4c, in order improve accuracy. However, constraint damping is not guaranteed to yield physically meaningful data and we are even able to construct constraint solved data, which behaves unphysically if we choose unsuitable frames of stationarity. On the other hand, this approach is justified if the obtained violations are comparably small with respect to constraint solved data and the evolutions

²Note that we use the term “stationary” in a sense that neglects higher order contributions, in particular gravitational wave radiation. This allows us to say that stars on circular orbits are stationary in a rotating frame.

always behave properly in a physical sense. Obviously, the best solution would be to construct constrained, consistent initial data and then evolve these data with constraint damping evolution schemes. For accurate investigations we employ exactly this combination of initial data and evolutions.

In the works cited above, interesting physical results can be found, especially the f -mode oscillations of highly eccentric neutron stars [East and Pretorius, 2012; Gold et al., 2012] and black hole-neutron star binaries [East et al., 2012a; Stephens et al., 2011]. Nevertheless, it is possible that these oscillations are spuriously excited due to inconsistencies within the initial data. Hence we have to provide further numerical evidence to rule out such issues.

Following our investigation in [Mol1], we can distinguish between four different approximations that are hidden in the superimposed data:

- (i) The metric obtained via superposition of boosted spherical stars gives rise to violations of the Einstein constraint equations, which are much stronger than the violations in typical evolutions. The other three approximations can be found regarding the fluid part of the data and would only be exact at infinitely large separations:
- (ii) Since the stars are spherical by definition, they obviously lack tidal deformation.
- (iii) Boosting the stars in different directions leads to data that are spherical in a linearly comoving frame (in a Lorentzian sense) rather than in a corotating frame.
- (iv) The initial velocity is assumed to be homogeneously constant throughout each star.

Coming straight to our implementation and anticipating some of the results, the scheme allows us to separately estimate the influence of these approximations. Looking at an evolution of purely boosted TOV stars, it is striking how the central densities (here in terms of rest-mass, but of course this is true for all related quantities) oscillate around 20%. We will see that solving the constraint equations and allowing for tidal deformations, i.e. getting rid of assumption (i) and (ii), does not improve the quality of the initial data and still leads to similar oscillations. Contrary, we will find that retaining the constant velocity approximation (iv) and dropping assumption (iii) drastically decreases the spurious oscillations, which led us to the conclusion that the main source of error is given by assuming stationarity in a linearly comoving frame. Finally, we will see that the second largest source of error is given by assumption (iv), which can be relaxed later.

So the idea is to eliminate the artificial oscillations by finding a proper notion of stationarity. We found two equivalent ways to tackle this problem, where one is based on geometric arguments and the other is a more “physical” ansatz.

Physical approach

We start with the latter, by formulating the problem differently: we seek a generalization of the vector field (3.7) for which the energy (3.9) is approximately constant. Similarly to the quasicircular case, we are free to specify an arbitrary location of the stars with respect to the coordinate system. On the basis of Keplerian orbits, we choose the stars with masses m_1 and m_2 to be initially located at apoapsis on the x -axis. This is a good choice in particular, since it maximizes the distance of the stars and thus improves the constant three-velocity approximation. Also, it represents a moment of time symmetry, due to the vanishing radial velocity. We write

$$x_1 = a(1+e)\frac{m_2}{m_1+m_2} + x_{\text{cm}}, \quad (3.30a)$$

$$x_2 = -a(1+e)\frac{m_1}{m_1+m_2} + x_{\text{cm}}, \quad (3.30b)$$

where the “position” of a star is given by its maximum rest-mass density. In the above equations x_{cm} describes the center of mass (there is no y -component, since the stars are placed on the x -axis) and $e = \sqrt{1 - b^2/a^2}$ expresses the eccentricity of the ellipse in terms of the semimajor axis a and the semiminor axis b . It is important to note that e is not necessarily the eccentricity of the computed orbits, since fully general relativistic evolutions are certainly causing the stars to inspiral and thus deviate from Newtonian point particle ellipses. e can rather be seen as a parameter to monotonically adjust the output eccentricity of the data, where we define a notion of eccentricity for inspiralling orbits later.

If we are able to find a vector field k^α which approximately Lie-derives the flow that is assumed to be irrotational, then we can use the Cartan identity (3.11) as for quasicircular orbits and yield similar constant injection energy \mathcal{E} as before in equation (3.9). A natural choice to generalize this vector field is to manipulate the tangential velocity of the stars. Assuming the binary is in a quasicircular configuration, then decreasing the tangential part of the initial three-velocity of the stars will inevitably lead to an elliptic configuration, where the stars are at apoapsis. For our choice of coordinates this corresponds to applying a boost along the y -direction to (3.7), which yields

$$k^a = t^a + \omega \varphi^a + \lambda y^a. \quad (3.31a)$$

We refer to this vector field as “*helliptical*” vector or more strictly speaking *instantaneously inscribed helical vector*, which we justify later within the more geometrical approach section. Similar to the orbital frequency Ω_{qc} we introduce a rotation fre-

quency ω , however, both quantities are not equal in general. The boost parameter λ is chosen on physical grounds. For example, setting $\lambda = v^y$ and $\omega = 0$ would lead to $k^a = t^a + v^y y^a$, which implies stationarity in a linearly comoving frame. On the other hand, we can rewrite the boost parameter as a displacement parameter x_c , where $\lambda = -\omega x_c$, which then reads

$$k^a = t^a + \omega [(x - x_c)y^a - y x^a]. \quad (3.31b)$$

Stationarity in a linearly comoving frame is not a good assumption as we already mentioned before and a short calculation in appendix A shows why spurious oscillations are to be expected within this approximation. In fact, one should rather choose $\omega \neq 0$ and comparing (3.31a) to (3.7) it is obvious by construction that the circular limit is recovered for vanishing λ and x_c respectively.

In order to give a more concrete, reasonable choice of ω , we considered the limit of incompressible binaries on Newtonian eccentric orbits, for which equation (3.11) has to hold exactly. For a more detailed calculation we refer again to the appendix B. For the mean motion $\bar{\Omega} = 2\pi/T$ (with an orbital period T), we find the expression

$$\bar{\Omega} = \omega(1 + e)\sqrt{1 - e^2}. \quad (3.32)$$

The second parameter λ , respectively x_c can be found by demanding u^a and k^a to be initially parallel at the stars' centers. A simple comparison of (3.31a) to (3.15), with a substitution of (3.30) yields

$$\lambda_{1,2} = -\omega x_{c1,2} = -v_{1,2}^y \frac{e}{1 - e} - \omega x_{\text{cm}}. \quad (3.33)$$

Both parameters are connected via the relation

$$v_{1,2}^y = \omega(1 - e)(x_{1,2} - x_{\text{cm}}) \quad (3.34)$$

Here we immediately see the desired behavior of the tangential velocity component as it vanishes for $e = 1$ and results in a head-on collision. On the other hand, the limit of circular orbits is recovered for $e = 0$.

In this approach, we were utilizing the limit of incompressible Newtonian stars to find the required parameters. In the next section, we show an equivalent, but on some level more elegant way to obtain the result.

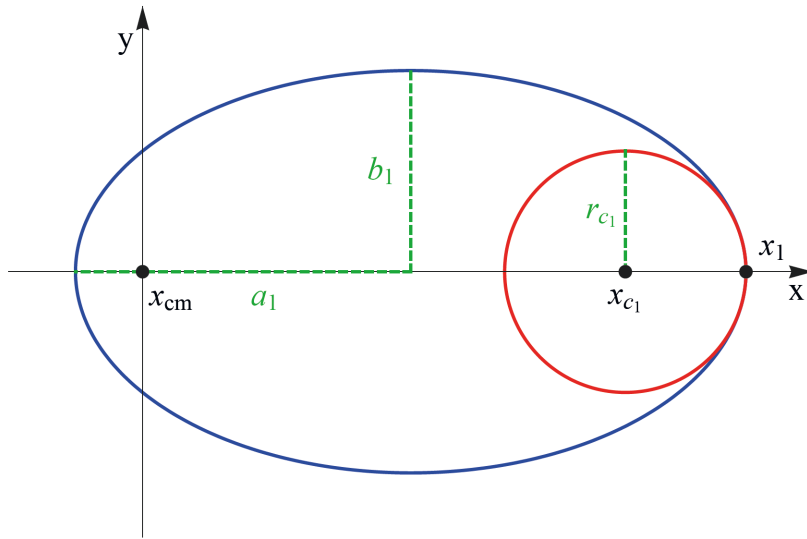


Figure 3.3: An illustration of the approximation of the orbits by using circles inscribed into the orbital ellipse in a way that their curvature is the same as the one of the ellipse. We show the scaled semimajor axis $a_1 = a \frac{m_2}{M}$, semiminor axis $b_1 = b \frac{m_2}{M}$, and the radius $r_{c_1} = b_1^2/a_1$ and center x_{c_1} of the inscribed circle as well as the center x_1 of one of the stars. The center of mass is denoted by x_{cm} . Plot taken from [Mol1].

Geometrical approach

The following derivation was first described in [Mol1] and later on in [Mol3]. We use Fig. 3.3 to support the calculations with a schematic representation. The idea is to generalize the standard helical Killing vector to an approximate helical symmetry vector by making three reasonable assumptions:

- (i) There exists a vector k^α that approximately Lie-derives the flow.
- (ii) k^α is along the motion of the star center.
- (iii) Each star's center moves along a segment of an elliptic orbit at apoapsis. We can use assumption (iii) to specify the kind of orbit we want to construct. We do not need a complete orbit for the construction, but only a small segment of an orbit near apoapsis, which allows us to model this segment by a circle that is inscribed into the ellipse (see Fig. 3.3). It is straightforward to see that the radius of such a circle depends on the eccentricity and on the semimajor axis of the ellipse. The curvature of a circle with radius R_c is given by $-1/R_c$, while the curvature of an ellipse (with semimajor and semiminor-axis A and B) at apoapsis is given by $-A/B^2$. Thus, an inscribed circle has to have the radius $R_c = (1 - e^2)A$. In Newtonian theory we know that two particles with masses m_1 and m_2 are orbiting around each other on ellipses with semimajor axes $a_{1,2} = d_{1,2}/(1 + e)$, where $d_{1,2}$ denotes the maximal distance of each particle from the center of mass. In our case this leads to radii of the inscribed

circles

$$r_{c_{1,2}} = (1 - e)d_{1,2}. \quad (3.35)$$

In order to find the centers of these circles, we have to consider the stars positions and subtract their radii

$$x_{c_{1,2}} = x_{1,2} \mp r_{c_{1,2}} = x_{\text{cm}} + e(x_{1,2} - x_{\text{cm}}), \quad (3.36)$$

where the distance was replaced by $d_{1,2} = |x_{1,2} - x_{\text{cm}}|$ and the upper and lower signs are belonging to the different stars as they are denoted by subscripts 1 and 2. Assumption (ii) is necessary, since if k^a is not along the motion of the star center, k^a can never be an approximate Killing vector. So, our the symmetry vector k^a must be along the trajectory of the particles, which can be approximated by two circles centered at $x_{c_{1,2}}$ with radii $r_{c_{1,2}}$. Let us assume that the angular velocity of these two particles along the circles is given by ω_1 and ω_2 . We can further assume that the center of mass is at rest and conservation of momentum yields

$$m_1\omega_1r_{c_1} = m_2\omega_2r_{c_2}. \quad (3.37)$$

We obtain the balance $m_1d_1 = m_2d_2$ from the definition of the center of mass and together with Equation 3.35 it is straightforward to see that

$$m_1r_{c_1} = m_2r_{c_2}. \quad (3.38)$$

Finally, we can combine (3.37) and (3.38) to see that both frequencies have to be the same

$$\omega_1 = \omega_2 =: \omega. \quad (3.39)$$

Altogether, this means that the symmetry vector should look like

$$k_{1,2}^a = t^a + \omega [(x - x_{c_{1,2}})y^a - y x^a]. \quad (3.40)$$

A nice property that comes along with the identity of the frequencies is that although k_1^a and k_2^a look different, there is only one approximate Killing vector at large distances since $x \gg x_{c_{1,2}}$.

If we make the constant three velocity approximation (3.15), assumption (ii) also tells us how to choose the velocity parameter

$$v_{1,2}^y = \pm\omega r_{c_{1,2}} = (1 - e)\omega(x_{1,2} - x_{\text{cm}}). \quad (3.41)$$

In order to provide further consistency checks of our derived equations, we consider the Newtonian limit and see whether the vector k^a leads to the correct physics. We use a *force balance* equation to compute ω , which has the form (3.13) and can be simplified in the Newtonian limit to be

$$\bar{D}_i \mathcal{E} = 0, \quad (3.42)$$

where the injection energy in star 1 is given by

$$\mathcal{E} = \frac{1}{2}v^2 + \Phi + h - \omega [(x - x_{c1})v^y - yv^x] \quad (3.43)$$

and Φ is the Newtonian gravitational potential and \bar{D} denotes the covariant derivative in flat Euclidean space. Assuming that the stars are far apart, then they are almost spherical and the orbits are approximately elliptic. In this case, the potential due to star 2 can be approximated as that of a point mass by $\Phi = -Gm_2/\|\vec{x} - \vec{x}_2\|$ and we neglect the gradient of star 1's potential at its center. Note that factors of G are shown explicitly so that the distinction between the gravitational and centripetal forces becomes more clear. We take (3.42) and evaluate it at the center of the star $x = x_1$. Here, the density is maximum and for the enthalpy this yields a vanishing derivative $\partial_x h_{x=x_1} = 0$, hence we obtain

$$G\frac{m_2}{r^2} - \omega v^y = 0, \quad (3.44)$$

where r is the separation of the stars. Inserting (3.41) gives

$$G\frac{m_1 m_2}{r^2} = m_1 \omega^2 r_{c1}, \quad (3.45)$$

which shows that ω yields a centripetal force, which is needed to keep star 1 on the inscribed circular orbit, and is exactly provided by the gravitational force due to star 2. Further it is straightforward to see that (3.45) can be used together with relation (3.32) and (3.35) to obtain

$$G\frac{m_2}{r^2} = \bar{\Omega}^2 \frac{a_1}{(1+e)^2}, \quad (3.46)$$

where we can further substitute $r = a(1+e)$ to obtain Kepler's third law

$$\bar{\Omega}^2 = \frac{G(m_1 + m_2)}{a^3}. \quad (3.47)$$

The above paragraphs demonstrate how it is possible to give a geometrical interpretation of the symmetry vector and thus justifies the term *instantaneously inscribed*

helical vector field, since it generates time translations in a frame that rotates about a point $(x_{c_{1,2}}, 0, 0)$. In the circular case, the integral curves of the helical Killing vector field coincide with the trajectory of the star center when we project them onto a spatial slice Σ_t . However, in the elliptic case, the projections of the integral curves are given by circles, which are inscribed into the elliptic trajectory at apoapsis. The center of those circles is placed at $(x_{c_{1,2}}, 0, 0)$, while the radius is given by $r_{c_{1,2}}$, corresponding to the radius of curvature of the ellipse at apoapsis. Only initially at $t = 0$, the trajectory of the star is tangent to the integral curves of the symmetry vector field. Additionally, the injection energy (3.9) is only spatially constant, but not conserved in time. This means, for $t = 0$ the energy is constant throughout the fluid, while this is violated for $t > 0$, which is why we call the symmetry vector *instantaneous*. Nevertheless, operating with $k^a \partial_a$ on the vector yields

$$\partial_t \mathcal{E} + k_{1,2}^i \partial_i \mathcal{E} = 0, \quad (3.48)$$

and since the injection energy is spatially constant, the time derivative has to vanish initially as well. Since (2.87) is satisfied, one could call $k_{1,2}^a$ approximate Killing vectors for the regions of spacetime occupied by each star.

3.2.5 Generalized orbits with radial velocity

There are several ways how one could further generalize the symmetry vector. One starting point is the construction of initial data that are not at apoapsis, but at an arbitrary other time. Based on the previous description in section 3.2.4, we can straightforwardly generalize the inscribed circles to be inscribed into an arbitrary position of the elliptic trajectory. This complicates the equations and the “heliptical” vector takes the form

$$k^a = t^a + \omega [(x - x_c)y^a - (y - y_c)x^a], \quad (3.49)$$

where we have an additional parameter y_c . However, this generalization comes with many disadvantages, since other points than apoastron naturally correspond to smaller separations and the approximations we made becomes worse. Non-vanishing radial derivatives increase the bad properties such as lower iteration stability and increased artificial oscillations. On the other hand, we do not see the need for constructing stars at different locations. Thus we have not tested this generalization in detail and restrict ourselves to the case $y_c = 0$

A much more promising extension of our scheme is to add radial velocity to the stars and allow for a slow inspiral of the orbit. This inspiral is expected due to the emission of gravitational wave radiation, hence it has to be present initially as well. Simply setting the eccentricity parameter e to zero generates helically symmetric data, but neglects these initial radial velocity components. The consequence are intrinsic residual eccentricities, which lead to an oscillatory behavior of the separation as seen in Kyutoku et al. [2014] and thus pollute the data. When incorporating radial velocity it is useful to look back at our three assumptions from the geometrical approach in section 3.2.4. Considering assumption (ii), we see that assumption (iii) has to be modified to include a radial part. The approximate Killing vector then takes the form

$$k_{r1,2}^a = k_{1,2}^a + \frac{v_r}{r} r^a = t^a + \omega [(x - x_{c1,2})y^a - yx^a] + \frac{v_r}{r} r^a, \quad (3.50)$$

where $r^a = (0, x, y, z)$ is a vector pointing in radial direction and r is again the separation of the star's centers. Note that we drop the subscript r of the vector and just denote it by $k_{1,2}^a$, since it is sufficient to say that we set $v_r = 0$ in many cases and mention explicitly if we use the full vector. A scheme that uses this new vector $k_{1,2}^a$ needs to provide a way to compute the parameter v_r . A possible method is given by approximating it with post-Newtonian or effective-one-body theory, where one can possibly add tidal correction terms to take the finite size of the stars into account. Read et al. [2009a] used a similar technique to decrease the eccentricity, where they applied a Lorentz boost in radial direction based on post-Newtonian theory in the point particle limit and they obtained significantly lower eccentricities than in previous simulations without such improvements [Read et al., 2013].

Other techniques require to change both, the radial and the tangential velocity of the stars. We are able to change the tangential velocity by varying the eccentricity parameter e as it changes the y -component of the fluid three-velocity by construction. Several other groups [Husa et al., 2008; Mroué and Pfeiffer, 2012; Pfeiffer et al., 2007; Pürrer et al., 2012; Tichy and Marronetti, 2011] used evolved data of black holes in order to find parameters which improve the tangential and radial velocity so that the residual eccentricity was minimized. We are now able to do the same for neutron stars, where we start with $e = 0$ and $v_r = 0$ and evolve the data for a short period of time (usually one to one and a half orbits) and then iteratively find better parameters. We describe the iteration method later in section 5.3. Note that while we were investigating this type of eccentricity reduction, Kyutoku et al. [2014] have set up a similar method with slightly different treatment of the tangential velocity but also suitable for neutron star binaries.

Numerical method

So far, we have described the model we want to use for the implementation including the approximations we have made. In this section discuss the numerical method to solve the equations, where start by summarizing the recipe to construct initial data through an iterative self-consistent method by gathering the accumulated results from previous sections. Then we briefly discuss the preferred technique to solve elliptic equations in our Cartesian finite-differencing implementation BAM. The implementation itself is considered in more detail in the subsequent section and at last, we describe the pseudo-spectral SGRID code, where we implemented our scheme using surface fitting coordinates.

4.1 Iteration recipe

The general concept of finding initial data for neutron star binaries has been reduced to finding solutions to the elliptic conformal thin-sandwich equations (3.5), which also satisfy the first integral of the Euler equation (4.1). In other words, we want to end up with expressions for the matter density profile h (and thus ρ , p , etc ... via some specified EoS) and for the five elliptic gravitational quantities ψ , α and β^i . To tackle this task, we use the hellicptical vector from (3.31 *a*) and compute the first integral (3.9) to the relativistic Euler equation (2.86)

$$\mathcal{E} = -h\{u_t + \omega [(x - x_c) u_y - y u_x]\}. \quad (4.1)$$

For simplicity, we just consider the case of the constant three-velocity approximation (3.15) for now, thus we can write

$$u_a = g_{ab}u^b = u^t(g_{at} + v^y g_{ay}). \quad (4.2)$$

The start of the iteration scheme has to be made with an initial guess. It turns out that the method is rather sensitive to the initial guess and whether the code converges or not, crucially depends on the quality of this guess. Usually, a good initial guess is given by superimposing two single neutron stars. Solutions to Einstein's equations for such isolated objects have been extensively studied and are fairly easy to construct. Our initial guess is basically the type of initial data that was used in Gold et al. [2012] and we proceed in the same way to construct it: The first step consists of computing the solution to the Tolman-Oppenheimer-Volkoff (TOV) equations [Oppenheimer and Volkoff, 1939; Tolman, 1939]. These solutions are non-rotating and spherical and the stars are constructed such that either the central density or the baryonic mass is the same as for the desired initial data. The exact choice depends on the quantity that is chosen to be fixed during the iteration process. The second step is to boost the computed solutions by applying a Lorentz transformation in the $\pm y$ direction, which approximates the orbital motion. Finally, the two boosted stars are superimposed by adding their metrics and subtracting the flat Minkowski metric η_{ab} . This yields

$$g_{ab}^{(\text{sup})} = g_{ab}^{(1)} + g_{ab}^{(2)} - \eta_{ab}, \quad (4.3)$$

where $g_{ab}^{(1,2)}$ denotes the metric of star 1 and star 2 respectively. Now we have an approximate solution and the metric serves as an initial guess for the elliptic quantities. Therefore, ψ^4 is taken to be the xx component of the 3-metric, since the boost prohibits spatial conformal flatness. The density profile is simply initialized by setting it to the TOV solution.

Finding an initial guess is only the first obstacle. In the next step, this guess is used to solve the XCTS equations (3.5) for fixed source terms. This can be done with an elliptic solver, but the result will not satisfy the matter equations. However, we know the metric and can use (3.15) with the normalization condition $u_a u^a = -1$, yielding

$$u^t = (-g_{tt} - 2g_{ty} - g_{yy}v_y^2)^{-1/2} \quad (4.4)$$

to find the time component of the fluid four-velocity. The remaining components can be constructed via

$$u_t = \beta^i u_i - \alpha \sqrt{\gamma^{ij} u_i u_j + 1} \quad (4.5a)$$

$$u^i = g^{it} u_t + g^{ij} u_j = \gamma^{ij} u_j - \alpha^{-1} \beta^i \sqrt{\gamma^{jk} u_j u_k + 1} \quad (4.5b)$$

Additionally to the metric (and thus ψ , α and β^i), we now have the fluid four-velocity

u^a at hand and want to solve the integrated Euler equation (4.1) for the enthalpy h . However, we are still missing a value for ω (and also λ , resp. x_c , but these are given in terms of ω and the center of mass x_{cm} by equation (3.41) or (3.33)) and for $\mathcal{E}_{1,2}$. In short this means that we are left with four parameters that have to be calculated, namely the orbital frequency ω , the center of mass x_{cm} , and the injection energy of each star $\mathcal{E}_{1,2}$. To do so we have two equations left, the integrated Euler equation (4.1) and its derivative, the force balance equation

$$0 = \{\partial_x u_t + \omega [(x - x_c) \partial_x u_y + u_y - y \partial_x u_x]\}_{|_{x=x_{1,2}}}, \quad (4.6)$$

where we have set $\partial_x h = 0$, which fixes the location of the stars' centers. We evaluate these equations each at two points — the centers of the stars as defined by the maximum density — and obtain four equations for four parameters to solve. The typical way is to solve the force balance equation (4.6) first, which yields ω and x_{cm} . The solving process is done with a root finding algorithm. We can then simply plug the solutions into the integrated Euler equation (4.1) evaluated at the centers to obtain the injection energy (which is constant throughout the star). Finally, we can evaluate (4.1) at arbitrary points and thus solve for h in order to update our fluid quantities. These updated values can be used to calculate new source terms via (3.6) and the next iteration step can start.

Note that during this whole process we have fixed the stars' centers $x_{1,2}$ and thus also the separation of the stars. Furthermore, the central density is a free parameter as well, which is fixed throughout the iteration, unless we want to fix the total rest-mass instead. We employ the latter especially to perform calculations of sequences. We provide another example of this scheme for equal mass stars in section 4.3.

4.2 Elliptic solver

Solving the constraint equations is the main duty of initial data computation in terms of time consumption. Nonlinear elliptic partial differential equations (PDE's) are not trivial to solve. Several different approaches have been developed in order to increase the efficiency of elliptic solvers and people still keep trying to improve the accuracy and runtime. A detailed analysis of various algorithms is given by Press et al. [2007]. While we employed a conjugate gradient method in our stand-alone implementation in Moldenhauer [2012], the nested boxes grid structure of BAM is perfectly suited for the use of multigrid methods. We do not want to go into much detail at this point and thus assume that the basic numerical concepts of finite differencing (or later for

SGRID pseudo-spectral representation) are known. However, since the solution of elliptic equations is crucial to the initial data construction, we want to summarize the methods of our choice.

4.2.1 Multigrid methods

One of the most famous introducing works on multigrid solvers was done by Brandt [1977] and thus multigrid methods are quite young in comparison to many other algorithms. The basic idea behind this concept is to use not one, but several grids with different resolutions. Common relaxation methods like Gauß-Seidel are applied on the coarsest grid, where they work comparably fast and then the solution is used to accelerate the computation on finer grids. It is thus possible to reach extremely low numbers of necessary operations. A differential equation, discretized on a grid with N points can be solved within $\mathcal{O}(N)$ operations (see Press et al. [2007]). For our nonlinear problems it is also a major advantage that multigrid methods are able to handle nonlinear equations without much further effort. From the range of different multigrid approaches (also see Briggs et al. [2000]) we choose the *full approximation storage multigrid algorithm* (or often just short FAS), which fits best to the intrinsic grid structure in BAM.

The general framework of such multigrid solvers can be described as follows. The PDE is assumed to be written as a nonlinear operator \mathcal{A} acting on the state vector \vec{x} , where we denote the grid spacing by h for the fine grid, yielding

$$\mathcal{A}_h(\vec{x}_h) = f_h, \quad (4.7)$$

and respectively the grid spacing $H = 2h$ for the coarse grid gives

$$\mathcal{A}_H(\vec{x}_H) = f_H. \quad (4.8)$$

If \vec{v} is an approximate solution to the exact solution \vec{x} , then the error is given by $\vec{e} = \vec{x} - \vec{v}$, while the residual is defined as

$$r = f - \mathcal{A}(v). \quad (4.9)$$

We have to be able to interpolate a solution from a fine grid to a coarser one and vice versa. This is done via *restriction* and *prolongation* operators \mathcal{R}_h^H and \mathcal{P}_H^h , where the subscripts and superscripts denote that \mathcal{R}_h^H restricts a solution from a grid with spacing h to a grid with spacing H and the other way round for the prolongation

operator. There are different possibilities to define these operators. A typical choice is given by a bilinear interpolation operator for prolongation and the adjoint operator for restriction.

Defining the residual on the fine grid according to (4.9) yields

$$r_h = \vec{f}_h - \mathcal{A}_h(\vec{v}_h) = \mathcal{A}_h(\vec{e}_h + \vec{v}_h) - \mathcal{A}_h(\vec{v}_h). \quad (4.10)$$

Similarly, we can consider the coarse grid, where (4.8) together with the definition of the residual yields

$$\begin{aligned} \mathcal{A}_H(\vec{x}_H) &= \mathcal{A}_H(\vec{v}_H) + \vec{r}_H \\ &= \mathcal{A}_H(\mathcal{R}_h^H \vec{v}_h) + \mathcal{R}_h^H \vec{r}_h \end{aligned} \quad (4.11)$$

and can be solved on the coarse grid (which is fast compared with solving on the fine grid) and results in an approximate solution \vec{v}_H . Thus we have a correction of the coarse grid by

$$\vec{e}_H = \vec{v}_H - \mathcal{R}_h^H \vec{v}_h \quad (4.12)$$

The important step is now to use the coarse grid correction to improve the approximate solution on the fine grid by prolongation

$$\begin{aligned} \vec{v}_h^{\text{new}} &= \vec{v}_h + \mathcal{P}_H^h \vec{e}_H \\ &= \vec{v}_h + \mathcal{P}_H^h \left(\vec{v}_H - \mathcal{R}_h^H \vec{v}_h \right). \end{aligned} \quad (4.13)$$

Iterating over this procedure yields further improvement of the approximate solution \vec{v} . This concept can be extended to several grids. This means that instead of solving (4.11), we can take it as the starting point of another multigrid level, where now $H = 2h$ is the fine grid in comparison to an even coarser grid with a grid spacing of $4h$. Only on the coarsest grid we really have to solve the system, for instance with a relaxation method like Gauß-Seidel. Finally, there are different schemes for the order of restriction and prolongation, which have a large influence on the performance and accuracy of the solver. In Fig. 4.1, we show the two schemes implemented in BAM, the V and W-cycle. The above discussion reveals that there are several settings that can be changed to adjust and tweak the multigrid solver such as restriction and prolongation operators, relaxation schemes and interpolation cycles. We tested different settings in order to find a stable and fast scheme, but a detailed analysis is not the goal of this thesis and can be found in the literature.

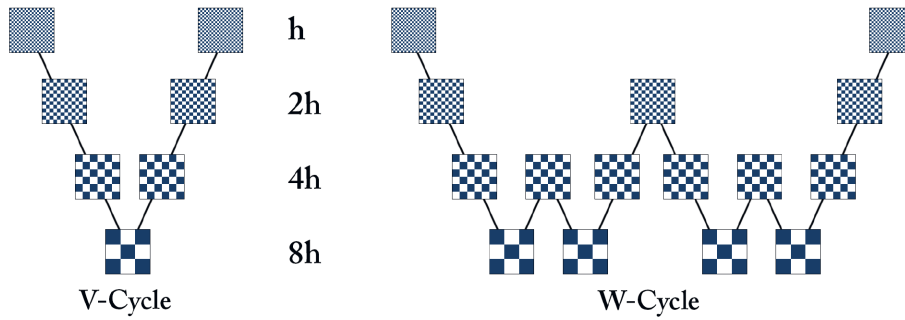


Figure 4.1: Shown are the two different types of cycles that are used in BAM for prolongation and restriction. Descending lines denote restriction from a fine to a coarser grid, while ascending lines denote prolongation from a coarse to a finer grid. A smoothing is applied in each step, but the full system of nonlinear equations has only to be solved on the coarsest grid.

4.3 BAM implementation

An early implementation of a previous version of the scheme outlined in 4.1 was presented within the master thesis [Moldenhauer, 2012] and first steps using the BAM code were already done. Unfortunately, this version of the scheme turned out to be insufficient and did not yield correct data. The new version was first implemented in the BAM code as described and tested in [Mol1]. A detailed description of BAM, in particular with respect to the neutron star treatment (and their evolutions) can be found in the work by Thierfelder et al. [2011] or in Brüggmann et al. [2008] for a discussion focused on black holes. The code uses second order-finite differences in a full approximation storage multigrid scheme. This multigrid solver, which is used to solve the elliptic equations as described in section 4.2, provides a nested boxes structure, where each refinement level doubles the resolution. The relaxation scheme that is employed on the coarsest level is a red-black Gauß-Seidel method [Press et al., 2007]. The code is fully parallelized with a hybrid OpenMP/MPI implementation and is able to use bitant or octant symmetry if desired. Due to the second order finite differencing operator, second order convergence is expected, but there is no obvious reason against the implementation of higher order multigrid methods to improve the convergence order. In fact, the OLLIPTIC code by Galaviz et al. [2010] would be available for an improvement to up to eighth-order stencils. However, we chose to increase the accuracy by implementing the scheme in the spectral SGRID code that is described in section 4.4.

Since the recipe as well as the multigrid elliptic solver have already been explained,

we want to provide more insight into the method by examining an example and discuss the different steps that are taken by BAM. For the sake of simplicity, we are looking at equal-mass stars. We specify a location of the stars' centers $\pm x_c$, a central density h_c and some parameters Γ and κ for the EoS. At first, the built-in TOV solver is called to compute a single spherical star, which is then placed at $\pm x_c$ and superimposed. If the stars are too close, the scheme requires a good initial guess and we have to add a boost (where we choose the parameter by hand) to the stars. For larger distances, the scheme works well with unboosted (head-on) data as an initial guess. After computing the source terms according to (3.6), we can solve the elliptic equations by feeding them to the multigrid solver, which provides us with updated values of ψ , α and β^i . We have to stress that we use Cartesian coordinates, which means that we do not have the benefits of any spatial compactification. We use a Robin boundary condition and provide the fall-off behavior of the quantities according to Duez et al. [2003] as

$$\alpha \sim 1 - r^{-1} \quad (4.14a)$$

$$\psi \sim 1 + r^{-1} \quad (4.14b)$$

$$\beta^x \sim \beta^y \sim r^{-2} \quad (4.14c)$$

$$\beta^z \sim r^{-4} \quad (4.14d)$$

Due to the mesh refinement, we are able to choose outer boundary locations far away at $t \sim 3000$, and hence yield good agreement for quasi-circular test cases with existing codes.

Since we chose equal mass stars, the center of mass x_{cm} has to be at $x = 0$, which allows us to algebraically solve the force-balance-equation (4.6) without calling a Newton-Raphson root finder. Therefore, we use (4.5) to construct the fluid velocity components and use second order finite differencing stencils to compute their derivatives. Plugging these values into the force-balance equation immediately yields the frequency ω . Using the constant three-velocity approximation, the Euler equation in BAM takes the form

$$\mathcal{E}_{1,2} = -hu^t \{-\alpha^2 + \psi^4[\beta^i \beta_i + v_{1,2} \beta^y - \omega y \beta^x + \omega(x - e x_{1,2})(\beta^y + v_{1,2})]\}. \quad (4.15)$$

We choose a fixed central density h_c thus we can evaluate (4.15) at the centers (if we chose to fix the mass, we would now have to compute the integrated mass) and obtain $\mathcal{E}_{1,2}$. This in turn allows us to evaluate (4.15) at an arbitrary location, since all variables are known and BAM computes an updated density profile h out of the elliptic

quantities ψ , α and β^i . Afterwards, the equation of state is used to compute the mass density and the pressure. At this point, the end of the iteration loop is reached. Next, we start again by computing the source terms and repeat the procedure until a fixed point is reached. Usually we end the iteration, if the overall change in the elliptic variables falls below a certain threshold. Note that we use a technique called *softening* to avoid overshooting the solution. More precisely, this means that instead of taking the full solution of the elliptic variables after a multigrid solve, we use a weighted average of old and new variables. Usually (if X denotes an elliptic variable), we choose

$$X = 0.25X_{\text{new}} + 0.75X_{\text{old}}. \quad (4.16)$$

This procedure is similar to the one used by Tichy [2012] and is crucial in order to achieve convergence.

4.4 Sgrid implementation

After discussing the BAM implementation, we want to give insight into the implementation of our scheme in the SGRID code developed by Tichy [2009b, 2012]. The BAM implementation was designed to be fast in terms of runtime and should serve as a testing environment for the scheme, which allowed us to vary all kinds of implementation details in order to find a stable and working algorithm. After successfully constructing initial data, we wanted to proceed by using a more specialized code to improve the accuracy of our computations. SGRID is a pseudo-spectral code and provides an advanced grid structure, which allows us to impose boundary conditions at the stellar surfaces. Thus the constant three-velocity approximation (3.15) can be dropped and we can solve the full velocity potential. We present that grid structure in the following and then briefly discuss the iteration procedure of SGRID, which is similar to the one used in BAM. Note that increased accuracy is not the only advantage of SGRID. It is also the first code that handles neutron stars with spins and recently, as we described in [Mol3], the EoS treatment has been generalized to handle piecewise polytropes in order to construct more realistic stars ¹.

¹For a detailed analysis of binary neutron star mergers with realistic equations of state for various mass ratios, and also a nice summary of single rotating stars we refer the reader to the PhD thesis of Tim Dietrich.

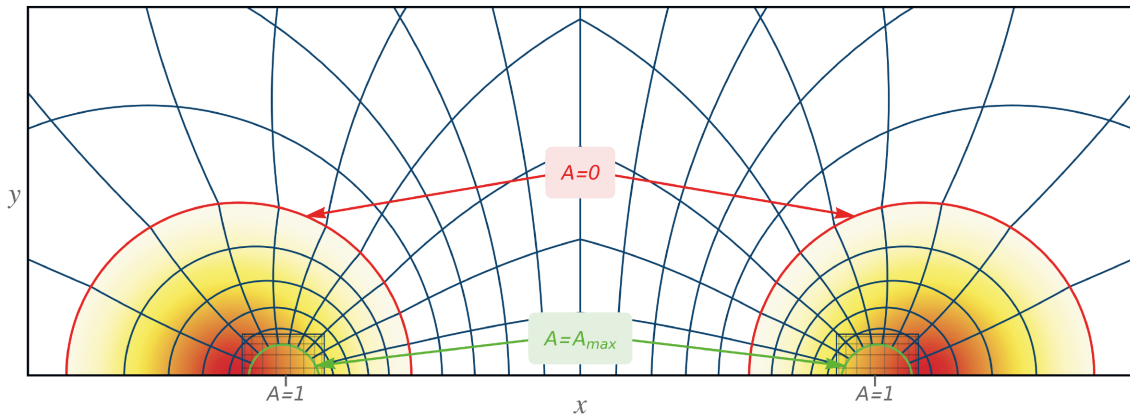


Figure 4.2: This Figure shows a $z = 0, y > 0$ cross section for the density profile of an equal mass configuration. The grid structure becomes evident by lines of constant A and B and also the Cartesian boxes with Chebychev grids are drawn. The lines of constant $A = 0$ and $A = A_{\max}$ are drawn in red and green respectively. The parameters used to construct this grid are (chosen according to the simulation to produce the density profile) $b = 16, \sigma_+ = -\sigma_- = 1.304$ and $A_{\max} = 0.5$. Adapted from [Mol3].

4.4.1 Grid configuration

Attempting to accurately solve neutron star initial data requires specialized grid setups. As we already discussed, we have to impose a boundary condition at the stellar surface and although the fluid quantities are smooth in the interior, they become non-differentiable at the surface. Thus, it would be best if the stellar surfaces were domain boundaries, however, the matter distribution and hence the star shapes change with each update of the fluid density. To solve this issue, Tichy [2009b] introduced special coordinates, based on the coordinates by Ansorg [2007] and divides the domain into 6 separate parts. We have one domain for the interior of each star and another two domains, which describe the outer region; again one domain for each star. Finally, the interior domains possess a coordinate singularity, which has to be covered by a Cartesian box, so that we obtain a total of six domains. Figure 4.2 shows the computational domains and the grid structure, which we are about to introduce.

The chosen coordinates provide a compactified domain and include spatial infinity,

which makes it easy to impose outer boundary conditions

$$\lim_{r \rightarrow \infty} \psi = 1, \quad (4.17a)$$

$$\lim_{r \rightarrow \infty} B^i = 0, \quad (4.17b)$$

$$\lim_{r \rightarrow \infty} \alpha \psi = 1. \quad (4.17c)$$

Denoting the new coordinates by $X \in [0, 1]$, $R \in [0, \sqrt{1 - X^2}]$ and $\varphi \in [0, 2\pi)$, we can give the relation to Cartesian coordinates by (cf. Tichy [2009b])

$$x = \frac{b}{2} \left[\frac{1}{(X^2 + R^2)^2} + 1 \right] (X^2 - R^2), \quad (4.18a)$$

$$y = b \left[\frac{1}{(X^2 + R^2)^2} - 1 \right] XR \cos(\varphi), \quad (4.18b)$$

$$z = b \left[\frac{1}{(X^2 + R^2)^2} + 1 \right] XR \sin(\varphi). \quad (4.18c)$$

Here, b is a parameter to specify the distance of the stars. Another transformation is applied to obtain coordinates A, B, φ , which take into account the different computational domains. The two exterior domains include spatial infinity $(A, B) = (1, 0)$ and use

$$X = (1 - A) [\operatorname{Re}(C_{\pm}(B, \varphi)) - B \operatorname{Re}(C_{\pm}(1, \varphi))] + B \cos \left(\frac{A\pi}{4} + (1 - A) \arg(C_{\pm}(1, \varphi)) \right), \quad (4.19a)$$

$$R = (1 - A) [\operatorname{Im}(C_{\pm}(B, \varphi)) - B \operatorname{Im}(C_{\pm}(1, \varphi))] + B \sin \left(\frac{A\pi}{4} + (1 - A) \arg(C_{\pm}(1, \varphi)) \right). \quad (4.19b)$$

The stellar surfaces are given by the inner domain boundary $A = 0$, where we employ a strictly positive function C_+ and a strictly negative function C_- to describe the shape of the surface

$$C_{\pm}(B, \varphi) = \sqrt{\tanh \left(\frac{\sigma_{\pm}(B, \varphi) + i\pi B}{4} \right)}. \quad (4.20)$$

Here, σ_{\pm} gives the relation of the star's surface to Cartesian coordinates. While $A = 0$ always describes the surface, σ_{\pm} determines the (x, y, z) location, for instance a spherical star is given by constant σ_{\pm} .

The coordinate transformations are different for the inner region of the stars and can

be expressed by

$$\begin{aligned} X &= (1 - A) [\operatorname{Re}(C_{\pm}(B, \varphi)) - B \operatorname{Re}(C_{\pm}(1, \varphi))] \\ &\quad + B \cos(D_{\pm}) + \delta_+(1 - B)A, \end{aligned} \quad (4.21a)$$

$$\begin{aligned} R &= (1 - A) [\operatorname{Im}(C_{\pm}(B, \varphi)) - B \operatorname{Im}(C_{\pm}(1, \varphi))] \\ &\quad + B \sin(D_{\pm}) + \delta_-(1 - B)A, \end{aligned} \quad (4.21b)$$

where

$$D_{\pm} := (1 - A) \arg(C_{\pm}(1, \varphi)) + \delta_{\pm} \frac{\pi}{2} A \quad (4.22)$$

and the abbreviations $\delta_+ = 1$ for the star located at $x > 0$ and $\delta_+ = 0$ for $x < 0$, and the other way round for δ_- .

As indicated before, a Cartesian grid is employed at the stars' centers. Looking at (4.18a) and (4.21a) one can see that the coordinates are indeed singular at the center of the star $A = 1$. Therefore, A goes to a maximum value $A_{\max} < 1$ (often ~ 0.8 and depending on the choice, the Cartesian box will be larger or smaller and the grid points will be more or less clustered) and the Cartesian boxes are given with grid points

$$x^i_k = \frac{x^i_{\min} - x^i_{\max}}{2} \cos\left(\frac{k\pi}{n^i - 1}\right) + \frac{x^i_{\min} + x^i_{\max}}{2}, \quad (4.23)$$

where $x^i = (x, y, z)$, with $0 \leq k < n_{\text{Cart}}$. For the A, B directions Chebychev expansions are employed, while we use Fourier expansions in ϕ direction. The collocation points are given by

$$A_i = \frac{A_{\max}}{2} \left[1 - \cos\left(\frac{\pi i}{n_A - 1}\right) \right], \quad (4.24a)$$

$$B_j = \frac{1}{2} \left[1 - \cos\left(\frac{\pi j}{n_B - 1}\right) \right], \quad (4.24b)$$

$$\varphi_k = \frac{2\pi k}{n_{\varphi}}, \quad (4.24c)$$

where $0 \leq i < n_A$, $0 \leq j < n_B$ and $0 \leq k < n_{\varphi}$. Typical setups we are running make use of 20 to 28 points in A and B direction, while 8 points in φ direction are sufficient. In the Cartesian box we employ $n_x = n_y = n_z = n_{\text{Cart}} = 16, \dots, 24$ points. Note that piecewise polytropic setups naturally require more points, since the different pieces may be not resolved at the lower end of these specifications.

The elliptic variables are written altogether into a state vector and the XCTS equations (3.5) are imposed at each grid point. The nonlinear system is solved within

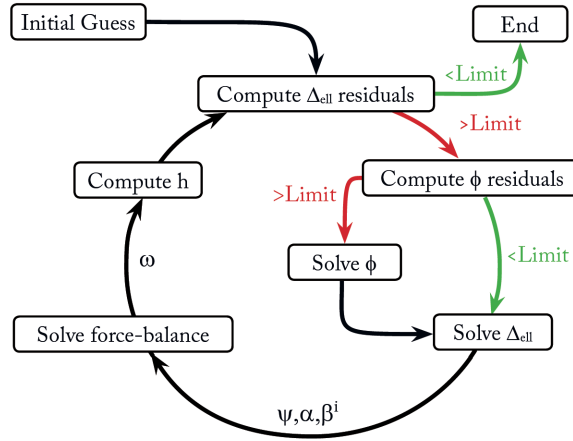


Figure 4.3: Schematic representation of the iteration scheme as outlined in the text. Δ_{ell} denotes the set of elliptic equations. Plot adapted from [Mol3].

a Newton-Raphson iteration, while the linearized equations can be solve via matrix inversion, where the UMFPACK sparse matrix solvers are used [Davis, a,b] or the references within the original description [Tichy, 2009b]).

4.4.2 Iteration

The iteration scheme that is used in SGRID is similar to the one used in BAM, but with the additional complication of solving the elliptic equation for the velocity potential. Tichy [2012] describes the following iterative procedure (see also Figure 4.3) to construct initial data and our additions to the SGRID code do not change this overall behavior.

(i) Similar to the initialization of the BAM implementation, we either start with solving the TOV equations and superimposing them or by using a previously constructed solution. The latter will become handy when we construct low eccentric data in Sec. 5.3. The orbital angular velocity is computed with the help of post-Newtonian theory and the velocity potential is set to $\phi = \Omega(x_{c1,2} - x_{\text{cm}})y$, which corresponds to a spatially constant velocity field.

(ii) Next, we compute the residuals of all elliptic equations and leave the iteration loop if the combined residual falls below a threshold.

(iii) The third step consists of computing the residual of (3.14) and see if it exceeds a tenth of the previously computed combined residual of the elliptic equations. If so, we solve the elliptic equation for ϕ to update the velocity potential with a softening $\phi_{\text{new}} = 0.2\phi + 0.8\phi_{\text{old}}$.

(iv) In this step the main solve of the five elliptic equations is performed and again

softening is applied $\Delta_{\text{ell}}^{\text{new}} = 0.4\Delta_{\text{ell}} + 0.6\Delta_{\text{ell}}^{\text{old}}$, where Δ_{ell} stands for the elliptic variables ψ, α, B^i .

(v) The maximum of h along the x -axis is searched in order to find the positions of the stars' centers, $x_{c_{1,2}}$. Then Ω and x_{cm} are computed through the force balance equation (4.6).

(vi) One of the last steps is to compute h and $\mathcal{E}_{1,2}$ such that the baryonic mass of each star remains constant. Finally, σ_{\pm} is updated to take into account the changes in the shape of the stars' surfaces and adjust the domain boundaries with respect to that. In order to improve the overall stability, it might be necessary to filter out high frequencies in σ_{\pm} and impose $\partial_B \sigma_{\pm}(B, \varphi)|_{B=0,1} = 0$ to keep the stars on the x -axis.

(vii) We go back to step (ii).

Neutron star initial data

It is now time to use the presented scheme for initial data construction. Therefore, we start with consistency checks in the quasicircular test case, where we set $e = v_r = 0$. We do not have to check the constructed SGRID data in the circular case, since these data have been examined before [Tichy, 2009b] (of course, we have to ensure that the data is still the same, which has to be the case if the implementation was done correctly). Nevertheless, we verify that the BAM implementation constructs reasonable initial data in this limit, based on our investigations published in [Mol1]. Afterwards we examine eccentric initial data and show the advantages of the scheme compared to previous initial data sets. We also present the improvements we recently achieved in [Mol3] through the use of surface-fitted coordinates. Finally, we are considering low eccentric initial data and use our scheme to compute orbits with an inward velocity to improve the noise in the extracted gravitational waves due to the residual eccentricity. Note that all evolutions are done with BAM and that the SGRID data has to be interpolated onto the BAM grid before evolving it, while the multigrid data can be used directly, since it uses the same grid structure (compare Fig. 5.1).

5.1 Quasicircular orbits

SGRID has been compared against other codes, such as the Lorene code from the Meudon group as it is described e.g. by Taniguchi and Gourgoulhon [2002] in the limit of irrotational stars on circular orbits. These studies show good agreement and we thus use SGRID as a reference for the BAM implementation. We provide a table with different datasets in Table 5.1, where we list the basic parameter choices for several setups for quasicircular data and also eccentric data that is used later on.

First, we check the convergence of the code in order to provide a solid basis for further discussions. We use the setup *mgQC* and compare the constraints at three different resolutions in Fig. 5.2, where the finest grid (the innermost of six levels) has a grid

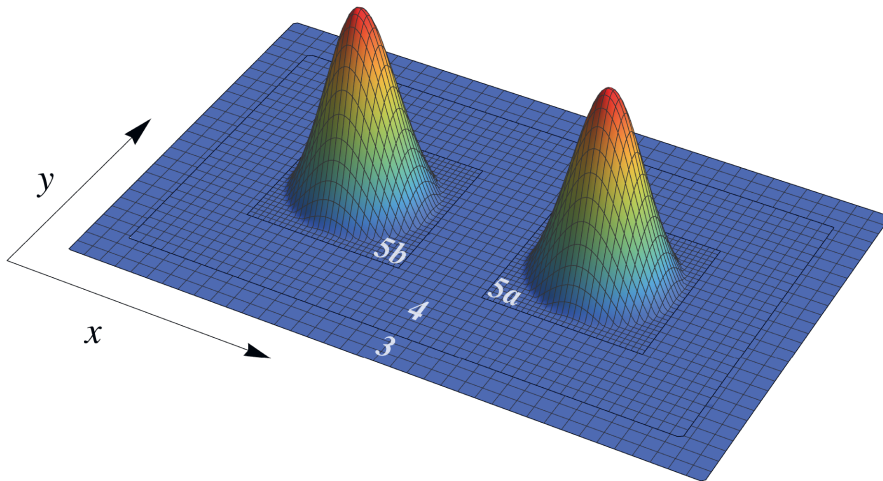


Figure 5.1: Example of a BAM setup corresponding to $mgQC$ from Table 5.1. The multigrid solver of BAM uses the same grid setup as the evolutions. Shown is the density profile in the xy -plane. One can see the innermost levels $l = 5a, b$, $l = 4$ and partially $l = 3$. Levels $l = 2, 1, 0$ are not depicted. Instead of the full grid, only every fourth grid point is shown for better visibility.

spacing of $h = 0.09375$, which corresponds to the range of resolutions we target for production runs. The boundary is chosen to be at $x = y = z \sim \pm 500$ and is fixed for the convergence checks. Although this might be too close for production runs, we tried to keep the computational efforts low, hence exceedingly accurate boundaries are not needed for convergence analysis. In fact, unless we want to extract gravitational waves, the boundary distance is large enough in order to obtain accurate results from the Robin boundary conditions for the elliptic variables. Later we add additional refinement levels to push the outer boundary further out than we have done now for our five refinement levels, which is especially necessary for gravitational wave extraction. The results clearly show convergence of second order as it is expected for the multigrid solver. The left panel of Fig. 5.2 shows the Hamiltonian constraint \mathcal{H} , while the right panel shows the y -component of the momentum constraint \mathcal{D}^y . These quantities were chosen, since they yield the largest constraint violations (\mathcal{D}^x and \mathcal{D}^z are much smaller, because the stars are initially moving in $\pm y$ -direction.), but in principle every other elliptic or constraint monitoring quantity we tested shows the same behavior. It is noteworthy that the constraint violations are computed with second-order finite differencing as well and thus corresponds to the multigrid order. Without surface-fitting coordinates it is hard to remove numerical artifacts at the surface of the stars. We cut off those features to show the details in the center of the stars, but we show them later in Fig. 5.5 and we postpone the discussion of the

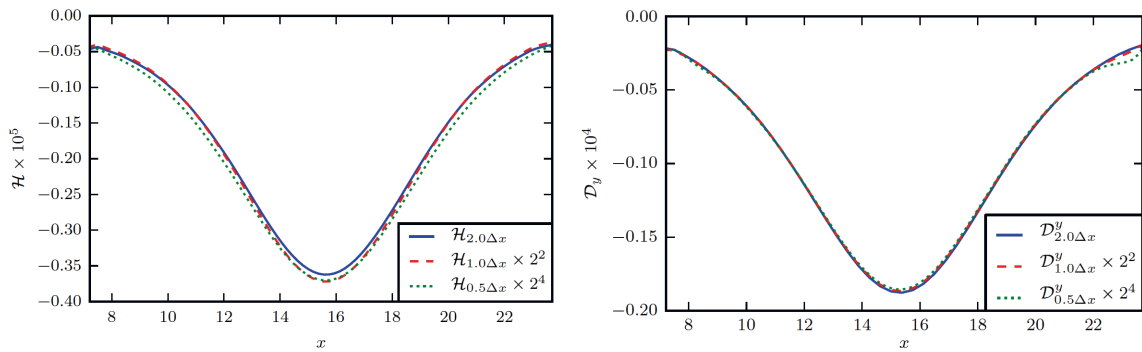


Figure 5.2: Shown is the convergence of the multigrid implementation with the help of the Hamiltonian constraint (left) and the y -component of the momentum constraint (right, adopted from [Mol1]). Each constraint is plotted along the x -axis passing through the stars' centers. We show the interior of one star for three different resolutions, the standard one with a grid spacing $\Delta x = 0.1875$ and double $2\Delta x$ respectively half $0.5\Delta x$ the resolution for the others. The medium and the fine grid solution are scaled with factors of 2^2 and 2^4 in order to match the coarse grid solution. Note that we are focusing on the strong-field interior of the star on purpose in these plots. Convergence (and the constraint violations) is worse at the surface and produces spikes due to inaccuracies. These features are the same in the eccentric case and will therefore be discussed later in Sec. 5.2.

spikes to the corresponding section.

In Sec. 3.2.2 we already showed a preview of some evolutions to justify the constant three-velocity approximation and we want to add another point here. But before, we have to give some details about the evolution setups. The setups we employ are similar to the ones used by Bernuzzi et al. [2012b] with some modifications. We use second-order spatial finite differencing for the geometry, consistent with the order of the multigrid algorithm, and fourth-order Runge-Kutta integration in time. Additionally, we employ fourth-order Kreiss-Oliger dissipation as it is appropriate for second-order spatial finite differencing. A fifth-order weighted-essentially-non-oscillatory WENOZ scheme [Bernuzzi et al., 2012a] is employed for the evolution of the fluid quantities as well as a LLF flux scheme. Note that the evolutions of the multigrid solver are designed to run with good performance, as we are later going to use them for quick parameter estimates, so we can construct SGRID data with the desired properties (cf. the run times mentioned in Sec. 5.2). For high accuracy runs and most SGRID evolutions we use slightly different setups.

Fig. 5.3 presents another justification for the constant three-velocity (CTV) approxi-

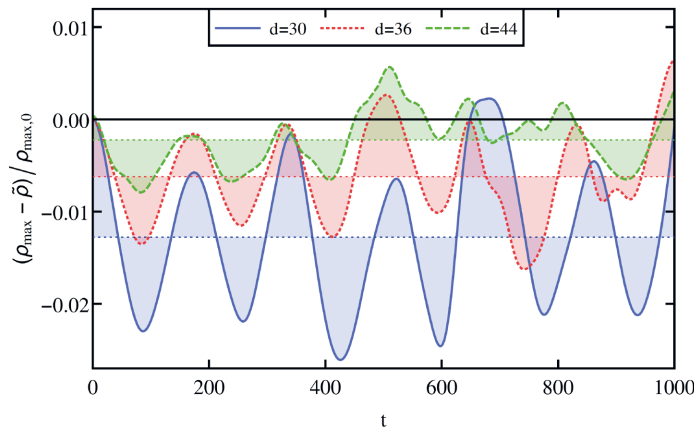


Figure 5.3: Comparison of the constant three-velocity approximation. Shown are the central density oscillations $\rho_{\max}(t)/\rho_{\max,0}$ normalized by the initial central density and shifted by the corresponding central density of the run without approximation $\tilde{\rho}(t)$. These deviations caused by the approximation are shown for different initial separations d and are clearly decreasing for higher initial distances. The horizontal lines, which the curves are oscillating around, represent the average deviation.

mation by looking at the oscillations of the central rest-mass density $\rho_{\max}(t)$. Instead of looking at the density directly, we look at the difference of the density oscillations with and without the CTV approximation (here we denote the latter by a tilde) and normalize it by the initial value $[\rho_{\max}(t) - \tilde{\rho}(t)]/\rho_{\max,0}$. Originally, the density is more noisy, which required us to use simple low-pass filters in order to make a clean analysis. Then we compare three different initial separations $d = 30, 36$ and 44 and find that the average deviation from the run, where we perform a full solve for the velocity potential indeed decreases with increasing separation. Together with the considerations in Fig. 3.2, we can confirm that the CTV approximation is especially useful for runs with large initial separations, as we deal with for highly eccentric runs. For small separations, those eccentric setups would just immediately merge, similar to head-on collisions.

The last check we perform on initial data for quasicircular binaries is a further investigation of the central density oscillations. So far, we just considered the oscillations we obtain with the CTV approximation. Now, we want to have a look at these spurious oscillations for different kinds of initial data and demonstrate how the CTV approximation is indeed a huge improvement over superimposed TOV stars, which were used by Gold et al. [2012]. Fig. 5.4 shows a range of different initial data types and confirms that inconsistencies of the data with the hydrodynamic properties of the system lead to unphysical oscillations. The worst result — in terms of the oscillation

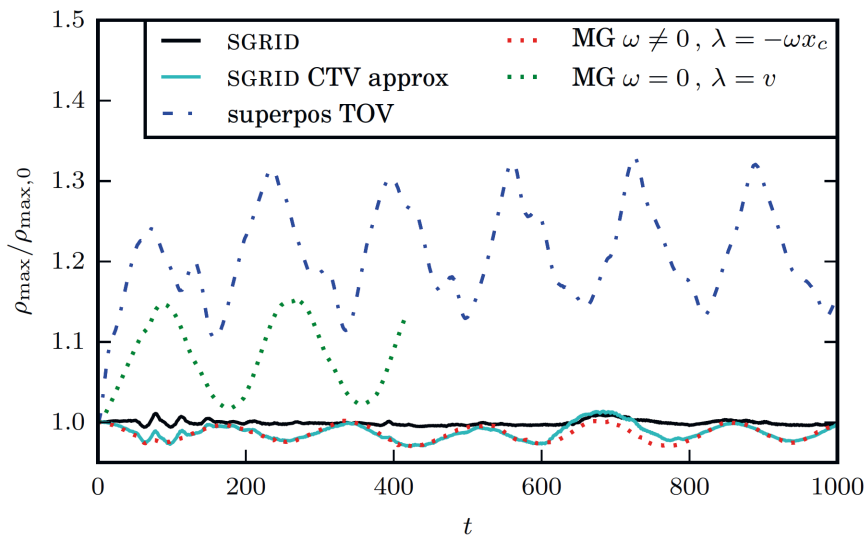


Figure 5.4: Comparison of the stellar density oscillations over time, where ρ_{\max} denotes the central density and is normalized by the maximum density at $t = 0$, denoted by $\rho_{\max, 0}$. We show evolutions of various initial data types, where we distinguish between SGRID initial data (solid), multigrid initial data (dotted) and superimposed, boosted TOV stars (dot-dashed). We further distinguish between the SGRID setup with (cyan) and without (black) constant-three velocity approximation. Two different multigrid setups show the influence of the stationarity frame, i.e. stationarity in a rotating frame (red) and in a linearly comoving frame (green). While the improvement of the spurious oscillations is not large for the latter, the effect of the rotating frame is clearly visible (red and cyan) and the remaining oscillations vanish if we solve for the full velocity potential (black).

amplitude — is obtained when we take superimposed TOV stars. We tried to find a boost parameter that results in velocities similar to those we obtained through our schemes and thus approximating circular data. The remaining eccentricity can be further reduced iteratively via bisection, but this would not even be necessary for the kind of comparison we are doing, since the central density oscillations are insensitive. The resulting oscillations are roughly 20%. If we now assume stationarity in a linearly comoving frame, as it is the case for boosted TOV stars, but solve the constraint and the hydrodynamic equations, the spurious oscillations are not significantly reduced (note that these configurations are also not easily converging, since they require strong softening and careful treatment of the iteration order and parameters. A more detailed view on this can be found in [Mol1]). On the other hand, Tsatsin and Marronetti [2013] were able to reduce the oscillations without solving these equations, by “simply” changing the shape of the stars. They found a way to reduce the oscillations in non-constraint solved data by tuning the profile of the

matter density and the velocities. However, this kind of fine tuning is undesirable and violating the constraints is not satisfying from a physical point of view. Fig. 5.4 also shows data which assumes stationarity in a corotating frame, which is consistent with the hydrodynamic properties of the system (see the discussion in Sec. 5.2.1). If we use the CTV approximation in SGRID (recall that we always use it in the multigrid solver, due to the Cartesian coordinates) and compare to the multigrid solution, then we see almost identical spurious oscillations, which are improved by an order of magnitude with respect to the superimposed data. Finally, we consider SGRID data, where we solve for the full velocity potential and see that the spurious oscillations are basically removed (apart from initial perturbations that are present in all datasets).

Another possible way to verify the consistency of the data and check the quality is to look at constant rest-mass sequences. These are provided in Sec. 5.2.2 for eccentric systems, where we also include the limit of circular binaries.

5.2 Eccentric orbits

After assuring that the data we produce with our code are giving reasonable results in the limit of circular orbits, we can proceed to more interesting cases that have not been treated before. We test our scheme for large eccentricities and start by investigating the convergence behavior, similar to what we did for circular orbits. Next, we produce highly eccentric binaries and discuss their properties and compare the features to previous studies from Gold et al. [2012] with inconsistent initial data. Furthermore, we are trying to give some estimates of the reasonability of our data with respect to post-Newtonian estimates. During all these examinations we are considering data computed with SGRID as well as with BAM's multigrid solver.

Before discussing any details we want to have a brief look at the runtimes of the two different implementations. As we mentioned many times before, due to spectral accuracy and a complicated surface-fitting grid structure, SGRID is more accurate as the multigrid solver. However the major advantage of the multigrid method is its computational speed. Due to the use of MPI, the BAM code scales well for large numbers of cores (we tested up to 512 cores), whereas SGRID's pure OpenMP parallelization usually does not allow more than twelve cores. Additionally, the computation in SGRID is more expensive because of the different computational domains. Computing data with BAM with 258^3 points — which is higher than most production runs — takes 0.9 hours on 256 cores on the JUROPA cluster (130^3 points can be computed on 96 cores in 0.6 hours), while typical SGRID computations need roughly two weeks (with

Table 5.1: The most relevant parameters for various initial data sets used for comparisons in the circular limit and for eccentric systems. We label the data sets by their most notable properties, beginning with *mg* or *sg*, denoting whether the data was computed with BAM’s multigrad or SGRID. Usually, we give further give the corresponding eccentricity parameter followed by certain extensions denoting, denoting high resolution (*h*) or other special assumptions. The setups used for sequences are included and labeled by *Seq* to distinguish from single circular or eccentric runs (*QC* or *Ecc*). In the table, the equation of state is given as EoS and we specify if we use the CTV approximation of solve for the velocity potential. We usually assume stationarity in a rotating (*rot*) frame ($\lambda = -\omega x_c$), but sometimes stationarity in a comoving frame (*com*) is employed. In the remaining columns, $m_{1,2}$ denotes the baryonic mass of each star, d_{coord} denotes the initial coordinate separation of the stars’ centers and e is the eccentricity parameter set in the initial data. Furthermore, κ is the scale parameter in the polytropic EOS, $(\Delta x)_{\text{min}}$ denotes the finest grid spacing, and n denotes the number of points in each dimension on each level, where we use l_{max} refinement levels, from which all levels $l > l_{\text{inv}}$ are moving. Note that we give the setups of BAM evolutions. For SGRID sequences we specify the relevant parameters instead.

Name	EoS	Assumption	$m_{1,2}$	d_{coord}	e	κ	$(\Delta x)_{\text{min}}$	points	l_{max}	l_{inv}
mgQC	$\Gamma 2$	CTV,rot	1.620	31.3	0	123.65	0.09375, 0.1875,	194, 98,	5	1
							0.375	50		
mgQCcom	$\Gamma 2$	CTV,com	1.620	31.3	0	123.65	0.1875	98	5	1
mgSeq{ <i>e</i> }	$\Gamma 2$	CTV,rot	1.625	[30.64, ..., 51.44]	0, 0.2, 0.5, 0.9	123.65	0.156	146	8	–
mgEcc{ <i>e</i> }	$\Gamma 2$	CTV,rot	1.504	80.0	0.45, 0.5, 0.6, 0.73, 0.8, 0.915, 0.96	100	0.25	130	6	3
mgEcc0.915h	$\Gamma 2$	CTV,rot	1.504	80.0	0.915	100	0.125	258	6	3
sgQC	$\Gamma 2$	full,rot	1.620	31.3	0	123.65	0.1875	98	5	1
sgQCctv	$\Gamma 2$	CTV,rot	1.620	31.3	0	123.65	0.1875	98	5	1
sgSeq{ <i>e</i> }	$\Gamma 2$	full,rot	1.620	[30.64, ..., 102]	0, 0.1, 0.2, 0.4, 0.5	123.65	$n_A = n_B = 24$, $n_\phi = 8$ and $n_{\text{cart}} = 20$			
sgEcc0.45SLy	SLy	full,rot	1.504	79.0	0.45	–	0.25	130	6	2
sgEcc{ <i>e</i> }H4	H4	full,rot	1.468	37.2	0, 0.3	–	$n_A = n_B = 8, \dots, 30$, $n_{\text{cart}} = n_A - 4$			
sgEcc{ <i>e</i> } $\Gamma 2$	$\Gamma 2$	full,rot	1.490	37.2	0, 0.3	–	$n_A = n_B = 8, \dots, 30$, $n_{\text{cart}} = n_A - 4$			

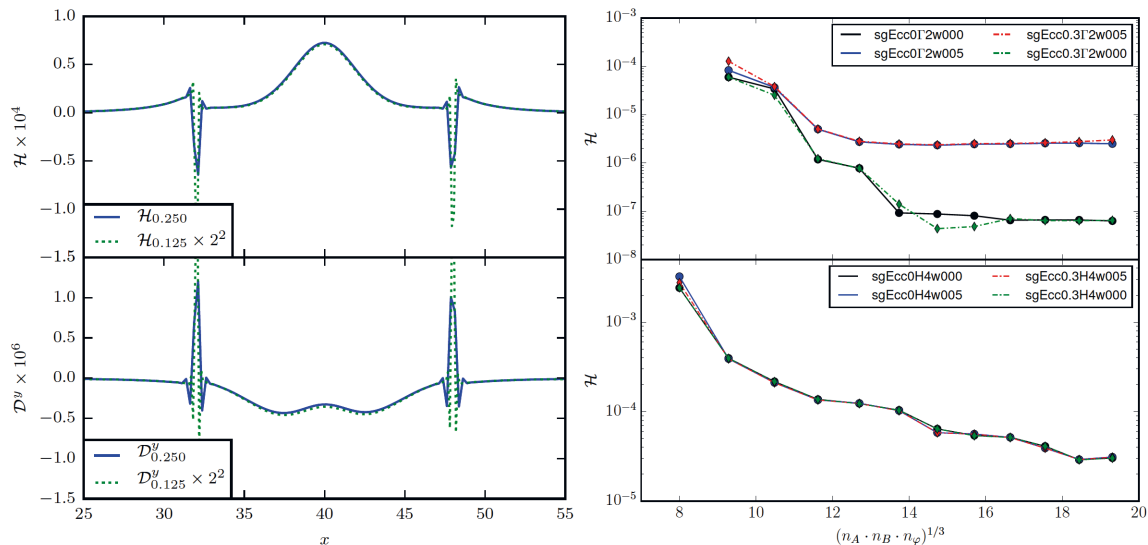


Figure 5.5: Convergence of the two implementations are shown. Left: The Hamiltonian and y -component of the momentum constraint for an eccentric configuration ($mgEcc0.915$) computed with BAM. The results are plotted along the x axis, which connects the two star centers and one star is shown at the finest grid box, including the surface, where spikes are occurring. We use two different resolutions and scale the results with the appropriate factor of second order convergence. Plot adopted from [Mol1]. Right: Convergence of SGRID shown with the help of the Hamiltonian constraint \mathcal{H} inside the two stars in the regions $A \in [0, A_{\max}]$, which includes the surface. We compare different setups $sgEcc0\Gamma_2$ and $sgEcc0.3\Gamma_2$, and $sgEcc0H_4$ and $sgEcc0.3H_4$, where $w000/5$ denotes the spin. The top panel shows simple polytropic Γ_2 EoS and the lower panel shows more complicated piecewise polytropic H4 EoS. In both cases we give the convergence for eccentric, non eccentric, eccentric spinning and non spinning setups. We have fixed $n_\phi = 8$ and use $n_A = n_B, n_{\text{Cart}} = n_A - 4$. Plot adapted from [Mol3].

$n_A = n_B = 26, n_{\text{cart}} = 22$) on twelve cores to finish. These different speeds are a nice illustration of the benefit of the simplicity of this implementation. In particular, one should have in mind that the time to compute initial data with BAM vanishes in comparison with typical evolution times, which are larger by a factor of ~ 50 for short runs with direct merger. In case of (several) encounters or inspiral, the evolution times drastically increase.

5.2.1 Convergence

Again, we start by discussing the converge properties of our implementations. Considering the left part of Fig. 5.5, we compare different initial data sets, which have

been computed with the BAM multigrid. The following grid setup is employed and can be used for production quality runs: We use 6 refinement levels and an outer boundary at $x = y = z \sim \pm 10^3$. The resolutions we compare employ 130^3 points with a spacing of $h = 0.25$ at the finest level and 258^3 points with a spacing of $h = 0.125$ respectively. Similar to the discussion in Sec. 5.1, we look at the constraint violations along the x -axis and we can see clear second order convergence in most parts of the plot, as it is expected. One can see some exceptions at the surface of the star, where the constraint violations are forming spikes. However, this can also be expected, since the density of an Γ_2 polytropic star is not differentiable at the surface. Moreover, we use sixth order finite differencing during the evolution of the metric variables in order to increase accuracy, i.e. reducing the constraint violations. This implies that we also use sixth order finite differencing to compute the constraints of our data, which itself is computed with second order stencils, and thus amplify the spiky features at the surface. At least for the Hamiltonian constraint, these artifacts are much smaller if we use second order finite differencing to compute the constraints. Furthermore, the usage of higher order stencils also leads to a qualitative change in the shape of the momentum constraint if we compare Figs. 5.5 and 5.2. This is not unexpected, since the remainders from second-order finite differencing are relatively large here.

We are pointing out that the difference in terms of convergence properties between eccentric and non-eccentric data is extremely small. Hence, the $e = 0.915$ case represents all eccentric runs, since we could not see any qualitative differences between high and low (or even zero) eccentricity.

Let us now consider the right panels of Fig. 5.5, where we show convergence for SGRID. First, in the upper plot we show simple polytropic stars as we also computed with BAM. Since SGRID is a spectral code, we show a different type of convergence — namely, the falloff of the overall constraint (here e.g. the Hamiltonian constraint. We could also show the momentum constraint, which looks similar but an order of magnitude smaller) with an increased number of points. We investigated spinning and non-spinning [$\omega_A^i = \omega_B^i = (0.005, 0.005, 0.005)$, resp. $\omega_A^i = \omega_B^i = (0, 0, 0)$] with and without eccentricity. We can clearly see that spinning stars are harder to solve and show larger violations as non-spinning setups. On the other hand, we can also see that adding eccentricity does not influence the convergence properties of SGRID. The lower right panel of the figure shows more complicated piecewise polytropic equations of state, as represented by the H4 EoS. Here we see again that adding eccentricity has a negligible effect on the convergence properties. However, as we discuss

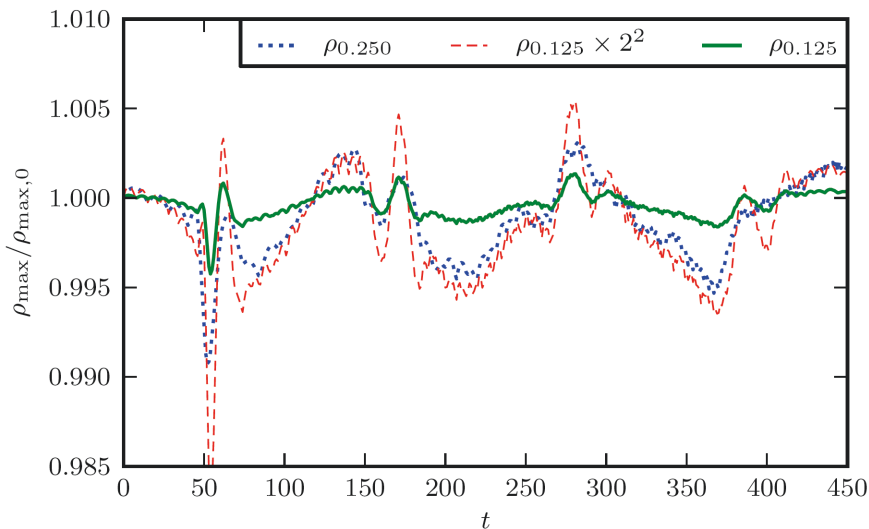


Figure 5.6: Convergence of the spurious density oscillations from data computed with BAM. The central density is shown for two different resolutions (datasets *MGe09* and *MGe09high*), which has an eccentricity $e = 0.915$. We show for the two resolutions (blue dotted and solid green) and also the rescaled high resolution results (red dashed), where we did not rescale the whole result, but only the oscillations $\Delta\rho_{\max}$ with a scaling factor 2^2 for second order convergence. Plot adopted from [Mol1].

in more detail in [Mol3], we can see that the overall convergence is worse for these EoSs, since the solution is only C^1 at the interfaces between different pieces and thus one does no longer obtain exponential convergence.

As we showed for circular orbits in Sec. 5.1, the spurious density oscillations are greatly improved for our data computed with BAM and almost vanishing if we employ SGRID and its surface fitting coordinates. This behavior does not change for eccentric orbits and the density oscillations look almost identical. However, we can show another nice convergence property if we again consider the BAM implementation from this section’s beginning. Fig. 5.6 monitors the central density for the *MGe09(high)* setup. We see a clear improvement in the oscillations when doubling the resolution and the convergence can be estimated by multiplying the oscillations $\Delta\rho_{\max} = \rho_{\max} - \rho_{\max,0}$ by the appropriate scaling factor, i.e., considering $4\Delta\rho_{\max} + \rho_{\max,0}$ for second-order convergence with a factor of 2 difference in the grid spacing. Although we can observe some small superimposed features around, e.g., $t = 50$ or $t = 180$, it is safe to say that the oscillations are decreasing with increasing resolution with almost second-order convergence. Due to spatial conformal flatness and the fact that we neglect radial radiation reaction velocity components, we do not expect the oscillations to completely converge away in the continuum limit. However, based on the results

shown in Fig. 5.6 and our results with SGRID, we expect that these oscillations would be at the same level as we see for SGRID.

5.2.2 Eccentric sequences and post-Newtonian comparisons

The convergence tests strengthened the trust in the numerics of our implementations. Now we want to check our results in a more physically motivated way by the means of sequences. This means, we compute a series of equal mass initial data sets with fixed baryonic mass $m_b = 1.625$ and vary the initial separation. We additionally vary the eccentricity of such sequences. To the best of our knowledge we have thus been the first to construct eccentric sequences in [Mol1]. Our results are shown in the following. In our particular setup, an isolated star with the same baryonic mass would yield a gravitational mass $M_i = 1.5149$. Using this mass, we can define a quantity typically used in sequences — the binding energy $E_b = M_{\text{ADM}} - M$. Here $M = 2M_i$ and M_{ADM} denotes the Arnowitt-Deser-Misner (ADM) mass, an asymptotic quantity that gives a measure of the total mass of the spacetime.

We take a short detour to discuss the measurement of the ADM mass, since there have been proposed several different ways. For example Ó Murchadha and York [1974] show how to define M_{ADM} via an integral at spatial infinity, requiring extrapolation in codes such as BAM, which do not support compactified coordinates. A realization of this idea can be found e.g. in the work of Brüggmann et al. [2008]. However, we noticed that the resolutions we use at the outer levels is not fine enough to give good results. Therefore we extract the ADM mass at a single radius which is sufficiently large, but not too close to the outer boundary where the resolution drops. Equation (16) of Ó Murchadha and York [1974] provides a useful formula to compute the ADM mass in spatial conformal flatness. As explained in that work, this simplified expression of the ADM mass can be evaluated in any region that satisfies the Laplace equation. Looking at equation (3.5a) in our case, it is evident that Laplace’s equation is approximately fulfilled, since the matter source vanishes outside of the star and $A_{ij}A^{ij}$ goes like the shift squared, which falls off to zero at infinity. Thus we can extract the ADM mass more easily and accurately. Actual experiments with SGRID data yielded a change in the mass of less than 0.01% when we changed the extraction radius of the simplified computation from $r = 150$ to $r = 500$, while the same change amounts to a deviation in mass of $\sim 4\%$ for the original ADM mass computation. The standard measure for the ADM angular momentum is sufficiently accurate for finite radii, so that we do not use extrapolation here, as well. We find a deviation caused by the change of the extraction radius of roughly 0.05%.

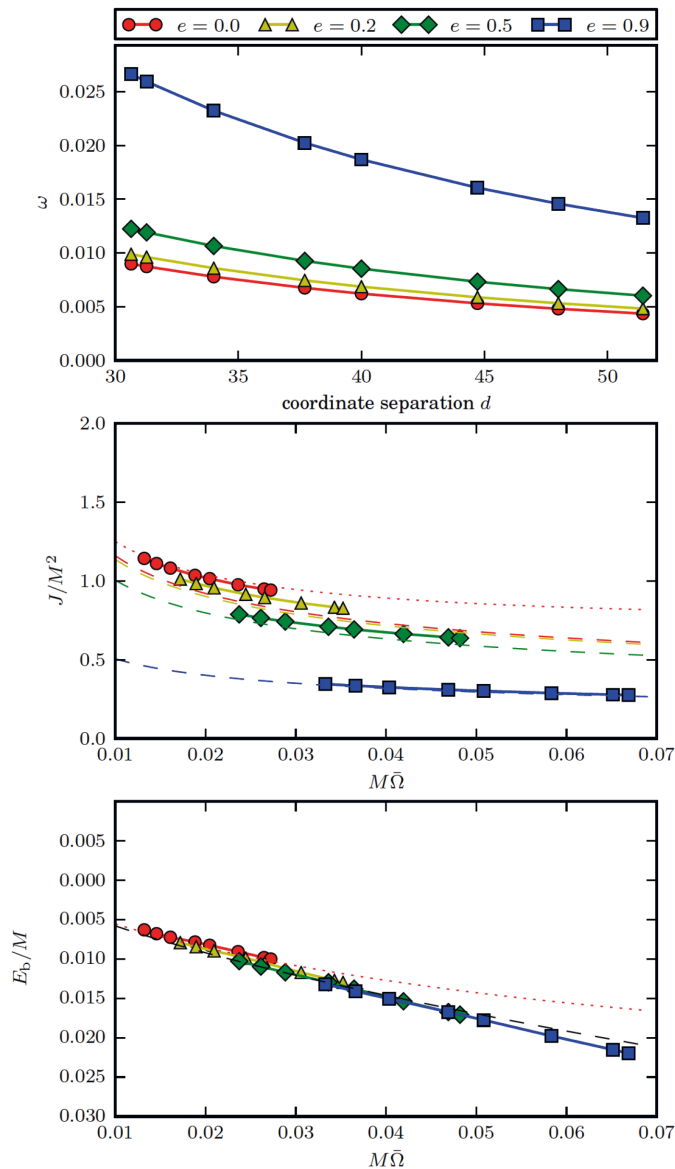


Figure 5.7: Shown are sequences for BNS with equal masses and varying eccentricity, where the eccentricity parameter e ranges from $e = 0$ to $e = 0.9$, i.e. we cover the limit of quasicircular sequences and go close to head-on collisions (see Tab. 5.1 *mgSeq*). The data has been computed with BAM for stars with individual gravitational masses of $M_{A,B} = 1.5149$ (compare Tab. 5.1). The top panel shows the rotation ω as a function of the coordinate separation of the two stars' centers. In the middle and bottom panel, we give the ADM angular momentum J_{ADM} and the binding energy E_b in dependence of the normalized mean motion $M\bar{\Omega}$. Dashed lines represent the expected Newtonian behavior (black in the lower plot, since in this case all Newtonian curves coincide) and the dotted lines denote the 3PN prediction for $e = 0$. Figure taken from [Mol1].

We can now come back to consider eccentric equilibrium sequences, where we show the dependency of the binding energy E_b and the ADM angular momentum J_{ADM} on the orbital frequency Ω . It has to be mentioned that the usual orbital frequency is no longer appearing in the Killing vector as in the circular case. For eccentric systems we use the orbital mean motion $\bar{\Omega}$ instead of ω (which is the internally used computational quantity in the new symmetry vector (3.31a)) or Ω . The reason is that only $\bar{\Omega}$ satisfies Kepler's third law in the Newtonian limit. In particular, increasing either ω or $\bar{\Omega}$ corresponds to decreasing the binary's initial coordinate separation. We expect from the Newtonian limit that the frequency decreases with increasing eccentricity e , which is only true for $\bar{\Omega}$, while $\omega \propto 1/\sqrt{1-e}$ in the Newtonian limit. The increase of ω with larger eccentricities is illustrated in the top panel of Figure 5.7.

The lower two panels of the figure show the sequences computed with BAM and compare them to Newtonian theory. Note that we also include the well studied case of circular orbits $e = 0$ and see a qualitative agreement of the results with Newtonian estimates. In this case we can further improve the agreement by considering higher order post-Newtonian calculations as done by Mora and Will [2004] so that the deviation from our circular data is less than 1%. For brevity, we do not show sequences computed with SGRID explicitly here, since the circular case was considered already by Tichy [2012]. Tichy demonstrated a nice match of irrotational data with PN theory and our results of SGRID for $e = 0$ are the same, while the BAM data are visually almost on top of that. However SGRID data is slightly more accurate (especially for lower separations) due to the precise treatment of the velocity potential. The similarity of the data computed by the two implementations is the same for eccentric orbits, thus we only show the BAM sequences.

The eccentric sequences in Fig. 5.7 reveal a qualitative agreement with Newtonian theory as it is indicated by the dashed lines. The binding energy E_b degenerates in the Newtonian limit and is independent of the eccentricity

$$\frac{E_b}{M} = -\frac{\eta}{2}(M\bar{\Omega})^{2/3}, \quad (5.1)$$

where $\eta := m_1 m_2 / M^2$ denotes the symmetric mass ratio, with M the total mass, so $\eta = 1/4$ in the equal-mass case we are considering. We see in the lower panel, that our solution approximately describes such behavior. The angular momentum in

Newtonian theory¹ is given by

$$\frac{J}{M^2} = \eta(1 - e^2)^{1/2}(M\bar{\Omega})^{-1/3} \quad (5.2)$$

and indeed, we see J decreasing for larger eccentricities. The next step we initially intended to investigate in [Mol1] as well, is an extension of our PN comparison. Similar to the improved matching of our results for circular orbits with 3PN calculations, we expected an improvement for eccentric orbits compared with 3PN over Newtonian theory. Again, the PN calculations were taken from Mora and Will, however the results we obtained were not in a good agreement with our data. After reconsidering our ansatz it turned out that the PN results obtained in that manner are not well-behaved for head-on collisions. In our scheme, we approach such configurations for increasing eccentricities and reach them for $e = 1$. On the other hand, Mora and Will approach an unbound parabolic orbit, i.e. with nonzero angular momentum, hence our comparison is not valid and one cannot expect it to work at large eccentricities. Sec. 10 of Blanchet [2014] gives an approach to alternative quasi-Keplerian parametrization of eccentric orbits. This could be a solution for this issue, since these solutions remain well-behaved even for vanishing angular momentum through 1PN. Unfortunately it is not clear how to relate the quantities used to describe the orbit in this parametrization to our $\bar{\Omega}$ variable using only data at apoapsis. Additional complications might arise from the fact that the zero angular momentum limit is special even in the Newtonian limit, since all three types of orbits (elliptic, parabolic, and hyperbolic) degenerate to head-on collisions when the angular momentum vanishes, as discussed in Spherhake et al. [2008]. Thus it is not surprising that the PN results do not match our eccentric data as initially expected.

In [Mol3] we compared eccentric sequences computed with SGRID and we chose a different approach. Because of the compactified grid, which includes spatial infinity, SGRID is capable of calculating the ADM quantities E_{ADM} and J_{ADM} more precisely than BAM's multigrid solver. We can thus try to compute the PN eccentricity based on these expressions and compare to the eccentricity parameter e we plug in. The results are shown in Fig. 5.8. The SGRID data is computed with $n_A = n_B = 24$, $n_\phi = 8$ and $n_{\text{cart}} = 20$ points and we choose the same physical setup as for the data computed with BAM before. A feature that all plots of that figure have in common is the nice

¹to derive this and the previous equation one plugs $\Omega_a = [(1 - e)/(1 + e)^3]^{1/2}\bar{\Omega}$ into Eqs. (2.2) in Mora and Will [2004]. The expression for the angular velocity at aphelion, Ω_a , in terms of $\bar{\Omega}$ comes from the standard Newtonian expressions above Eqs. (2.2) in Mora and Will, noting that $\bar{\Omega}^2 = M/a^3$, where a is the binary's semimajor axis, by Kepler's third law.

convergence of the PN eccentricity (denoted by \hat{e}_{harm} , where the index stands for harmonic coordinates) towards the input eccentricity for large distances of the neutron stars. However, as can be seen in the bottom panels, only small eccentricities behave properly if we increase the PN order. For larger values of $e = 0.5$, increasing PN orders do not lead to better agreements of input and PN eccentricity, since the 1PN results are closer to the input value than the 3PN results. The intention behind this kind of comparison was to avoid using PN expressions that are not well-behaved for large eccentricities, which corresponds to head-on collisions in our scheme. However, even if we started with regular expressions (in particular we constructed $\tilde{E}\tilde{J}^2$ from Mora and Will's expressions such that it is well behaved for large e) we end up with terms that can blow up at higher PN orders if we finally compute the PN eccentricity. Hence as e goes to one, the comparisons become worse. A more detailed description of the computation of the PN eccentricity can be found in [Mol3]. In short, we take 3PN expressions for the eccentricity derived from Mora and Will [2004] in harmonic coordinates (we also used ADM coordinates and found only minor differences as expected). The PN series of the binding energy² \tilde{E} can be inverted, so that the PN expansion parameter ζ can be expressed in terms of \tilde{E} . Using this expression, we can eliminate ζ from the PN angular momentum \tilde{J} . Ultimately this allows us to expand a series of \tilde{E} and \tilde{J} to construct the square of the eccentricity parameter \hat{e}_{harm} .

Due to the shortcomings of that PN expansion for large eccentricities, we also looked at PN expressions given by Memmesheimer et al. [2004]. Although these are singular for vanishing angular momentum (which occurs in head on collision) at constant energy, they give good agreement even for relatively large eccentricities. We computed the three eccentricities (e_r , e_ϕ and e_t) defined from post-Keplerian parametrization (see equation (20) and (25) within Memmesheimer et al. [2004]), where we again plugged in the values of the binding energy and angular momentum obtained from SGRID. In particular, the value of e_t is in good agreement with the specified eccentricity and we find a maximum deviation of $< 2.4\%$ for all considered separations of the $e = 0.5$ sequence.

5.2.3 Trajectories and waveforms

Transitioning from circular orbits to head-on collisions by decreasing the tangential velocity yields an intuitive picture of the “orbits” one obtains. The smaller velocity should lead to a less circular orbit as the stars fall faster towards each other. We

²here the tilde just denotes a rescaling of our quantities in comparison to Mora and Will. Again, details are given in the corresponding paper.

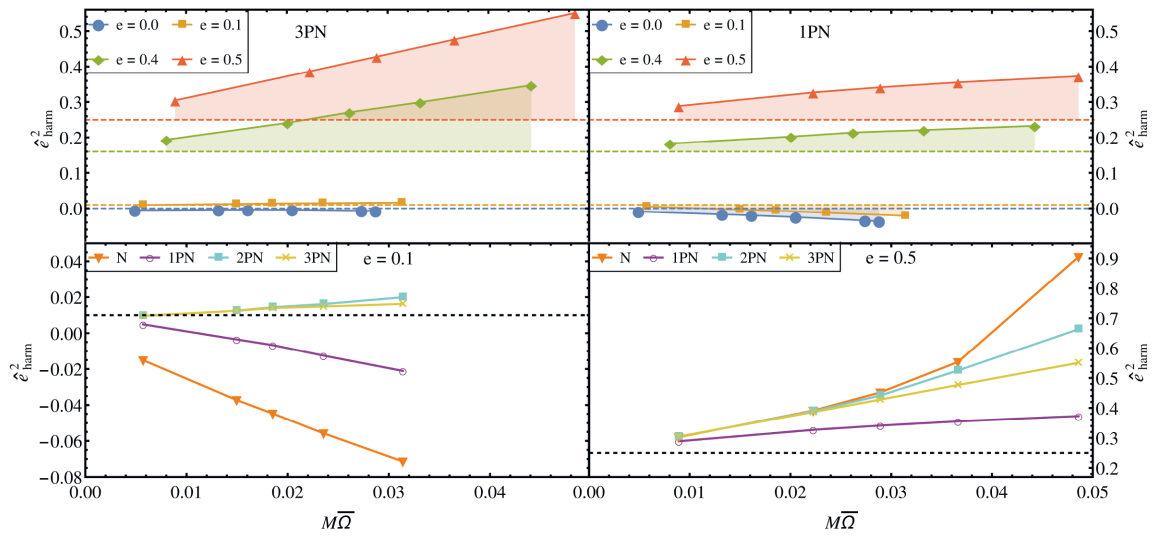


Figure 5.8: This figure shows different comparisons of initial data computed with SGRID and PN estimates (datasets *sgSeq0–sgSeq0.5*). In the top panels, we compare our data to fixed PN order (3PN on the left and 1PN on the right), while we compare different PN orders at fixed eccentricities ($e = 0.1$ left and $e = 0.5$ right) at the bottom panel. All panels show the squared eccentricity \hat{e}_{harm}^2 as calculated from the ADM energy E_{ADM} and angular momentum J_{ADM} using PN expressions. The dashed lines denote the input eccentricities and all four panels show convergence of \hat{e}_{harm}^2 towards the input eccentricity for larger distances. Also, for small eccentricities we see convergence with increasing PN order. All plots are given as a function of the normalized mean motion $M\bar{\Omega}$. Adopted from [Mol3].

characterize these orbits by the stars trajectories, which are defined as the local minimum of the lapse during an evolution. We want to ensure that our data shows the physical features which eccentric initial data are required to have. Before we can discuss further details, it is necessary to agree on the terminology and the way we measure eccentricities.

Eccentricity definitions

As we mentioned before, our scheme is only exactly valid in the limit of Newtonian point particles. Thus we do not expect the eccentricities that occur in our fully general relativistic evolution to perfectly match the initially specified eccentricity. Nevertheless, this does not pose any serious problems, since we do not necessarily need to specify a certain eccentricity, but want to be able to set up consistent eccentric initial data. Later we can use empiric relations of the input eccentricity e_{ID} ,

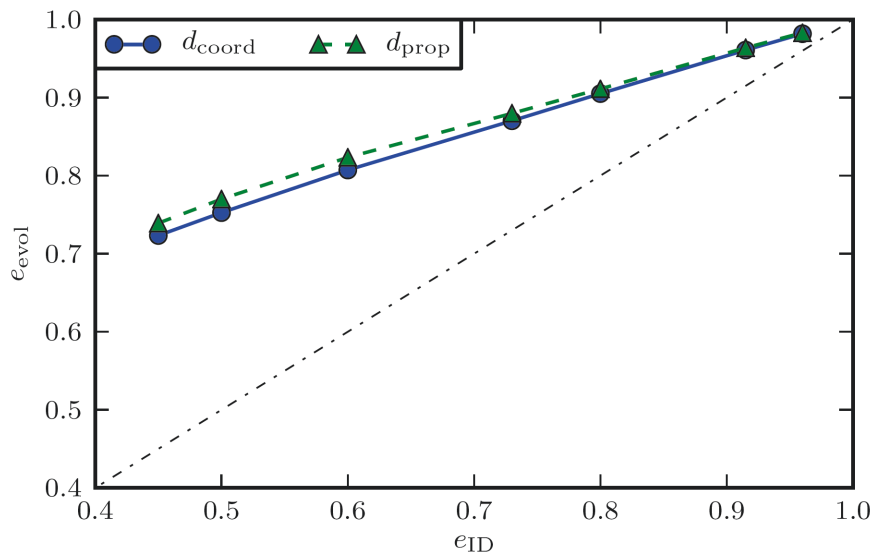


Figure 5.9: Shown is the relation of the eccentricity we specify as a parameter for initial data computation e_{ID} and the eccentricity we measure during evolutions e_{evol} . The black dashed line gives the “ideal” relation $e_{ID} = e_{evol}$. Our results from *mgEcc0.45–MgEcc0.96* datasets in Table 5.1 are plotted as blue and green lines. We distinguish between different methods to measure the eccentricity, where one is based on the coordinate distance, while the other relies on proper distance as described in more detail in the text. Both curves agree within the tolerance so that they can serve as empirical relations to estimate the final eccentricity before computing data.

which is the specified initial data parameter³, and the eccentricity during evolution e_{evol} to easily obtain the desired orbits.

A major problem with these relations is that there exists no obvious method to determine the eccentricity of a comparable mass system in general relativity. In the literature one can find numerous ideas on how to estimate the eccentricity in evolutions. Mroué and Pfeiffer [2012] give several references and more recently, Kyutoku et al. [2014] also worked on this topic. However, most of these methods are designed to work for small eccentricities (of the order $\lesssim 0.1$) and are not appropriate for the highly eccentric systems we are interested in. A possible way to give a reasonable estimate of the eccentricity of the system is to fit an ellipse to a short section of the trajectory. Ideally, this section is taken from the beginning of the simulation, but late enough that the initial perturbations have settled down. It is expected that the trajectories are approximately elliptical in these segments, since radiation reaction and other strong-gravity effects did not have much time to affect the orbit. A

³Note that we often drop the index *ID* for simplicity. In this section we refer to the eccentricity parameter e as e_{ID} and we return to the short notation afterwards.

quick estimate can be given by fitting the coordinate trajectory directly to an ellipse. One has to keep in mind that the coordinate distance is gauge dependent and one would likely want to estimate the extent of the gauge dependency on the eccentricity measure. Therefore, we compute the position angle of the trajectory and the proper distance between the stars and construct a “proper distance trajectory”, which we then fit with an ellipse. Note the caveat that the proper distance in BAM is not exactly gauge invariant, since it is not measured along a geodesic. It still depends on the foliation, but is much less influenced by initial gauge choices.

In highly relativistic simulations it does not make sense to define an orbit as a full ellipse in view of the fact that orbital precession and radiation reaction will radically affect the orbit. On the other hand we do not have to define such orbits; we just need a segment of the trajectory and find the best fit of an ellipse to that section in order to obtain the eccentricity. This procedure does not require us to define a semimajor and semiminor axis for the orbit as a whole, as one would expect from the Newtonian definition $e = (1 - b^2/a^2)^{1/2}$.

In Fig. 5.9 we show the relation of e_{evol} and e_{ID} for the two different fitting procedures of the ellipse. To compute this figure we fixed the central enthalpy $h = 0.255$ in BAM’s multigrid solver, which results in a star with an isolated gravitational mass of 1.399. We further fix the coordinate separation to $d = 80$ and only vary the eccentricity parameter. The evolution setup is the same as in the previous sections with sixth order finite differencing and eighth order dissipation as it is appropriate. Fortunately, the results are comparably stable with respect to different masses. More precisely, we found that changing the stellar mass by $\sim 10\%$ amounts to a change in e_{evol} of less than 0.5%, independent of the method used to compute it. The two methods agree with each other within 3% for eccentricities larger than $e \geq 0.4$, which is enough for our purpose of estimating the evolution eccentricity. Note that we also experimented with the intervals we considered for the elliptical fit. In particular, we varied the length interval of the section from 200 to 3000 points, which corresponds to coordinate displacements from ~ 0.8 to ~ 9 or a evolution timespan of $\Delta t \sim 30$ to $\Delta t \sim 200$. All experiments yielded deviations of $\sim 1\%$, or even less if one just considers medium sized intervals and leaves out the very first points.

Extrapolating the results of Fig. 5.9, we would obtain $e_{\text{evol}} = 0.5$ for vanishing input eccentricity, while the actual fits would yield around 0.2 to 0.3 output eccentricity in these cases, depending on the fitting procedure. One immediately sees that the fits are more sensitive in these regimes and the deviation of different methods is larger. Also the “real” residual eccentricities should be around 0.01, which shows that the

ellipse fitting method is not applicable for small eccentricities and thus we only use it for $e \gtrsim 0.5$. In Sec. 5.3 we consider low eccentricities and different measurement techniques that are more suitable.

We are aware that these estimates are not gauge independent and that other groups may have different results. For example the Princeton group [East and Pretorius, 2012; East et al., 2012a; Stephens et al., 2011] studied highly eccentric systems in generalized harmonic coordinates, which could considerably deviate from our results. However, in light of the above results from Fig. 5.9, we can use the relation of input and evolution eccentricity to give a very reasonable estimate of the system's character. Furthermore, the figure also shows that the eccentricities are behaving well in the sense that e_{evol} increases monotonically with e_{ID} .

The gauge independent quantity that would be preferable is the gravitational waveform. Unfortunately, the highly eccentric evolutions do not perform several inspirals before merger, but in most cases very short plunges or chaotic zoom whirl orbits. Quantities such as GW frequency or amplitude are hard to measure in these cases and not suitable for eccentricity estimates.

Evaluating eccentric orbits

Finally we want to check the physical properties of the initial data we have constructed. Looking at Fig. 5.10, we find that the orbits are indeed crucially depending on the value of the eccentricity parameter e . The performed evolutions are done with initial data from BAM's multigrid with a fixed central enthalpy $h = 0.255$ just as before when we considered the eccentricity estimates and the evolution setup is the same. The trajectories show the expected behavior, i.e. the orbits are less circular for large values of the eccentricity parameter e and approach a direct head-on merger for $e \rightarrow 1$. However, these short evolutions are less interesting than the more complicated setups we can find. Similar to the results of Gold et al. [2012] for superimposed initial data, we can produce orbits with one or several encounters before merger. For the specific separation and stellar mass, we find $e = 0.45$ to generate an orbit with two encounters before merger. Later we consider more generic setups constructed with SGRID with even more encounters, but for a first analysis we want to stick with the BAM multigrid initial data. The setups in the figure are chosen such that they are close to the data sets considered by Gold et al., although they are not exactly the same. It is desirable to have a close comparison to these setups. However, finding such configurations is not trivial, since small differences have a huge influence on the overall trajectory. The resulting gravitational waves differ and a comparison

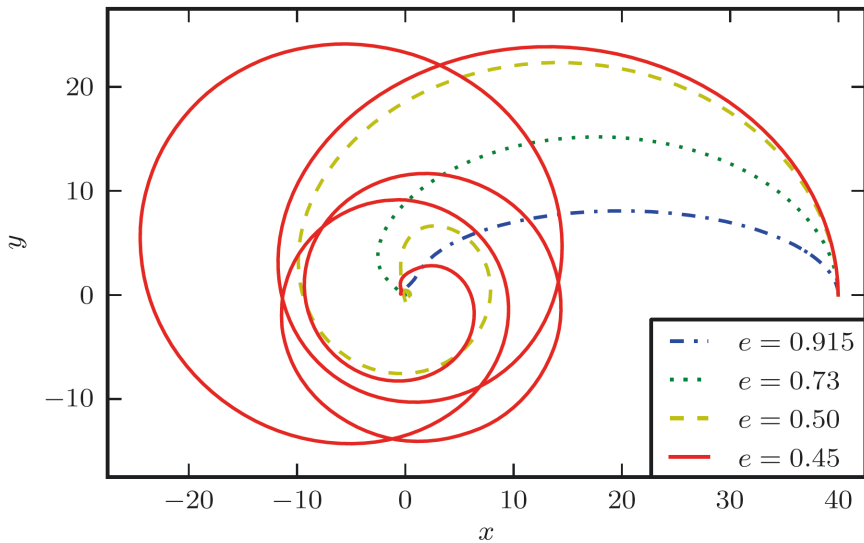


Figure 5.10: The trajectories of one star from an equal mass binary with varying eccentricity parameter e . The setup is the same for all four different runs, apart from e as can be seen in 5.1 from which we use $MGe0.45$, $MGe0.5$, $MGe0.73$ and $MGe0.915$. The influence of e on the star's trajectory is crucial. While large values lead to a direct merger, smaller values can be found which produce one or more encounters. Plot adopted from [Mol1].

might not be very illuminating. Moreover, comparing the trajectories is also not very helpful, because the coordinate trajectories and thus gauge dependent. Although we choose the same gauge conditions during the evolution as Gold et al., we do not have the same initial gauge. While we are initializing the lapse and shift with values computed by our initial data solver, Gold et al. use a zero shift initialization. Regardless of gauge initialization, the data are in a region of phase space, which is sensitively dependent on initial parameters, such as velocity (profile), separation or mass. The bottom line is that we can see the same qualitative behavior, i.e. zoom-whirl features where the separation decreases and subsequently increases again, as for superimposed data. But especially the first segments of the trajectories of the superimposed data look different compared to ours. In cases where we reproduce the qualitative features of zoom-whirl orbits for similar separations and masses as Gold et al. used, we have initially less eccentric trajectory segments. This issue is also related to the question how to define the eccentricity of the obtained orbits, particularly if we keep in mind that the trajectories are gauge dependent. We discuss this at the end of this section, but we discuss the gauge independent gravitational waves of the $e = 0.45$ run first.

The waveform, given in terms of the $\ell = m = 2$ mode of the Newman-Penrose scalar Ψ_4 , can be seen in Fig. 5.11 and reveals some interesting features. On the x -axis we

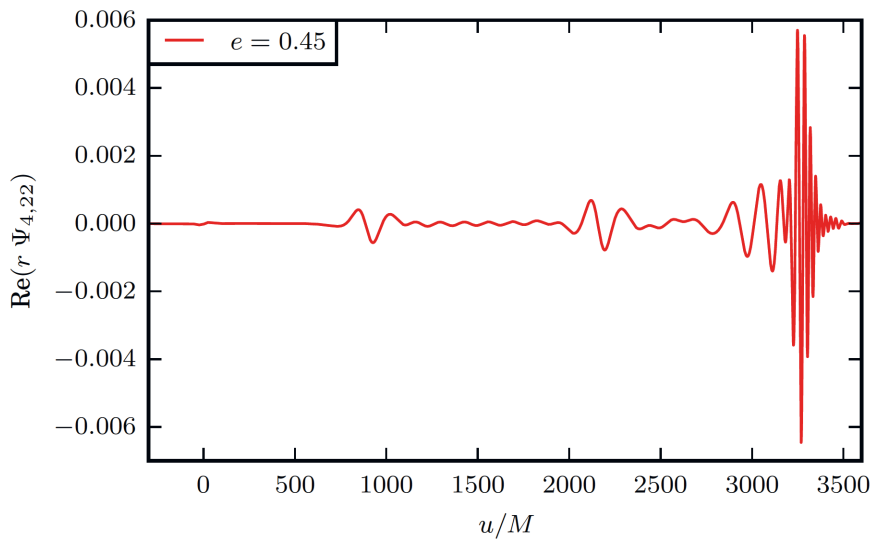


Figure 5.11: The gravitational waveform expressed through the $\ell = m = 2$ mode of the Newman-Penrose scalar Ψ_4 for the *mgEcc0.45* case (see Table 5.1). We extracted the waveform at a distance $r = 500$ from the binary’s center-of-mass and use the retarded time u for the x-axis (see text) to account for the wave’s travel time. The two small bursts (at $u \simeq 900M$ and $2100M$) correspond to close encounters before merger. One can also see the tidally induced f -mode oscillations of the stars inbetween the bursts. Plot adapted from [Mol1].

show the retarded time

$$u = t - r_* = t - r - 2M \ln(r/2M - 1), \quad (5.3)$$

which accounts for the wave’s travel time and where r denotes the extraction radius. Instead of the well known inspiral waveforms, which monotonically increase in amplitude and frequency until merger (the famous chirp signals), we obtain a completely different signal since we do not observe a long inspiral phase but merely a couple of “orbits”. While the stars approach each other there is almost no measurable signal until they are near periastron where we measure a burst. Then the two companions move apart and high frequency oscillations can be measured until the next burst during another encounter encounter. Finally, the stars merge and the merger signal can be seen. The same qualitative features were observed by Gold et al.. In particular, the high frequency oscillations between the bursts have been measured and assigned to stellar oscillations induced by tidal forces. We checked the frequency of these f -modes for an isolated non-rotating star with the same baryonic mass and equation of state as in our setup and found that the frequency agrees with the interburst signal. In particular, we compute this frequency using the fits given in Lau et al.

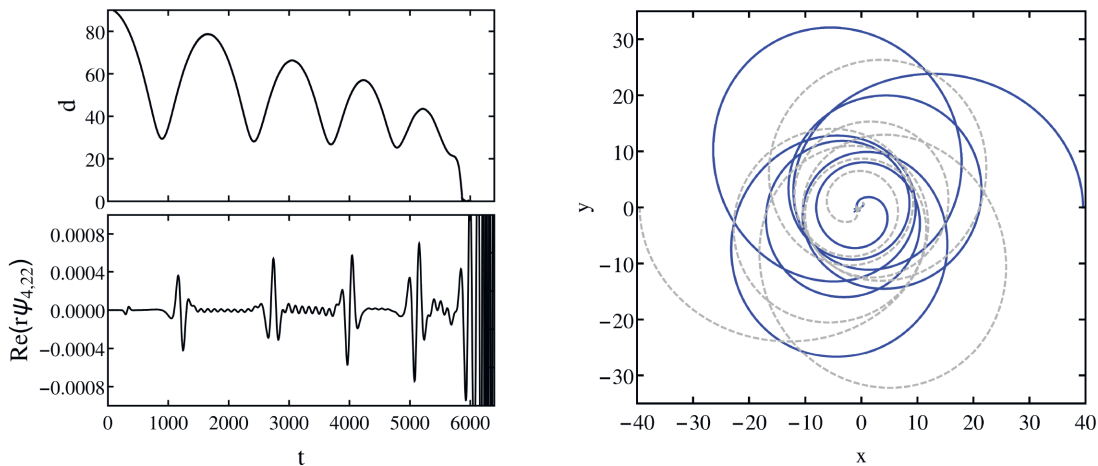


Figure 5.12: Illustrated is an SLy run with an eccentricity of $e = 0.45$, compare *sgEccSLy* from Table 5.1, which leads to four encounters before merger. We show the trajectories of the stars on the right panel, where star 1 is denoted by the solid blue line and star 2 by the dashed gray line. On the left panel, the proper distance and the real part of the mode $(2, 2)$ of Ψ_4 are shown as functions of time.

[2010] and the values of 1.399 and 9.586 for the isolated star’s gravitational mass and areal radius. We perform a similar analysis for different EoSs and find interesting orbits with several encounters. Fig. 5.12 shows the evolution of the SLy setup from Table 5.1 with the same eccentricity parameter as for the $\Gamma 2$ setups. We evidently see differences of those evolutions, originating from different EoS. The SLy setup results in four encounters before merger as it can be seen in all panels, most easily in the upper left plot, which shows the proper distance. We see the interburst signals in the $(2, 2)$ mode of the gravitational waveform Ψ_4 with frequencies matching the f mode oscillations. The amplitude of these oscillations is varying from encounter to encounter. Depending on the phase at which the oscillations are excited, the amplitude is increased (for instance after the second encounter) or even decreased (see the third encounter). The right panel shows the trajectories, which produce a fairly crowded but interesting path.

5.3 Eccentricity reduced orbits

So far we have only used one of the two introduced additional parameters provided by our hellicptical symmetry vector Eq. (3.50), namely the eccentricity parameter e . We used this to control the tangential velocity of the star and left the radial velocity parameter $v_r = 0$ unattended.

5.3.1 Eccentricity reduction scheme

In subsection 5.2.3 we discussed how to estimate large eccentricities in the evolutions and later in this section we show how small eccentricities can be measured by applying different techniques known in literature.

Assuming for the moment that we are able to accurately measure those eccentricities and we consider “circular” data in a sense that $e = v_r = 0$ in our initial data computation. In this case we measure a non-vanishing evolution eccentricity $e_{\text{evol}} \sim 0.01$ and the influence is sufficiently large that it can be seen with the naked eye by looking at the proper distance (compare the results we obtain in Fig. 5.14 and Fig. 5.15). However for the vast majority of astrophysical scenarios these eccentricities are of completely artificial nature. During the long lasting inspiral phase, the corresponding GW emission would efficiently circularize the orbit so that the eccentricity should vanish before merger. Kowalska et al. [2011] report that the measured eccentricity at merger of the six binary neutron star systems, which will coalesce within a Hubble time, will be $e_{\text{evol}} \lesssim 10^{-5}$. Hence, the expected eccentricities are several orders of magnitude smaller than what is often employed by the numerical relativity community.

These residual eccentricities influence various quantities, but the main effect can be observed on the gravitational waveform. In [Mol1] we already outlined a procedure to iteratively reduce the artificial eccentricity, which was based on studies done by Pfeiffer et al. [2007] and Husa et al. [2008], who reduced the eccentricity for binary black holes. We explained our method in detail in [Mol3] and presented results for eccentricity reduced neutron stars. In the meantime, Kyutoku et al. [2014] used a similar technique to compute eccentricity reduced neutron star binaries as well. Next, we describe the method we used to minimize the residual orbital eccentricity by tweaking the two parameters e and v_r in our approach.

In order to set up such a method we need two ingredients, i.e. (i) a measure for low eccentricities and (ii) a scheme for finding better suited parameters for initial data construction. Here we use two different approaches to measure the eccentricity, where one uses the gravitational wave frequency ω to estimate the remaining eccentricity e_{evol} , while the other uses the proper distance d inside the hypersurface. As already mentioned in the previous section, the latter is measured within BAM along the coordinate line connecting the two local minima of the lapse, corresponding to the centers of the two stars, and is not exactly gauge independent. However it is much less influenced by gauge choices than the coordinate distance d_{coord} , which is considered by others to estimate the eccentricity and thus seemed to be the better choice. For

more details, see also the description of the crucial impact of initial gauge choices on eccentricity reduction with the coordinate distance in Kyutoku et al. [2014]. After measuring e_{evol} , we apply corrections to the tangential and radial velocity that would remove the eccentricity from a Keplerian orbit (see the above mentioned works for black hole binary realization of this idea).

We assume that the stars are moving towards each other with a linearly increasing speed during the evolution, which means that the proper distance is second order polynomial in time. The ellipticity part of the model is given by $-\frac{B}{\omega} \cos(\omega t + \phi)$. Altogether we are modeling the proper distance as

$$d(t) = S_0 + A_0 t + \frac{1}{2} A_1 t^2 - \frac{B}{\omega} \cos(\omega t + \phi) \quad (5.4)$$

and try to find the best fitting parameters for our data. Note that it is as well possible to fit the time derivative $\dot{d}(t)$ instead. The advantage is the reduction of the fitting parameters, but for lower eccentricities the computation of the time derivative of d introduces noise and makes the fit more complicated. We have tried both methods and also apply low-pass filters to help improving the results. There is no clear conclusion which model, i.e. fitting either d or \dot{d} works better. We notice the tendency that the direct fits of d yield slightly better results in terms of residual eccentricity after a fixed number of iterations, thus we employ that model, although the following procedure is the same for both.

For a Keplerian orbit, the stellar separation is described by

$$d_{\text{Kep}}(t) = \frac{2p}{1 + e \cos[\phi(t)]}, \quad (5.5)$$

where p is the semi-latus rectum and ϕ is the true anomaly, i.e. the angle between the star's current position and its location at apoapsis. We can write the derivative of the distance as

$$\dot{d}_{\text{Kep}}(t) = \frac{d_0 e \omega \sin[\phi(t)]}{1 + e \cos[\phi(t)]} \approx e \omega d_0 \sin[\phi(t)] + \mathcal{O}(e)^2. \quad (5.6)$$

Here we used $\dot{\phi} = \omega$ and d_0 denotes the initial separation and we approximated the result by assuming the eccentricity e is small. Comparing (5.4) and (5.6) yields an eccentricity

$$e = \frac{B}{d_0 \omega}, \quad (5.7)$$

The radial velocity caused by the ellipticity, i.e. the component of \dot{d} originating from

the cosine term, is given by $B \sin(\phi)$. Hence, we have to correct the initial radial velocity v_r by

$$\delta v_r = -B \sin \phi \quad (5.8)$$

in order to remove the eccentricity caused by the radial velocity. After fixing the radial component, it remains to correct the orbital angular velocity Ω , which induces artificial eccentricity by radial acceleration and can be controlled via the eccentricity parameter e . The relation of the orbital angular frequency at apoastron Ω_{apo} to the orbital angular frequency of the quasi-circular data is given by $\Omega_{\text{apo}} \approx \sqrt{1-e}\Omega_0$. Changing e by a small δe leads to a change in Ω by $\delta\Omega \approx \frac{-1}{2\sqrt{1-e}}\Omega_0\delta e$. In general, a change of the orbital Ω by $\delta\Omega$ yields a change of the acceleration $\Omega^2 d_0/2$ by $d_0\Omega\delta\Omega$. Similar to the considerations for the radial velocity, the ellipticity contribution of the radial acceleration of one star is given by $(B\omega/2)\cos(\phi)$. Thus, the correction we have to add to the eccentricity parameter in order to balance the orbital acceleration is

$$\delta e = \frac{B\omega \cos(\phi)}{d_0\Omega_0^2} \sqrt{1-e}. \quad (5.9)$$

In summary, we can track the proper distance of the stars during an evolution for the first one to two orbits. This is sufficient to fit the proper distance to our model (5.4). Afterwards we can compute the necessary corrections (5.8) and (5.9) and start a new evolution. We can iterate over this procedure and in most cases two or three iterations are sufficient to drive the residual eccentricity down by more than an order of magnitude. A reduction of that order is similar to the findings reported by Pfeiffer et al. [2007] for black holes. Note that it is not possible to arbitrarily reduce the eccentricities, since after $\gtrsim 5$ iterations the measured distance is too smooth to accurately apply our fitting procedure.

As mentioned in the beginning of this section, we want to give another estimate of the eccentricity in order to verify our results. Instead of the proper distance we employ the gravitational waves. The eccentricity of an evolution estimated based on GWs is denoted by e_{GW} . To determine e_{GW} we follow the description of Walther et al. [2009], which itself is based on Baker et al. [2007]. Post-Newtonian calculations suggest to model the GW frequency as

$$\omega_{\text{fit}} = \frac{1}{4}\tau^{-3/8} (1 + c_1\tau^{-1/4} + c_2\tau^{-3/8}), \quad (5.10)$$

where c_1, c_2 are determined by fitting and

$$\tau^2 = \frac{\eta^2(t_c - t)^2}{25M^2} + d^2. \quad (5.11)$$

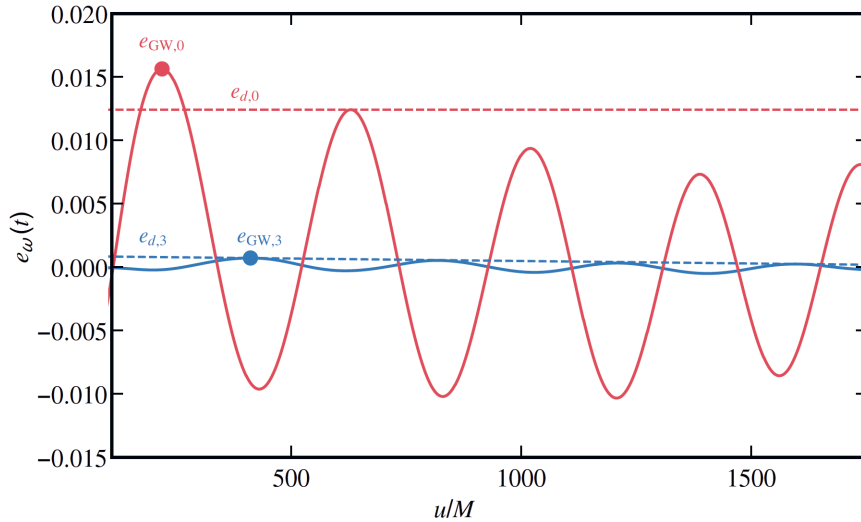


Figure 5.13: The eccentricity estimated from the gravitational wave frequency ω as a function of the retarded time u . The initial data are computed with SGRID for SLy equation of state with an initial separation $M\omega_{22} = 0.0365$. We show quasicircular data for $e = v_r = 0$ (red) and the third iteration of the eccentricity reduction (blue). The global extremum is marked by the points and gives the eccentricity estimate of these runs. We find $e_{\text{GW},3} = 0.00084$ and $e_{\text{GW},0} = 0.0156$ respectively, which is a factor of 20 improvement. The horizontal dashed lines mark the eccentricities e_d calculated based on the the proper distance. Plot adapted from [Mol3].

Here, t_c and d are further fitting parameters and $\eta = m_1 m_2 / M^2$ is the symmetric mass ratio. We measure the eccentricity based on the gravitational wave frequency

$$e_\omega(t) = \frac{\omega(t) - \omega_{\text{fit}}(t)}{2\omega_{\text{fit}}(t)}. \quad (5.12)$$

Equation (5.12) depends on time and is strongly oscillating. Nevertheless, we can use it to define a time independent measure of the eccentricity by computing the global extremum

$$e_{\text{GW}} = \max_t |e_\omega(t)|. \quad (5.13)$$

As one can see for example in Fig. 5.13 and as one would intuitively expect, this maximum occurs for the vast majority of simulations in the beginning. Note that we cut off the initial noise at the first time steps in order to obtain reasonable results. We additionally compare the estimates obtained via gravitational waves with estimates based on the proper distance fits for the standard quasicircular setup $e = v_r = 0$ and for the third iteration of the eccentricity reduction procedure (more details on the setups can be found in table 5.2). One can clearly see that these estimates agree

Table 5.2: The results of applying our eccentricity reduction iteration to two binary setups. The stars distance is given by $M\omega_{22} = 0.0365$ in both cases. The first configuration is a $\Gamma 2$ binary with individual masses of $M^A = M^B = 1.515$ and a total ADM mass of $M_{\text{ADM}} = 3.006$. The second one is an equal mass SLy configuration with $M^A = M^B = 1.350$ and $M_{\text{ADM}} = 2.6782$. For both runs we performed three iterations of the method and give the parameters e and v_r that are used as input. We further measure the remaining eccentricity during evolution e_{evol} based on the proper distance, so we call it e_d here. Additionally we provide the values of the binding energy $E_b = M_{\text{ADM}} - M$ and the angular momentum J_{ADM} , which we normalize by M and M^2 , respectively.

EOS	Iter	e [10^{-3}]	v_r [10^{-3}]	e_d [10^{-3}]	E_b/M [10^{-3}]	J_{ADM}/M^2
$\Gamma 2$	0	0	0	9.77	-7.984	1.0700
	1	-6.8	-1.63	1.38	-7.922	1.0729
	2	-5.7	-1.14	0.91	-7.920	1.0738
	3	-6.3	-1.16	0.56	-7.920	1.0734
SLy	0	0	0	12.41	-8.115	1.0541
	1	-6.0	-1.13	7.80	-8.103	1.0580
	2	-12.1	-1.91	3.97	-8.088	1.0615
	3	-13.7	-1.09	0.87	-8.085	1.0625

quite well within roughly 5% (comparing $e_{\text{GW},3} = 8.4 \times 10^{-4}$ to $e_{d,3} = 8.7 \times 10^{-4}$ for the third eccentricity reduction iteration step of an SLy EOS run). Especially for lower eccentricities (i.e. higher iterations) the numerical noise is increasing relatively to the measured proper distance oscillations, and thus the accuracy of the proper distance fits is reduced. Therefore we expect both methods to deviate. On the other hand the qualitative agreement shows the consistency of the measures. For actual numerical computations it is beneficial to use the proper distance based estimates for iterative applications of the eccentricity reduction scheme. The reason is the increased runtime one would need to evaluate the gravitational wave signal. The proper distance is tracked immediately and we have to evolve the data for one or two orbits, while the gravitational waves additionally have to reach the extraction radius.

5.3.2 Trajectories and waveforms

The initial data for eccentricity reduction are exclusively computed with SGRID due to the increased accuracy. We presented the results in [Mol3] and have already previewed some of our findings for a SLy EoS run in Fig. 5.13. Additionally, we investigate a similar setup with polytropic $\Gamma 2$ EoS for two equal mass stars. Both initial data sets differ only in the EoS and thus the stellar masses. Details about the parameters and in particular about the iterative changes of the eccentricity reduction parameters can be found in table 5.2. To compute the data we used $n_A = n_B = 26$, $n_\varphi = 8$, $n_{\text{Cart}} = 22$

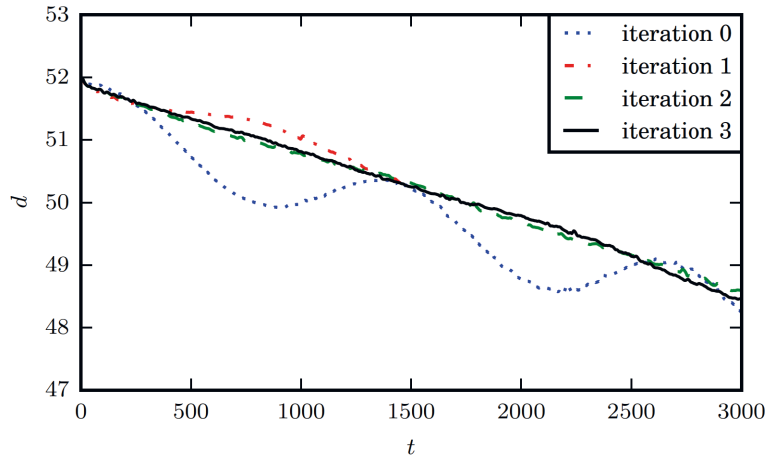


Figure 5.14: The proper distance d as a function of time for the polytropic $\Gamma 2$ setup from table 5.2. The original data is drawn as blue dotted line. The evolutions of the first and second iterative improvement are shown as red and green lines, while the third iteration is denoted by the solid black line. Plot adopted from [Mol3].

points in SGRID and for the evolution with BAM we used the constraint damping Z4c evolution scheme, as described in Bernuzzi and Hilditch [2010]; Hilditch et al. [2013]. The grid consists of seven refinement levels, where the two innermost boxes contain 96 points with a finest grid spacing of 0.15, while the outer boxes use 192 points and the grid spacing is doubled from level to level as usual. The outermost box is a cubed sphere with 192 points in radial and 84 points in azimuthal direction (see Bernuzzi and Hilditch [2010] for specific details and Ronchi et al. [1996]; Thornburg [2004] for a more general discussion on cubed spheres). Tab. 5.2 shows the results of the eccentricity reduction for different iteration steps. Initially, we measured large residual eccentricities of $e_{d,0} = 9.8 \times 10^{-3}$ for the $\Gamma 2$ setup and $e_{d,0} = 1.2 \times 10^{-2}$ for SLy. After three iterations we could decrease these to $e_{d,3} = 5.6 \times 10^{-4}$ and $e_{d,0} = 8.8 \times 10^{-4}$ respectively, which corresponds to improvements of at least a factor 20. In Fig. 5.14 we also show the $\Gamma 2$ setup’s proper distance d for the first two orbits as a function of time. The original circular data before our iteration procedure is clearly oscillating in the proper distance. The improvement after each iteration is evident and after the third iteration the oscillations are hardly visible.

Fig. 5.15 shows a setup similar to the $\Gamma 2$ setup, but with smaller initial separation so that the merger occurs earlier. One can see the trajectories of the stars with and without eccentricity reduction. Note that we have to initialize the simulation with zero shift in contrast to all other runs, in order to make the eccentricity intuitively visible in the tracks. One can clearly see that the trajectories are intersecting each other for standard circular data, whereas the improved data performs a fairly

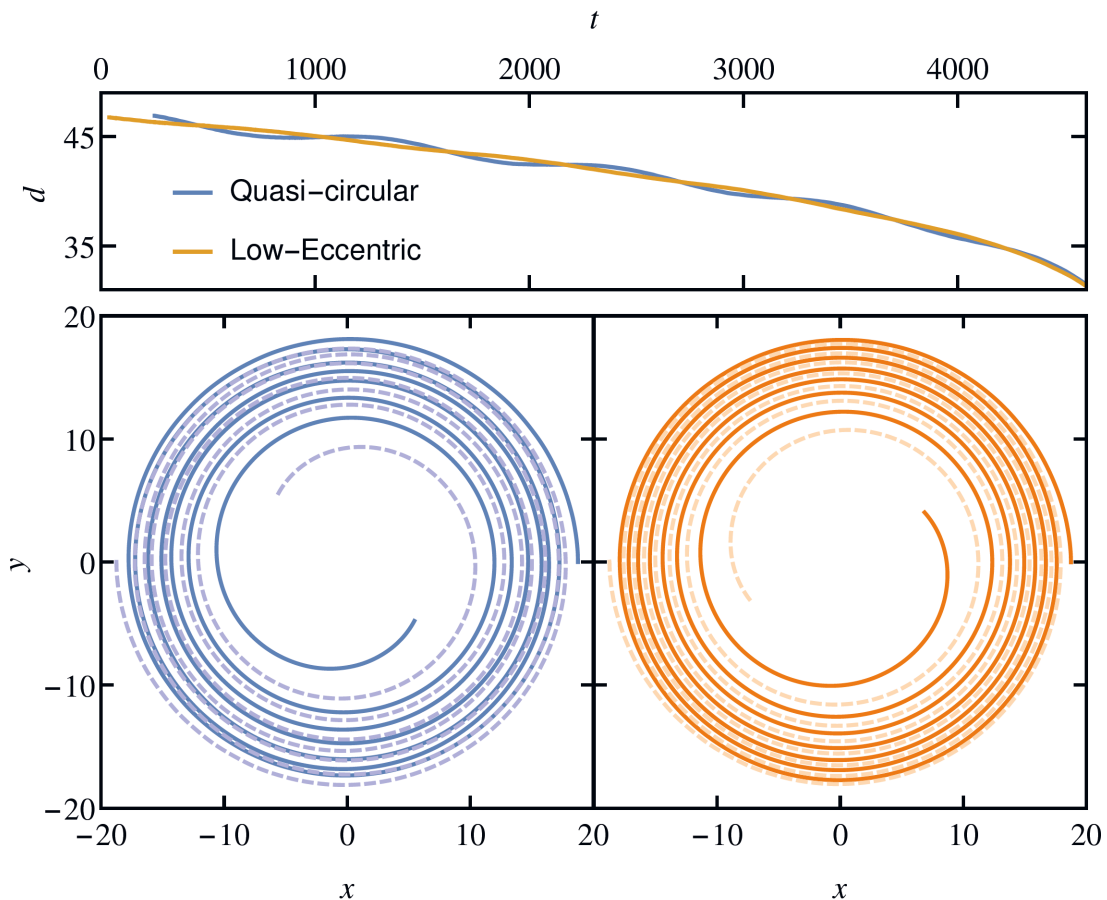


Figure 5.15: The trajectories of the centers of the stars for the original data (blue) and for eccentricity reduced data (orange). The solid and dashed lines distinguish between the two stars. The setup was chosen similar to the $\Gamma 2$ case from Table 5.2, but with closer initial separation, which results in fewer orbits and earlier merger. The eccentricity was reduced by an order of magnitude as the proper distance (top panel) shows as a function of time.

symmetric inspiral.

We can now discuss the influence of the residual eccentricity on the physical quantities. Additionally, it is possible to estimate the improvement of the data by looking at the ADM angular momentum and the binding energy and comparing with post-Newtonian calculations. Similar to Sec. 5.2.2, we look at PN expression by Mora and Will [2004], but an extension to fourth PN order does not change the results significantly. In view of the fact that the initial separations of the stars are rather large, we expect the third order post-Newtonian results for the ADM energy and angular momentum in terms of the binary's angular velocity to be fairly accurate. Indeed, we find that these quantities are closer to PN calculations for circular orbits,

if we consider our eccentricity reduced data sets instead of the original ones. Using the binding energy E_b and the angular momentum J_{ADM} as listed in Tab. 5.2, we compare those values to the PN results for

- (i) the SLy setup, where $J_{\text{ADM, PN}} = 1.0637M^2$ and $E_{b, \text{PN}} = -0.008088M$, and
- (ii) the $\Gamma 2$ setup, where $J_{\text{ADM, PN}} = 1.0730M^2$ and $E_{b, \text{PN}} = -0.007920M$.

In both cases we see the mentioned improvement. Case (i) yields a relative error of $\sim 1\%$ for the original data and an error of $\sim 0.15\%$ for the data at the third iteration. Furthermore, in setup (ii) we find a deviation of $\sim 0.4\%$ for the original and a deviation of $\sim 0.04\%$ for the eccentricity reduced data. Thus, the PN comparisons as well as the reduced proper distance and gravitational wave frequency oscillations prove the functionality of our iteration procedure.

Influence of low-eccentric data on waveform phasing

As already mentioned in the beginning of this section, Kyutoku et al. [2014] independently presented an eccentricity reduction procedure similar to ours. However, the influence on the GW phase and amplitude as relevant measurable quantities was not discussed. Thus we presented these observations in [Mol3] and summarize them in the following enriched with some more recent results.

The idea is to directly compare the data evolved with BAM and produced with SGRID, where we once use the eccentricity reduction iteration and once just compute $e = v_r = 0$ circular data. Such investigations are necessary since the eccentricity reduction procedure is computationally expensive so that one does not want to do it as default. Whenever truncation errors or other uncertainties affect the data such that their influence is larger than the gain of eccentricity reduction, we can skip that additional effort. Therefore we consider the SLy setup we used before (see Table 5.2) and a H4 EoS setup with the same mass and initial separation. The eccentricities are reduced from $e_d = 1.241 \times 10^{-2}$ (It0) to $e_d = 8.7 \times 10^{-4}$ after three iterations (It3) in the SLy setup. Similarly the H4 eccentricities during the evolutions are reduced from $e_d = 1.31 \times 10^{-2}$ (It0) to $e_d = 7.0 \times 10^{-4}$ (It3).

As before we focus on the dominant mode, i.e. the $\ell = m = 2$ multipole. The subscript is omitted for brevity. In order to accurately compare the waveforms they have to be aligned. we proceed as outlined in Bernuzzi et al. [2012b]. An interval $[t_1, t_2] = [1000, 6000] \simeq [370M, 2222M]$ is chosen, where the waveforms are brought

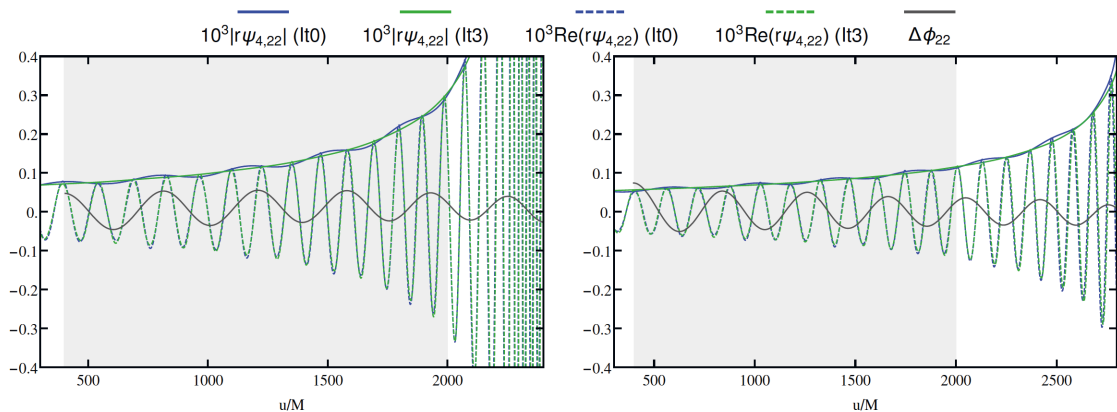


Figure 5.16: Comparison of the gravitational wave phasing of the evolutions of initial data without (It0, blue) and with (It3, green) eccentricity reduction for the SLy EoS (left) and H4 EoS (right) configuration. One can see the phase difference and the real part of the (2,2) mode of Ψ_4 , as well as its amplitude. The shaded region shows the region used for waveform alignment.

in congruence by shifting by constant time and phase offsets T, Φ according to

$$G(T, \Phi) = \int_{t_1}^{t_2} |\phi_1(t) - \phi_2(t + T) - \Phi|^2 dt. \quad (5.14)$$

Here $\phi_{1,2}$ denotes the GW phase of the two datasets, when we write the curvature scalar as $r\Psi_4 = a \exp(-i\phi)$. Note that Bernuzzi et al. [2015] present a more robust alignment procedure based on a frequency interval, which in principle could be employed as well. However the above procedure is sufficient for our purposes. Fig. 5.16 shows the results of our investigations, where we used green lines for the eccentricity reduced data and blue lines to denote the original data. The waveform is nicely aligned within the interval, which is illustrated as the shaded region. One can clearly see the reduced oscillations in the amplitude of the gravitational waveform. The circular data amplitude is oscillating around the eccentricity reduced data's amplitude with $\sim 5\%$ at early times $u \sim 400M$. Both simulations, SLy and H4, are looking qualitatively similar with the difference that the H4 setup has a later merger. We also provide the phase difference $\Delta\phi_{22}$, which oscillates between $[-0.06, 0.06]$ rad for both setups, where the amplitudes at early times are slightly larger for the H4 EoS.

Ultimately, these results demonstrate that the eccentricity reduction procedure — with roughly three iterations, corresponding to eccentricities of order $e_d \sim 10^{-4}$ — improves the waveform quality for GW modeling purposes, and should be employed in future precision studies of the gravitational waveform. On the other hand, we

have to note that eccentricity reduction is likely to be effective only if combined together with an improvement of other error sources, most notably truncation errors. Bernuzzi et al. [2015] showed that $\Delta\phi \sim 0.12$ rad is at least a factor two smaller than the typical uncertainty introduced by truncation errors at the resolutions employed here.

Irrotational binary inspiral

Although the focus of this thesis is squarely on initial data for neutron stars, we want to outline preliminary results of a related project, namely the usage of a Hamilton-Jacobi scheme for irrotational binary inspiral evolutions. The scheme has been developed by Markakis [2014] and we include it here, since considerable effort went into the first implementation of this scheme in a full general relativistic code and the considerations made within the derivation are similar to the equations we treated here. Furthermore, the BAM implementation we are striving for, would be particularly well-suited for evolutions of our initial data, which exclusively uses irrotational flows if computed with the BAM multigrid solver.

However, we have to stress that this is work in progress and the current implementation has led to several modifications of the scheme. We are thus only able to present preliminary results restricted to single TOV stars in this section, as there still exist open problems. Nevertheless, we do not want to leave this scheme and its implementation undiscussed, since it provides technical simplification and gain in efficiency and accuracy to binary inspiral problems, as explained in Markakis [2014], most notably the potential elimination of artificial atmospheres (compare Sec. 2.4.1).

6.1 Irrotational Hamilton-Jacobi hydrodynamics

We focused on the implementation of the irrotational Hamiltonian-Jacobi method and on overcoming the numerical challenges, hence we do not give the derivation here. Instead we refer to Markakis [2014] for details and briefly summarize the idea to gather the important equations. As in previous chapters, a simple barotropic fluid is considered. The starting point is the Euler-Lagrange equation of motion (Eq. (3) in [Markakis, 2014]) from which one can obtain the covariant Hamilton equation through Cartan's identity such that

$$\frac{d\pi_a}{dt} + \frac{\partial H}{\partial x^a} = \partial_t \pi_a + u^b (\nabla_b \pi_a - \nabla_a \pi_b) + \nabla_a H = 0. \quad (6.1)$$

Here we use the canonical fluid momentum π_i , which we already introduced earlier and the Hamiltonian of a fluid element is defined as

$$H = -hu_t = -\beta^j \pi_j + \alpha \sqrt{h^2 + \gamma^{ij} \pi_i \pi_j} = h \frac{\alpha - \beta^j \nu_j}{\sqrt{1 - \nu^2}}. \quad (6.2)$$

The fluid velocity as measured by normal observers is given by

$$\nu^i = \alpha^{-1}(v^i + \beta^i). \quad (6.3)$$

Following Markakis [2014], an important property stated in [Friedman and Stergioulas, 2013] can be exploited, i.e. binaries modeled as barotropic fluids without viscosity or dissipation exactly conserve circulation and thus if they are initially irrotational they remain irrotational. This enables us to assume the flows to be irrotational $\omega_{ab} = \nabla_b \pi_a - \nabla_a \pi_b = 0$, hence we can simplify (6.1) to become strictly flux conservative (meaning that it has no source terms)

$$\partial_t \pi_a + \nabla_a H = 0. \quad (6.4)$$

Further considering the conservation of rest-mass, the irrotational evolution scheme can be written in flux conservative form analogous to the Valencia formulation in Sec. 2.4.1. It thus reads

$$\partial_t \vec{U} + \partial_k F^k = 0, \quad (6.5)$$

where we can give the conservative variables \vec{U} and the flux vectors \vec{F}^k via

$$\vec{U} = \begin{pmatrix} \rho_* \\ \pi_i \end{pmatrix}, \quad \vec{F}^i = \begin{pmatrix} \rho_* v^i \\ \delta_j^i H \end{pmatrix}, \quad \text{for } i = 1, 2, 3 \quad (6.6)$$

and the i -th row of the vector is label with index i . Additionally, we employed the weighted rest mass density $\rho_* = \alpha \sqrt{\gamma} \rho u^t$, which is closely related to D as the only difference is the factor of the determinant. The conserved variables π_i are coupled with ρ_* via the equation of state $\rho = \rho(h)$ and the usual normalization condition $u_a u^a = -1$, thus

$$u^t = \alpha^{-1} \sqrt{\gamma^{ij} u_i u_j + 1}. \quad (6.7)$$

It is now possible to evolve (6.5) together with the spacetime metric. A nice feature of this formulation can be seen by looking at the construction of the primitive variables h, u_i from the conservative ones, which is necessary to compute the fluxes \vec{F}^i at each

time step. This reconstruction can be done by numerically solving

$$\rho(h) = \frac{\rho_* h}{\sqrt{\gamma} \sqrt{\gamma^{ij} \pi_i \pi_j + h^2}}, \quad (6.8)$$

which can be obtained through (6.7). One can notice that the reconstruction can solely be done by dividing by the specific enthalpy h instead of the rest-mass density. $h = 1$ in the exterior of the stars and thus no artificial atmosphere is needed for reconstruction. However, because strong hyperbolicity is lost for zero sound speed, a modification near the surface (not necessarily an atmosphere) is still needed for stability.

6.2 Preliminary numerical results

We implemented (6.5) in BAM and employed a Newton-Raphson scheme to iteratively solve (6.8) for reconstructing primitive from conservative variables. We compute the fluxes with a local Lax-Friedrich scheme and employed second order finite differencing for the test setups as well as a standard third order Runge-Kutta scheme for time evolutions. For our first runs, we still make use of an atmosphere and consider a simple polytropic equation of state with $\Gamma = 2$. The star is placed on a small grid with a fine grid size of $h = 0.25$. We then find that the evolution scheme encounters instabilities in the atmosphere caused by the vanishing sound speed. However, running in octant symmetry seems to minimize these effects and it is possible to run stable simulations for more than $1000M$. The left panel of Fig. 6.1 shows the results for a TOV star, which is oscillating in density over time due to the scheme. We clearly see that these oscillations are decreasing with second order as expected if we increase the resolution. For another test scenario, we made use of a similar setup, but now tried to drop the artificial atmosphere. Instead, we extrapolate the enthalpy h to the outer region of the stars, so that it is perfectly smooth and we modify the crust equation of state to be $\rho = \rho_{OC} h^{\lambda+1}$ with a density of the outer crust ρ_{OC} . Note that h is not used for solving the gravity part of the equations in the exterior and thus setting ρ to zero there to compute the sources of the gravity part does not introduce any errors.

We show the results of a full three dimensional evolution without any symmetries in the right panel of figure 6.1. We tested the stability of the scheme by adding a perturbation of the matter fields at around $x = -2.5$, $y = z = 0$ to the initial TOV data. We see the density profile (and all related profiles) settling down to a new stable solution after $10M$, while the snapshot in that figure shows the situation after $100M$. Unfortunately, the solution develops spikes in the velocities at the surface of the star

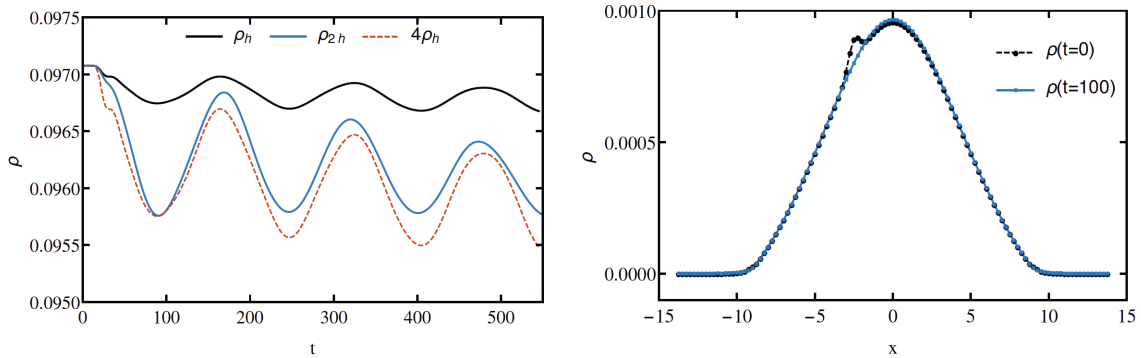


Figure 6.1: Shown are the central densities for two different setups. The left panel shows the oscillations of the density during the evolution with the irrotational scheme still including artificial atmosphere. The black line denotes twice the resolution of the blue line, while the red dashed line is the higher resolved run with appropriate scaling according to the expected second order convergence (note that actually the oscillations are rescaled and not the whole density).

In the right panel, the atmosphere is set to zero and the enthalpy is extrapolated to the outer region. We show the density profile with an initial perturbation in black and the solution settles down to a stable state, which is shown at $t = 100$ in blue.

and further instabilities are originating from the boundaries. These effects take over the dynamics after $\sim 200M$ and the solution becomes unstable. Again, at the surface zero sound speeds are encountered when $h = 1$ and then the characteristic eigenvalues become degenerate, instead of being distinct as for positive sound speeds. So, for polytropes instability arises for both Hamiltonian and Valencia formulation. For Valencia, an artificial atmosphere prevents instability at the expense of accuracy. In the Hamiltonian case, the same trick does not work. Instead, what does seem to work but has not yet been fully implemented is the following: Modify the crust EoS so that the sound speed remains finite and takes a constant realistic value ($\sim 0.05c$) in the crust. Also, extend h to values < 1 outside. This i) restores strong hyperbolicity and stability and ii) makes H and h smooth across the surface. Due to this smoothness, perturbations moving from the inside towards the outside cross the surface without amplification or reflection (which happens in Valencia with an atmosphere), and also numerical accuracy can be higher since smooth quantities are being numerically differentiated.

Currently we are investigating different EoSs in the crust and although this is work in progress, we hope that these techniques can circumvent the current problems.

Conclusion

7.1 Summary

Full general relativistic hydrodynamic simulations are needed to precisely study gravitational waves, ejecta or merger remnants of neutron stars with high accuracy. Binary neutron star mergers have been the center of studies of several works in recent years. A lot of progress has been made in this field by investigating topics such as different equations of state (e.g. Shibata et al. [2005]), neutron stars with spins [Bernuzzi et al., 2014] or large mass ratios [Taniguchi and Shibata, 2010]. However, there are still certain scenarios that could not yet be covered in a satisfactory manner. One of these is the topic of neutron stars which have not been circularized by gravitational wave radiation and which can probably be found in globular clusters through dynamical captures. In contrast to such highly eccentric orbits, simulations with low eccentricities have been studied in more detail, but are not entirely unproblematic, since usually undesired residual eccentricities of $e \sim 10^{-2}$ are inscribed to the initial data.

We have developed a method that is able to compute for the first time consistent initial data with eccentricities that cover the range from highly eccentric orbits down to eccentricity-reduced circular orbits. To do so, we have generalized the approximate helical Killing vector that is typically exploited to solve the Euler equation via its first integral to a pair of inscribed helical symmetry vectors. This generalization was then justified using two equivalent approaches. First, we added a boost to the standard approximate helical Killing vector used for constructing quasicircular initial data in order to vary the stars tangential velocities at apoapsis. Secondly, we showed that the same vectors can be constructed by inscribing circles to orbits approximated by ellipses. We further added a radial velocity component to that vector so that we are finally able to control the tangential and the radial velocity of the stars individually and construct arbitrary orbits, where the stars are initially located at apoapsis.

We wrote our own initial data solver and directly implemented it into the BAM code, which performs the evolutions. This code is based on a second order multigrid method and designed to run fast. Due to the simple Cartesian grid structure provided by BAM, we restrict to irrotational stars and approximate this fluid flow through a constant velocity potential. This approximation was tested and we presented results showing that it is a good approximation if the stars are sufficiently far apart. In our scheme, we distinguish between different frames of stationarity to track down the source of spurious oscillations found in evolutions of inconsistent, high eccentricity data. Our method reduces such oscillations by at least an order of magnitude for high resolutions if we assume stationarity in a rotating frame, while we observe the same spurious oscillations in case of stationarity in a comoving frame is assumed. Furthermore, we can confirm the physical character of the oscillations induced by tidal deformation at close encounters of the neutron stars, since these are qualitatively the same as found in other works with inconsistent data with unsolved constraints [Gold et al., 2012] or without solving Euler equation [East and Pretorius, 2012].

Another implementation has been carried out in order to upgrade the SGRID code and include our method. This code provides surface-fitted and compactified coordinates and solves the equation for the velocity potential and thus increases the accuracy of the data. Together with previous upgrades (described in Tichy [2012] or [Mol3]), SGRID is now able to compute neutron stars with arbitrary eccentricities in combination with more realistic piecewise polytropic EoS, generic spins and unequal mass ratios.

We were able to compute eccentricity reduced initial data for different equations of state, where we used an iterative method to determine eccentricity and radial velocity parameters, such that the resulting orbital eccentricity during evolutions is minimized. The eccentricity could be decreased by more than an order of magnitude within a few iterations, although each iteration is fairly time consuming. Evolutions with eccentricity reduced data were performed and showed clear differences in the waveforms amplitude and phase. However, the uncertainties are usually of comparable size so that other errors, e.g. truncation errors, have to be minimized in order to benefit from the improved data. If this can be achieved, low eccentric binaries have to be employed for gravitational wave analysis templates. As discussed in Read et al. [2013], the residual eccentricity in current simulations is large enough to bias the determination of the tidal deformation, which would provide a valuable constraint on the poorly-known equation of state of cold, dense nuclear matter.

Throughout the thesis, we provided several consistency checks of both implemen-

tations such as convergence checks or post-Newtonian estimates. It could be shown that our results are trustworthy and we also used different analytic estimates to define notions of eccentricity. Overall, the ability to construct self-consistent initial data for eccentric binary neutron stars allows us to study many interesting physical setups, in both the high- and low-eccentricity regimes.

Finally, we introduced a side-project in which we want to set up a new evolution scheme for irrotational binaries. This would be especially useful in our BAM initial data implementation, which uses irrotational flows and could thus evolve our initial data. The advantage of such a scheme is that it does not necessarily need an artificial atmosphere, which is employed by several other schemes. We showed first results of this work in progress and outlined the concept. Our preliminary results motivated a more detailed investigation in the future.

7.2 Future prospects

Now that we have two implementations capable of computing initial data for stars with arbitrary eccentricities, we are ready to explore the parameter space beyond our previous investigations. For highly accurate simulations it is appropriate to use SGRID's initial data, but especially for simulations with large eccentricities, we can use the extremely fast multigrid solver in BAM to find interesting orbits (e.g. with several encounters) and then compute more accurate data using the obtained parameters in SGRID. In [Mol4], we are investigating highly eccentric runs. We are considering a range of eccentric setups with and without spin and with different piecewise polytropic equations of state, as well as Γ_2 EoS. We plan to estimate the detectability of the waveforms and estimate the energy stored in the inter-burst oscillations and its effect on the orbit. Additionally, we hope to answer open questions about the final remnant of such eccentric scenarios, such as the properties of the accretion disc or one might also consider the ejecta.

Apart from these studies, there are several different things we can investigate with SGRID in the future. Most notably, we have not looked at the influence of eccentricity reduction on unequal mass stars and only have considered proof-of-principle tests for spinning stars.

Furthermore, there are also some possible upgrades that we would like to include in our scheme. On the one hand, we could tweak our schemes by considering PN corrections to the Newtonian expressions for the orbital motion which we used to

derive the symmetry vectors. Thus, we could try to obtain better comparisons with analytic techniques such as EOB formulations.

On the other hand, a general extension of our scheme to include black holes would not be complicated. Black hole-neutron star binaries would be an interesting feature of our initial data solvers and would yield the possibility to revisit previous setups (for instance from Stephens et al. [2011]) with consistent initial data.

The preliminary results we obtained from the Hamilton-Jacobi evolution scheme were promising and future work has to be done on this topic. We plan to implement an improved treatment of the neutron star crust in order to cure remaining instabilities. The next step is the application for binary neutron stars and a first simulation of stars on inspiralling or eccentric orbits.

Appendix

A Stationarity in a linearly comoving frame

Assuming we employ stationarity in a linearly comoving frame, i.e. setting $\omega = 0$ and $\lambda = v^y$, then this yields a Killing vector

$$k^a = t^a + v^y y^a \quad (\text{A.1})$$

and we would have an enthalpy profile determined by

$$(\partial_t + v^y \partial_y)h = 0. \quad (\text{A.2})$$

However, we can consider the limit of circular orbits, where $v_{1,2}^y = \Omega x_{1,2}$ and in which case the enthalpy profile has to exactly satisfy

$$(\partial_t + \omega \partial_\phi)h = 0. \quad (\text{A.3})$$

From (A.3), we obtain that $\partial_t h = -\Omega \partial_\phi h$, which can be inserted into (A.2) to get

$$(\partial_t + v^y \partial_y)h = (-\Omega \partial_\phi + v^y \partial_y)h \quad (\text{A.4})$$

$$= \Omega [(x_{1,2} - x) \partial_y + y \partial_x] h \quad (\text{A.5})$$

for each star 1, 2. Obviously, this only vanishes at the star's center at $x = x_{1,2}, y = 0$, but nowhere else. This leads to unphysical behavior in the most parts of the stars interiors.

Furthermore, using the injection energy to construct the force balance equation (similar to (3.42)), we obtain violations of true force balance at the stars center if we employ (A.1) for this construction, due to the missing centrifugal forces. Thus the gravitational forces are unbalanced and explain the the oscillations of $\sim 20\%$ in Figure 5.4.

B Nonrelativistic incompressible binaries

In the following, we are investigating the injection energy and the velocity potential in the limit of nonrelativistic incompressible flows based on calculations done in [Mol1]. These investigations are particularly useful for fixing parameters in the physical approach to the symmetry vector, since we thus ensure the correct limits. Following equation (6.49) from Gourgoulhon [2006], we can write the Crocco form of the Euler equation as

$$\partial_t v_i + v^j (\bar{D}_j v_i - \bar{D}_i v_j) = -\bar{D}_i H. \quad (\text{B.6})$$

where $H = \frac{1}{2}v^2 + h_N + \Phi$ is the Hamiltonian of a fluid element with specific enthalpy h_N , while $v^i = dx^i/dt$ is its velocity, Φ is the gravitational potential, and \bar{D}_i is the covariant derivative compatible with the Euclidian 3-metric f_{ij} in \mathbb{E}^3 . For irrotational flows, the second term on the right hand side of Eq. (B.6) vanishes and we can write it as

$$\partial_t \Psi = -H, \quad (\text{B.7})$$

where Ψ is the potential $\bar{D}_i \psi = v_i$. Employing the specific enthalpy for incompressible flows $h_N = \int dp/\rho = p/\rho$, where the mass density ρ is constant, the continuity equation

$$\partial_t \rho + \bar{D}_a (\rho v^a) = 0 \quad (\text{B.8})$$

simplifies to a Laplace equation for the velocity potential,

$$\bar{D}_a \bar{D}^a \Psi = 0. \quad (\text{B.9})$$

Instead of considering such systems for evolutions as done in chapter 6, we now want to focus on initial data by finding analytic solutions to Eqs. (B.7) and (B.9) for binaries on circular and eccentric orbits.

Circular orbits

We describe the location of the star by the position of its center relative to the origin (which we assume to be the center of mass) with

$$\vec{R}(t) = R \cos \Omega t \vec{x}_1 + R \sin \Omega t \vec{y}_1, \quad (\text{B.10})$$

where $x_{\mathbb{1}}$ denotes the unit vector in x -direction. We can thus write the fluid velocity as

$$\vec{v}(t) = \dot{\vec{R}} = -\Omega R(\sin \Omega t \vec{x}_{\mathbb{1}} - \cos \Omega t \vec{y}_{\mathbb{1}}) = \vec{\nabla} \Psi. \quad (\text{B.11})$$

For irrotational incompressible binaries on circular orbits, all fluid elements move on circles with different centers, but with the same radius R , and with the same speed $v = \Omega R$. Then, Eqs. (B.7) and (B.9) have the exact solution ¹

$$\Psi(t, \vec{r}) = -\mathcal{E}t + \vec{v}(t) \cdot \vec{r} = -\mathcal{E}t - \Omega R(x \sin \Omega t - y \cos \Omega t). \quad (\text{B.12})$$

The injection energy \mathcal{E} is constant throughout the star in space and time [Friedman and Stergioulas, 2013]. Besides the Euler equation, the solution (B.12) satisfies the incompressibility condition

$$\nabla v = \nabla^2 \Psi = 0, \quad (\text{B.13})$$

which follows from the continuity equation for constant density. Thus, this solution is exact for irrotational incompressible stars on circular orbits. It is straightforward to check that the velocity potential (B.12) satisfies a Hamilton-Jacobi equation in a rotating frame

$$(\partial_t \Omega \partial_\phi) \Psi + \mathcal{E} = 0. \quad (\text{B.14})$$

This is a first integral of the equation

$$(\partial_t + \Omega \mathcal{L}_{\vec{\varphi}}) v_a = 0, \quad (\text{B.15})$$

which follows from helical symmetry, i.e., stationarity in a rotating frame. The conserved injection energy is obtained from Eqs. (B.7) and (B.14) and given by

$$\mathcal{E} = H - \Omega(xv_y - yv_x). \quad (\text{B.16})$$

Taking the gradient of this equation and evaluating at the center of the star $(R, 0, 0)$ at $t = 0$ gives a force balance equation

$$\partial_x \mathcal{E}|_{x=R} = \partial_x \Phi|_{x=R} - \Omega^2 R = 0, \quad (\text{B.17})$$

which yields Kepler's third law for inverse square forces.

¹Note that $\vec{\nabla}$ is the index-free version of \bar{D}_a

Eccentric orbits

Now the derivation is generalized to eccentric binary systems, for which the position of the stellar center can be expressed as

$$\vec{R}(t) = [a \cos \zeta(t) + ae] \vec{x}_1 + b \sin \zeta(t) \vec{y}_1, \quad (\text{B.18})$$

The eccentric anomaly $\zeta(t)$ is related to the mean anomaly $\bar{\Omega}t$ via the Kepler equation

$$\bar{\Omega}t = \zeta(t) + e \sin \zeta(t), \quad (\text{B.19})$$

where $e = \sqrt{1 - b^2/a^2}$ is the eccentricity with semi-major axis a and semi-minor axis b , and $\bar{\Omega} = 2\pi/T$ is the mean motion for a orbital period T . Furthermore, we employ an extreme mass ratio and thus study an effectively one body problem, where the massive star is at the origin (which is the center of mass) and is chosen to be the left focus of the ellipse. This assumption is made for simplicity, but can straightforwardly be relaxed to recover the two body equations as we point out in the end. Using e.g. Mathematica, we compute a series solution to Kepler equation (B.19) and find

$$\zeta(t) = \frac{\bar{\Omega}t}{e+1} + \frac{(\bar{\Omega}t)^3 e}{6(e+1)^4} + \mathcal{O}(t^5), \quad (\text{B.20})$$

where we assumed that the values $\zeta = 0$ and $\zeta = \pi$ correspond to apoapsis and periapsis, respectively. The fluid velocity is homogeneous and given by

$$\vec{v}(t) = \vec{\dot{R}} = -\dot{\zeta}(t)[a \sin \zeta(t) \vec{\hat{x}} - b \cos \zeta(t) \vec{\hat{y}}] = \vec{\nabla} \Psi \quad (\text{B.21})$$

and the velocity potential is given by

$$\begin{aligned} \Psi(t, \vec{r}) &= -\mathcal{E}t + \vec{v}(t) \cdot \vec{r} \\ &= -\mathcal{E}t - \dot{\zeta}(t)[ax \sin \zeta(t) - by \cos \zeta(t)]. \end{aligned} \quad (\text{B.22})$$

Introducing the quantity

$$\varpi(t) = \dot{\zeta}(t) = \frac{\bar{\Omega}}{e+1} + \mathcal{O}(t^2) \quad (\text{B.23})$$

allows us to write

$$\vec{\ddot{R}} = \vec{\dot{\varpi}} \times \vec{R} - \varpi^2 \vec{R} = \frac{\dot{\varpi}}{\varpi} \vec{\dot{R}} - \varpi^2 \vec{R} \quad (\text{B.24})$$

and thus

$$\partial_t \Psi = -\mathcal{E} + \ddot{\vec{R}} \cdot \vec{x} = -\mathcal{E} - \varpi^2 [a x \sin \zeta(t) + b y \cos \zeta(t)] + \frac{\dot{\varpi}}{\varpi} \dot{\vec{R}} \cdot \vec{x} \quad (\text{B.25})$$

If we operate on (B.22) with $\partial_t + k^i \partial_i = \partial_t + \omega \partial_\varphi + \lambda \partial_y$, where k^i is the spatial part of our inscribed helical symmetry vector (3.31a), and demand that the resulting expression be constant throughout the star at $t = 0$, i.e., $\vec{\nabla} \mathcal{E} = 0$. This yields

$$v = (1 - e^2) \omega a \quad (\text{B.26})$$

with ω given by Eq. (3.32). In order to obtain Eq. (3.33), we have to assume additionally that $k^i = v y^i$ at the star center $x = a(1 + e)$ at $t = 0$.

At this point it is straightforward to check that the force balance equation

$$\partial_x \mathcal{E}|_{x=a(1+e)} = 0 \quad (\text{B.27})$$

applied to the star center yields Kepler's third law $\Omega^2 = GM/a^3$.

In order to recover the two-body equations one can rescale the ellipse by a factor depending on the mass of each companion, as indicated by Eq. (3.30). Then, Eq. (B.26) is replaced by Eqs. (3.34), while e , ω , and $\bar{\Omega}$ remain unchanged.

C Publications

- [Mol1] **N. Moldenhauer**, C. Markakis, N. K. Johnson-McDaniel, W. Tichy, B. Brügmann (2014) *Initial data for binary neutron stars with adjustable eccentricity*, Phys.Rev.D.90 084043, arXiv:1408.4136[gr-qc].
- [Mol2] B. Brügmann, S. Bernuzzi, T. Dietrich, D. Hilditch, N. K. Johnson-McDaniel, **N. Moldenhauer**, M. Ujevic, and A. Weyhausen, *Dynamics of binary neutron star systems*, in S. Wagner, A. Bode, H. Satzger, M. Brehm (Eds.), High Performance Computing in Science and Engineering Garching/Munich 2014, ISBN: 978-3-9816675-0-9.
- [Mol3] T. Dietrich, **N. Moldenhauer**, N. K. Johnson-McDaniel, C. Markakis, S. Bernuzzi, W. Tichy, B. Brügmann (2015), *Binary Neutron Stars with generic Spin, Eccentricity, Mass ratio and Compactness - Quasi-equilibrium sequences and first evolutions* arXiv:1507.07100[gr-qc].
- [Mol4] **N. Moldenhauer**, N. K. Johnson-McDaniel, C. Markakis, B. Brügmann (2016), *Evolutions of highly eccentric Neutron stars* In preparation.

D List of presentations

- 16.10.2012 SFB/TR7 Semiannual Meeting (Garching): Initial Data for Neutron Star Binaries
- 27.02.2013 DPG Spring Meeting (Jena): Eccentric Binary Neutron Star Initial Data
- 12.07.2013 GR20/Amaldi 10 (Warsaw): Initial Data for Neutron Star Binaries, poster presentation
- 04.09.2013 International Conference on Mathematical Modeling in Physical Sciences (Prague): Eccentric Binary Neutron Star Initial Data
- 24.02.2014 Annual Meeting GRK (Oppurg): Eccentric Binary Neutron Star Initial Data
- 20.03.2014 DPG Spring Meeting (Berlin): Eccentric Binary Neutron Star Initial Data
- 04.12.2014 SFB/TR7 Conclusion Workshop (Jena): Initial Data for Neutron Star Binaries with Adjustable Eccentricity
- 19.03.2015 DPG Spring Meeting (Berlin): Initial Data for Neutron Star Binaries with Adjustable Eccentricity
- 02.03.2015 RTG Networking Workshop (Bremen): Initial Data for Neutron Star Binaries with Adjustable Eccentricity
- 25.06.2015 Tag der Forschung (Jena): Numerical Relativity, poster presentation

Bibliography

- Miguel Alcubierre. *Introduction to 3+1 Numerical Relativity*. Oxford University Press, Oxford, 2008.
- Daniela Alic, Wolfgang Kastaun, and Luciano Rezzolla. Constraint damping of the conformal and covariant formulation of the Z4 system in simulations of binary neutron stars. *Phys. Rev.*, D88(6):064049, 2013. doi: 10.1103/PhysRevD.88.064049.
- N. Andersson and G.L. Comer. Relativistic fluid dynamics: Physics for many different scales. *Living Rev. Relativity*, 10:1, 2007. doi: 10.12942/lrr-2007-1.
- Marcus Ansorg. Multi-Domain Spectral Method for Initial Data of Arbitrary Binaries in General Relativity. *Classical Quantum Gravity*, 24:S1–S14, 2007. doi: 10.1088/0264-9381/24/12/S01.
- J. M. Antognini, B. J. Shappee, T. A. Thompson, and P. Amaro-Seoane. Rapid eccentricity oscillations and the mergers of compact objects in hierarchical triples. *Mon. Not. R. Astron. Soc.*, 439:1079–1091, March 2014. doi: 10.1093/mnras/stu039.
- F. Antonini and H. B. Perets. Secular Evolution of Compact Binaries near Massive Black Holes: Gravitational Wave Sources and Other Exotica. *Astrophys. J.*, 757:27, September 2012. doi: 10.1088/0004-637X/757/1/27.
- R. Arnowitt, S. Deser, and Charles W. Misner. The dynamics of general relativity. In L. Witten, editor, *Gravitation: An Introduction to Current Research*, pages 227–265. Wiley, New York, 1962.
- John G. Baker, James R. van Meter, Sean T. McWilliams, Joan Centrella, and Bernard J. Kelly. Consistency of post-Newtonian waveforms with numerical relativity. *Phys. Rev. Lett.*, 99:181101, 2007. doi: 10.1103/PhysRevLett.99.181101.
- Thomas W. Baumgarte and Stuart L. Shapiro. *Numerical Relativity: Solving Einstein's Equations on the Computer*. Cambridge University Press, Cambridge, 2010.

- Sebastiano Bernuzzi and David Hilditch. Constraint violation in free evolution schemes: comparing BSSNOK with a conformal decomposition of Z4. *Phys. Rev. D*, 81:084003, 2010. doi: 10.1103/PhysRevD.81.084003.
- Sebastiano Bernuzzi, Alessandro Nagar, Marcus Thierfelder, and Bernd Brügmann. Tidal effects in binary neutron star coalescence. *Phys. Rev. D*, 86:044030, 2012a. doi: 10.1103/PhysRevD.86.044030.
- Sebastiano Bernuzzi, Marcus Thierfelder, and Bernd Brügmann. Accuracy of numerical relativity waveforms from binary neutron star mergers and their comparison with post-Newtonian waveforms. *Phys. Rev. D*, 85:104030, 2012b. doi: 10.1103/PhysRevD.85.104030.
- Sebastiano Bernuzzi, Tim Dietrich, Wolfgang Tichy, and Bernd Brügmann. Mergers of binary neutron stars with realistic spin. *Phys. Rev. D*, 89:104021, 2014. doi: 10.1103/PhysRevD.89.104021.
- Sebastiano Bernuzzi, Alessandro Nagar, Tim Dietrich, and Thibault Damour. Modeling the dynamics of tidally-interacting binary neutron stars up to merger. *Phys. Rev. Lett.*, 114(16):161103, 2015. doi: 10.1103/PhysRevLett.114.161103.
- Luc Blanchet. Gravitational Radiation from Post-Newtonian Sources and Inspiralling Compact Binaries. *Living Rev. Relativity*, 17:2, 2014. doi: 10.12942/lrr-2014-2.
- S. Bonazzola, E. Gourgoulhon, and J.-A. Marck. Numerical models of irrotational binary neutron stars in general relativity. *Phys. Rev. Lett.*, 82:892, 1999. doi: 10.1103/PhysRevLett.82.892.
- Achi Brandt. Multi-level adaptive solutions to boundary-value problems. *Math. Comp.*, 31: 333–390, 1977.
- William L. Briggs, Van Emden Henson, and Steve F. McCormick. *A Multigrid Tutorial*. SIAM Press, Philadelphia, 2nd edition, 2000. ISBN 0-89871-462-1.
- Bernd Brügmann, José A. González, Mark Hannam, Sascha Husa, Ulrich Sperhake, and Wolfgang Tichy. Calibration of Moving Puncture Simulations. *Phys. Rev. D*, 77:024027, 2008. doi: 10.1103/PhysRevD.77.024027.
- Alessandra Buonanno, Lawrence E. Kidder, Abdul H. Mroué, Harald P. Pfeiffer, and Andrea Taracchini. Reducing orbital eccentricity of precessing black-hole binaries. *Phys. Rev. D*, 83:104034, 2011. doi: 10.1103/PhysRevD.83.104034.
- B. Carter. Cambridge University Press, Cambridge, England, 1979.

- Timothy A. Davis. UMFPACK: A set of routines for solving sparse linear systems via LU factorization, a. URL <http://www.cise.ufl.edu/research/sparse/umfpack/>. UMF-PACK.
- Timothy A. Davis. UMFPACK: A set of routines for solving sparse linear systems via LU factorization, b. URL <http://www.cise.ufl.edu/research/sparse/umfpack/>. <http://www.cise.ufl.edu/research/sparse/umfpack/>.
- M. Dominik, E. Berti, R. O’Shaughnessy, I. Mandel, K. Belczynski, C. Fryer, D. E. Holz, T. Bulik, and F. Pannarale. Double Compact Objects III: Gravitational Wave Detection Rates. *Astrophys. J.*, 806(2):263, 2015. doi: 10.1088/0004-637X/806/2/263.
- Michal Dominik, Krzysztof Belczynski, Christopher Fryer, Daniel E. Holz, Emanuele Berti, Tomasz Bulik, Ilya Mandel, and Richard O’Shaughnessy. Double Compact Objects I: The Significance of the Common Envelope on Merger Rates. *Astrophys. J.*, 759:52, 2012. doi: 10.1088/0004-637X/759/1/52.
- Matthew D. Duez, Pedro Marronetti, Stuart L. Shapiro, and Thomas W. Baumgarte. Hydrodynamic simulations in 3+1 general relativity. *Phys. Rev. D*, 67:024004, 2003.
- William E. East and Frans Pretorius. Dynamical Capture Binary Neutron Star Mergers. *Astrophys. J. Lett.*, 760:L4, 2012. doi: 10.1088/2041-8205/760/1/L4.
- William E. East, Frans Pretorius, and Branson C. Stephens. Eccentric black hole-neutron star mergers: effects of black hole spin and equation of state. *Phys. Rev. D*, 85:124009, 2012a. doi: 10.1103/PhysRevD.85.124009.
- William E. East, Fethi M. Ramazanoğlu, and Frans Pretorius. Conformal Thin-Sandwich Solver for Generic Initial Data. *Phys. Rev. D*, 86:104053, 2012b. doi: 10.1103/PhysRevD.86.104053.
- William E. East, Sean T. McWilliams, Janna Levin, and Frans Pretorius. Observing complete gravitational wave signals from dynamical capture binaries. *Phys. Rev. D*, 87(4):043004, 2013. doi: 10.1103/PhysRevD.87.043004.
- D. Eichler, M. Livio, T. Piran, and D. N. Schramm. Nucleosynthesis, neutrino bursts and gamma-rays from coalescing neutron stars. *Nature*, 340:126, 1989. doi: 10.1038/340126a0.
- Joshua A. Faber and Frederic A. Rasio. Binary neutron star mergers. *Living Rev. Relativity*, 15:8, 2012. doi: 10.12942/lrr-2012-8. URL <http://www.livingreviews.org/lrr-2012-8>.
- Francois Foucart, Lawrence E. Kidder, Harald P. Pfeiffer, and Saul A. Teukolsky. Initial data for black hole-neutron star binaries: A flexible, high-accuracy spectral method. *Phys. Rev. D*, 77:124051, 2008. doi: 10.1103/PhysRevD.77.124051.

- John L. Friedman and Nikolaos Stergioulas. *Rotating Relativistic Stars*. Cambridge University Press, New York, NY, 2013. ISBN 978-0-521-87254-6.
- Pablo Galaviz, Bernd Brügmann, and Zhoujian Cao. Numerical evolution of multiple black holes with accurate initial data. *Phys. Rev. D*, 82:024005, 2010. doi: 10.1103/PhysRevD.82.024005.
- Bryant Garcia, Geoffrey Lovelace, Lawrence E. Kidder, Michael Boyle, Saul A. Teukolsky, Mark A. Scheel, and Bela Szilagy. Are different approaches to constructing initial data for binary black hole simulations of the same astrophysical situation equivalent? *Phys. Rev. D*, 86:084054, 2012. doi: 10.1103/PhysRevD.86.084054.
- Roman Gold and Bernd Brügmann. Radiation from low-momentum zoom-whirl orbits. *Classical Quantum Gravity*, 27:084035, 2010. doi: 10.1088/0264-9381/27/8/084035.
- Roman Gold and Bernd Brügmann. Eccentric black hole mergers and zoom-whirl behavior from elliptic inspirals to hyperbolic encounters. *Phys. Rev. D*, 88:064051, 2013. doi: 10.1103/PhysRevD.88.064051.
- Roman Gold, Sebastiano Bernuzzi, Marcus Thierfelder, Bernd Brügmann, and Frans Pretorius. Eccentric binary neutron star mergers. *Phys. Rev. D*, 86:121501(R), 2012. doi: 10.1103/PhysRevD.86.121501.
- E. Gourgoulhon. Relations between three formalisms for irrotational binary neutron stars in general relativity. 1998.
- Eric Gourgoulhon. An Introduction to relativistic hydrodynamics. *EAS Publ. Ser.*, 21:43, 2006. doi: 10.1051/eas:2006106.
- Eric Gourgoulhon, Philippe Grandclément, Jean-Alain Marck, Jérôme Novak, and Keisuke Taniguchi. <http://www.lorene.obspm.fr>.
- David Hilditch, Sebastiano Bernuzzi, Marcus Thierfelder, Zhoujian Cao, Wolfgang Tichy, and Bernd Brügmann. Compact binary evolutions with the Z4c formulation. *Phys. Rev. D*, 88:084057, 2013. doi: 10.1103/PhysRevD.88.084057.
- Sascha Husa, Mark Hannam, José A. González, Ulrich Sperhake, and Bernd Brügmann. Reducing eccentricity in black-hole binary evolutions with initial parameters from post-Newtonian inspiral. *Phys. Rev. D*, 77:044037, 2008. doi: 10.1103/PhysRevD.77.044037.
- James A. Isenberg. Waveless approximation theories of gravity. *Int. J. Mod. Phys. D*, 17: 265–273, 2008. doi: 10.1142/S0218271808011997.

- Nathan K. Johnson-McDaniel, Nicolas Yunes, Wolfgang Tichy, and Benjamin J. Owen. Conformally curved binary black hole initial data including tidal deformations and outgoing radiation. *Phys. Rev. D*, 80:124039, 2009. doi: 10.1103/PhysRevD.80.124039.
- I. Kowalska, T. Bulik, K. Belczynski, M. Dominik, and D. Gondek-Rosinska. The eccentricity distribution of compact binaries. *Astron. Astrophys.*, 527:A70, March 2011. doi: 10.1051/0004-6361/201015777.
- K. Kyutoku and N. Seto. Pre-merger localization of eccentric compact binary coalescences with second-generation gravitational-wave detector networks. *Mon. Not. R. Astron. Soc.*, 441:1934–1942, July 2014. doi: 10.1093/mnras/stu698.
- Koutarou Kyutoku, Masaru Shibata, and Keisuke Taniguchi. Reducing orbital eccentricity in initial data of binary neutron stars. *Phys. Rev. D*, 90:064006, 2014. doi: 10.1103/PhysRevD.90.064006.
- J. M. Lattimer and M. Prakash. Neutron star structure and the equation of state. *Astrophys. J.*, 550:426–442, 2001. doi: 10.1086/319702.
- James M. Lattimer. The nuclear equation of state and neutron star masses. *Ann. Rev. Nucl. Part. Sci.*, 62:485–515, 2012. doi: 10.1146/annurev-nucl-102711-095018.
- H. K. Lau, P. T. Leung, and L. M. Lin. Inferring physical parameters of compact stars from their f-mode gravitational wave signals. *Astrophys. J.*, 714:1234–1238, 2010. doi: 10.1088/0004-637X/714/2/1234.
- William H. Lee, Enrico Ramirez-Ruiz, and Glenn van de Ven. Short gamma-ray bursts from dynamically-assembled compact binaries in globular clusters: pathways, rates, hydrodynamics and cosmological setting. *Astrophys. J.*, 720:953–975, 2010. doi: 10.1088/0004-637X/720/1/953.
- A. Lichnerowicz. Sur l’invariant intégral de l’hydrodynamique relativiste. *Ann. Scient. École Norm. Sup.*, 58:285, 1941. URL http://www.numdam.org/item?id=ASENS_1941_3_58__285_0.
- A. Lichnerowicz. L’intégration des équations de la gravitation relativiste et le problème des n corps. *J. Math. Pures et Appl.*, 23:37–63, 1944.
- A. Lichnerowicz. *Relativistic Hydrodynamics and Magnetohydrodynamics*. Benjamin, New York, 1967.
- Nicholas Loutrel, Nicolas Yunes, and Frans Pretorius. A Parametrized post-Einsteinian Framework for Gravitational Wave Bursts. 2014.

- Charalampos M. Markakis. Hamiltonian Hydrodynamics and Irrotational Binary Inspiral. 2014.
- J. M. Martí, J. M. Ibáñez, and J. M. Miralles. Numerical relativistic hydrodynamics: Local characteristic approach. *Phys. Rev. D*, 43:3794, 1991.
- Raoul-Martin Memmesheimer, Achamveedu Gopakumar, and Gerhard Schäfer. Third post-Newtonian accurate generalized quasi-Keplerian parametrization for compact binaries in eccentric orbits. *Phys. Rev. D*, 70:104011, 2004. doi: 10.1103/PhysRevD.70.104011.
- Niclas Moldenhauer. Initial data for neutron star binaries, 2012. Master Thesis, University of Jena.
- Thierry Mora and Clifford M. Will. A post-Newtonian diagnostic of quasi-equilibrium binary configurations of compact objects. *Phys. Rev. D*, 69:104021, 2004. doi: 10.1103/PhysRevD.69.104021.
- Abdul H. Mroué and Harald P. Pfeiffer. Precessing Binary Black Holes Simulations: Quasicircular Initial Data. 2012.
- Smadar Naoz, Bence Kocsis, Abraham Loeb, and Nicolas Yunes. Resonant Post-Newtonian Eccentricity Excitation in Hierarchical Three-body Systems. *Astrophys. J.*, 773:187, 2013. doi: 10.1088/0004-637X/773/2/187.
- Ryan M. O’Leary, Bence Kocsis, and Abraham Loeb. Gravitational waves from scattering of stellar-mass black holes in galactic nuclei. *Mon. Not. R. Astron. Soc.*, 395(4):2127–2146, 2009. doi: 10.1111/j.1365-2966.2009.14653.x.
- N. Ó Murchadha and J. W. York. Gravitational energy. *Phys. Rev. D*, 10(8):2345–2357, 1974. doi: 10.1103/PhysRevD.10.2345.
- J. R. Oppenheimer and G. M. Volkoff. On Massive Neutron Cores. *Phys. Rev.*, 55:374–381, 1939. doi: 10.1103/PhysRev.55.374.
- P. C. Peters. Gravitational radiation and the motion of two point masses. *Phys. Rev.*, 136: B1224–B1232, 1964. doi: 10.1103/PhysRev.136.B1224.
- Harald P. Pfeiffer, D. A. Brown, L. E. Kidder, L. Lindblom, G. Lovelace, and M. Scheel. Reducing orbital eccentricity in binary black hole simulations. *Classical Quantum Gravity*, 24:S59–S82, 2007. doi: 10.1088/0264-9381/24/12/S06.
- Konstantin Postnov and Lev Yungelson. The Evolution of Compact Binary Star Systems. *Living Rev. Relativity*, 17:3, 2014. doi: 10.12942/lrr-2014-3.

- William H. Press, Saul A. Teukolsky, William T. Vetterling, and Brian P. Flannery. *Numerical Recipes: The Art of Scientific Computing*. Cambridge University Press, New York, NY, 3 edition, 2007.
- Richard H. Price, Charalampos Markakis, and John L. Friedman. Iteration Stability for Simple Newtonian Stellar Systems. *J. Math. Phys.*, 50:073505, 2009. doi: 10.1063/1.3166136.
- Michael Pürrer, Sascha Husa, and Mark Hannam. An efficient iterative method to reduce eccentricity in numerical-relativity simulations of compact binary inspiral. *Phys. Rev. D*, 85:124051, 2012. doi: 10.1103/PhysRevD.85.124051.
- J. S. Read, C. Markakis, M. Shibata, K. Uryū, J. D. E. Creighton, and J. L. Friedman. Measuring the neutron star equation of state with gravitational wave observations. *Phys. Rev. D*, 79:124033, 2009a. doi: 10.1103/PhysRevD.79.124033.
- Jocelyn S. Read, Benjamin D. Lackey, Benjamin J. Owen, and John L. Friedman. Constraints on a phenomenologically parameterized neutron-star equation of state. *Phys. Rev. D*, 79:124032, 2009b. doi: 10.1103/PhysRevD.79.124032.
- Jocelyn S. Read, Luca Baiotti, Jolien D. E. Creighton, John L. Friedman, Bruno Giacomazzo, Koutarou Kyutoku, Charalampos Markakis, Luciano Rezzolla, Masaru Shibata, and Keisuke Taniguchi. Matter effects on binary neutron star waveforms. *Phys. Rev. D*, 88:044042, 2013. doi: 10.1103/PhysRevD.88.044042.
- Luciano Rezzolla and Olindo Zanotti. *Relativistic hydrodynamics*. Oxford University Press, 2013.
- R. Rieth and Gerhard Schäfer. Comment on a relativistic model for coalescing neutron star binaries. 1996.
- C. Ronchi, R. Iacono, and P.S. Paolucci. The âcubed sphereâ: A new method for the solution of partial differential equations in spherical geometry. *J. Comput. Phys.*, 124(1): 93 – 114, 1996.
- S. Rosswog, T. Piran, and E. Nakar. The multi-messenger picture of compact object encounters: binary mergers versus dynamical collisions. *Mon. Not. R. Astron. Soc.*, 430: 2585, 2013. doi: 10.1093/mnras/sts708.
- Johan Samsing, Morgan MacLeod, and Enrico Ramirez-Ruiz. The Formation of Eccentric Compact Binary Inspirals and the Role of Gravitational Wave Emission in Binary-Single Stellar Encounters. *Astrophys. J.*, 784:71, 2014. doi: 10.1088/0004-637X/784/1/71.

- Naoki Seto. Highly Eccentric Kozai Mechanism and Gravitational-Wave Observation for Neutron Star Binaries. *Phys. Rev. Lett.*, 111:061106, 2013. doi: 10.1103/PhysRevLett.111.061106.
- Masaru Shibata. A relativistic formalism for computation of irrotational binary stars in quasi equilibrium states. *Phys. Rev. D*, 58:024012, 1998. doi: 10.1103/PhysRevD.58.024012.
- Masaru Shibata, Keisuke Taniguchi, and Kōji Uryū. Merger of binary neutron stars with realistic equations of state in full general relativity. *Phys. Rev. D*, 71:084021, 2005.
- U. Sperhake, E. Berti, V. Cardoso, J. A. González, B. Brügmann, and M. Ansorg. Eccentric binary black-hole mergers: The transition from inspiral to plunge in general relativity. *Phys. Rev. D*, 78:064069, 2008. doi: 10.1103/PhysRevD.78.064069.
- Branson C. Stephens, William E. East, and Frans Pretorius. Eccentric Black Hole-Neutron Star Mergers. *Astrophys. J. Lett.*, 737:L5, 2011. doi: 10.1088/2041-8205/737/1/L5.
- Kai Sheng Tai, Sean T. McWilliams, and Frans Pretorius. Detecting gravitational waves from highly eccentric compact binaries. 2014.
- K. Taniguchi and E. Gourgoulhon. *Phys. Rev. D*, 65:44027, 2002.
- Keisuke Taniguchi and Masaru Shibata. Binary Neutron Stars in Quasi-equilibrium. *Astrophys. J. Suppl. Ser.*, 188:187, 2010. doi: 10.1088/0067-0049/188/1/187.
- S. A. Teukolsky. Irrotational binary neutron stars in quasi-equilibrium in general relativity. *Astrophys. J.*, 504:442–449, 1998. doi: 10.1086/306082.
- Marcus Thierfelder, Sebastiano Bernuzzi, and Bernd Brügmann. Numerical relativity simulations of binary neutron stars. *Phys. Rev. D*, 84:044012, 2011. doi: 10.1103/PhysRevD.84.044012.
- Jonathan Thornburg. Black hole excision with multiple grid patches. *Classical Quantum Gravity*, 21(15):3665–3691, 7 August 2004.
- Wolfgang Tichy. Long term black hole evolution with the BSSN system by pseudo-spectral methods. *Phys. Rev. D*, 80:104034, 2009a. doi: 10.1103/PhysRevD.80.104034.
- Wolfgang Tichy. A new numerical method to construct binary neutron star initial data. *Classical Quantum Gravity*, 26:175018, 2009b. doi: 10.1088/0264-9381/26/17/175018.
- Wolfgang Tichy. Initial data for binary neutron stars with arbitrary spins. *Phys. Rev. D*, 84:024041, 2011. doi: 10.1103/PhysRevD.84.024041.

- Wolfgang Tichy. Constructing quasi-equilibrium initial data for binary neutron stars with arbitrary spins. *Phys. Rev. D*, 86:064024, 2012. doi: 10.1103/PhysRevD.86.064024.
- Wolfgang Tichy and Pedro Marronetti. A Simple method to set up low eccentricity initial data for moving puncture simulations. *Phys. Rev. D*, 83:024012, 2011. doi: 10.1103/PhysRevD.83.024012.
- R. C. Tolman. Static Solutions of Einstein's Field Equations for Spheres of Fluid. *Phys. Rev.*, 55:364–373, 1939. doi: 10.1103/PhysRev.55.364.
- David Tsang. Shattering Flares During Close Encounters of Neutron Stars. *Astrophys. J.*, 777:103, 2013. doi: 10.1088/0004-637X/777/2/103.
- Petr Tsatsin and Pedro Marronetti. Initial data for neutron star binaries with arbitrary spins. *Phys. Rev. D*, 88(6):064060, 2013. doi: 10.1103/PhysRevD.88.064060.
- Antonios Tsokaros, Kōji Uryū, and Luciano Rezzolla. A new code for quasi-equilibrium initial data of binary neutron stars: corotating, irrotational and slowly spinning systems. *Phys. Rev. D*, 91(10):104030, 2015. doi: 10.1103/PhysRevD.91.104030.
- Koji Uryū, Francois Limousin, John L. Friedman, Eric Gourgoulhon, and Masaru Shibata. Binary neutron stars in a waveless approximation. *Phys. Rev. Lett.*, 97:171101, 2006. doi: 10.1103/PhysRevLett.97.171101.
- Koji Uryū, Francois Limousin, John L. Friedman, Eric Gourgoulhon, and Masaru Shibata. Non-conformally flat initial data for binary compact objects. *Phys. Rev. D*, 80:124004, 2009. doi: 10.1103/PhysRevD.80.124004.
- Frank Verbunt and Paulo C. C. Freire. On the disruption of pulsar and X-ray binaries in globular clusters. *Astron. Astrophys.*, 561:A11, 2014. doi: 10.1051/0004-6361/201321177.
- Benny Walther, Bernd Brügmann, and Doreen Müller. Numerical black hole initial data with low eccentricity based on post-Newtonian orbital parameters. *Phys. Rev. D*, 79:124040, 2009.
- J. R. Wilson and G. J. Mathews. *Relativistic hydrodynamics.*, pages 306–314. 1989.
- James W. York. Gravitational degrees of freedom and the initial-value problem. *Phys. Rev. Lett.*, 26:1656–1658, 1971.
- James W. York. Conformal ‘thin-sandwich’ data for the initial-value problem of general relativity. *Phys. Rev. Lett.*, 82:1350–1353, 1999. doi: 10.1103/PhysRevLett.82.1350.

Abbreviations

ADM	Arnowitt-Deser-Misner
BAM	Bifunctional Adaptive mesh (name of the code)
BH	Black hole
CFV	Constant fluid velocity
CTS	Conformal thin-sandwich
CTT	Conformal transverse traceless
EOB	Effective-one-body
EoS	Equation of state
GRHD	General relativistic hydrodynamics
GW	Gravitational wave
LIGO	Laser Interferometer Gravitational Wave Observatory
Lorene	Langage objet pour la relativité numérique (name of the code)
MG	Multigrid
NS	Neutron Star
PDE	Partial differential equation
PN	Post-Newtonian
TOV	Tolmann-Oppenheimer-Volkoff
WENO	Weighted essentially non-oscillatory
XCTS	Extended conformal thin-sandwich

Acknowledgment

It is a pleasure to thank my supervisor Prof. Bernd Brügmann for giving me the opportunity to work in the field of numerical relativity and thus to write this thesis. He has always been supportive during the years of the master's and PhD studies.

I want to thank Dr. Charalampos Markakis, who tutored me as his “Jedi apprentice“ and who has been the foundation of this work. He listened to uncountable many questions and problems and always tried to find an answer, while he always knew a well written reference with nice physical interpretations. Additionally, Haris provided many personal advises and did not punish me with more than 50 push-ups if the implementation failed again. Furthermore, I want to thank Dr. David Hilditch, because he has always been open for questions — especially if everybody else was busy— and for perfectly fulfilling his role as a “Senior Postdoc“ to make the group a friendly, enjoyable and nice community.

Of course, I also want to thank Dr. Georgios Gerakopoulos, for many delightful discussions, evenings and basketball matches. I thank Dr. Sebastiano Bernuzzi and Dr. Nathan Johnson-McDaniel for helpful discussions and many valuable comments on my work. Thanks to Prof. Maximiliano Ujevic Tonino, especially for initializing the office statistics and being the majority of 2835 visits within 2 years, even if he only actively pushed for a year. In addition, I want to thank Prof. Wolfgang Tichy for his support with SGRID and Dr. Andreas Weyhausen for many valuable tips, even though he betrayed us on Men's Day.

I am thankful for my office mates Enno Harms, Toni “Tim“ Dietrich and Marcus Bugner, since we could always discuss every topic and had a great time together. I thank Marcus for not rage-quitting most of our events and for his outstanding efforts to keep the environment clean, even below the surface of the Saale. My special thanks goes to Enno Harms, the green Chancellor, who was accompanying me over the last 8 years throughout the whole studies and without whom these years would be missing a lot of fun and remarkable events. Of course I also want to thank my invaluable fellow students, the great Moritz Feyerabend for just being an amazing entertainer and Martin Fruhnert for always being patient when teaching the local culture.

Special thanks for proof reading goes to Enno, David, George and Marcus.

Finally, I want to thank my parents and my sister for their support over all the years and for always believing in me. I am particularly grateful to my girlfriend Jessica for always listening to me and encouraging me in stressful times as well for being my non-physics-anchor to share all the happy times with.

Curriculum Vitae

Niclas Moldenhauer

Adress Lutherstraße 90
 07743 Jena
 Germany
Email niclas.moldenhauer@gmail.com
Phone +49171 94493338
Date of birth 04.05.1988
Place of birth Braunschweig

Education

2000 - 2007 Abitur (1.7), *Gymnasium Groß Ilsede*
2007 - 2010 B.Sc. in Physics (1.6), *Technische Universität Braunschweig*
2010 - 2012 M.Sc. in Physics (1.4), *Friedrich-Schiller Universität Jena*
since 2012 PhD in Physics, *Friedrich-Schiller Universität Jena*

Teaching

WS 2012/13 Mathematische Methoden III, Assistant of Prof. Dr. Lotze
SS 2013 Elektrodynamik (für Lehramt), Assistant of Prof. Dr. Lotze

Zusammenfassung

Die Simulation von Neutronensternen erfolgt in den meisten Arbeiten durch Evolution von Anfangsdaten, die unter der Annahme helikaler Symmetrie erzeugt wurden. Dadurch erfolgt der Umlauf auf Kreisbahnen, die einerseits keine radiale Geschwindigkeitskomponente aufgrund der Abstrahlung von Gravitationswellen berücksichtigen. Andererseits können keine Sterne auf exzentrischen Umlaufbahnen simuliert werden ohne starke Vereinfachungen zu machen, sodass beispielsweise verfälschende zeitliche Oszillationen der Dichte auftreten. In dieser Arbeit erweitern wir den benutzten Symmetrievektor, indem wir den elliptischen Orbit jedes Sterns als augenblicklich kreisförmig approximieren und dafür einen Kreis benutzen der sich in die Ellipse einschmiegt. Wir zeigen dass diese zwei Symmetrievektoren benutzt werden können um Integrale der Euler-Gleichung innerhalb der Sterne zu bilden. Daraus konstruieren wir ein selbst konsistentes Iterationsschema zur Konstruktion von Anfangsdaten, welche die Einstein'schen Zwangsbedingungen und die Materiegleichungen erfüllen. Schließlich erweitern wir das Schema indem wir noch radiale Geschwindigkeitskomponenten hinzufügen. Insgesamt ermöglicht uns das, konsistente Anfangsdaten zu erzeugen bei denen wir erstmals die radiale und die tangentielle Geschwindigkeit der Sterne beliebig variieren können.

Wir implementieren dieses Schema in zwei existierende Codes. Zunächst in einfachen kartesischen Koordinaten mit einem Multigrid-Löser, wobei wir vereinfachende Annahmen für das Geschwindigkeitsfeld machen. Später implementieren wir unsere Methode in einen spektralen Code mit oberflächen-angepassten Koordinaten und lassen diese Vereinfachung wieder fallen.

Wir vergleichen beide Ergebnisse und zeigen, dass die erste Lösung, insbesondere bei größeren Entfernungen wie sie bei exzentrischen Systemen auftreten, sehr brauchbar ist. Für akkurate Berechnungen verwenden wir die spektrale Methode, in der es uns außerdem möglich ist, den Sternen Spin und realistische Zustandsgleichungen zu verleihen. Das Hauptaugenmerk dieser Arbeit liegt jedoch bei den Exzentrizitäten. Wir untersuchen Evolutionen von unseren stark exzentrischen Anfangsdaten und sehen drastische Verbesserungen von mehr als einer Größenordnung bei den unphysikalischen Oszillationen, die bei inkonsistenten Anfangsdaten auftreten. Weiterhin können wir die in früheren Arbeiten gefundenen f-Moden Oszillationen bestätigen, welche bei nahen Begegnungen der Sterne durch Gezeitenkräfte induziert werden.

Des Weiteren betrachten wir den Einfluss verschiedener Stationaritätsbedingungen auf die Anfangsdaten. Hierbei finden wir, dass die größte Verbesserung unserer Daten im Vergleich zu inkonsistenten Lösungen aus der Stationarität im mitrotierenden Koordinatensystem herrührt, anstatt ein linear mitbewegtes Koordinatensystem anzunehmen.

Außerdem benutzen wir die neue Möglichkeit der radialen Geschwindigkeitskomponente um

Anfangsdaten mit sehr kleinen Exzentrizitäten zu erzeugen, die mehr als einen Faktor 10 unter denen bisheriger zirkulärer Anfangsdaten liegen, und daher astrophysikalisch besser geeignet sind. Dazu beschreiben wir ein weiteres Iterationsschema, welches auf bisherigen Arbeiten anderer Gruppen zu schwarzen Löchern basiert. Damit finden wir sukzessive bessere Parameter für die Tangential- und Radialgeschwindigkeit, mit denen ein bis zwei Orbits simuliert werden um wiederum bessere Anfangsdaten finden zu können. Wir sind so in der Lage erstmals die Einflüsse von sehr kleinen Exzentrizitäten auf die gemessenen Gravitationswellen zu zeigen.

Abschließend widmen wir uns ähnlichen physikalischen Betrachtungen wie für Anfangsdaten, nutzen dies aber zur Beschreibung eines Hamilton-Jacobi Evolutionsschemas für nicht rotierende Sterne. Dieses Schema ist insbesondere für die von uns entwickelten Anfangsdaten nützlich. Wir beschreiben kurz die erste Implementierung eines solchen Schemas und zeigen erste vorläufige Ergebnisse.

Ehrenwörtliche Erklärung

Ich erkläre hiermit ehrenwörtlich, dass ich die vorliegende Arbeit selbständig, ohne unzulässige Hilfe Dritter und ohne Benutzung anderer als der angegebenen Hilfsmittel und Literatur angefertigt habe. Die aus anderen Quellen direkt oder indirekt übernommenen Daten und Konzepte sind unter Angabe der Quelle gekennzeichnet. Bei der Auswahl und Auswertung haben mir die nachstehend aufgeführten Personen in der jeweils beschriebenen Weise unentgeltlich geholfen:

1. Prof. Brüggemann - beratend
2. Dr. Charalampos Markakis - beratend
3. Dr. Nathan Johnson-McDaniel - beratend
4. Prof. Wolfgang Tichy - beratend

Weitere Personen waren an der inhaltlich-materiellen Erstellung der vorliegenden Arbeit nicht beteiligt. Insbesondere habe ich hierfür nicht die entgeltliche Hilfe von Vermittlungs- bzw. Beratungsdiensten (Promotionsberater oder andere Personen) in Anspruch genommen. Niemand hat von mir unmittelbar oder mittelbar geldwerte Leistungen für Arbeiten erhalten, die im Zusammenhang mit dem Inhalt der vorgelegten Dissertation stehen. Die Arbeit wurde bisher weder im In- noch im Ausland in gleicher oder ähnlicher Form einer anderen Prüfungsbehörde vorgelegt. Die geltende Promotionsordnung der Physikalisch-Astronomischen Fakultät ist mir bekannt. Ich versichere ehrenwörtlich, dass ich nach bestem Wissen die reine Wahrheit gesagt und nichts verschwiegen habe. Hiermit erkläre ich, Niclas Moldenhauer, dass ich die vorliegende Arbeit selbständig verfasst und keine anderen als die angegebenen Hilfsmittel benutzt habe. Zitate wurden als solche kenntlich gemacht.

Niclas Moldenhauer,
Jena, den April 24, 2016